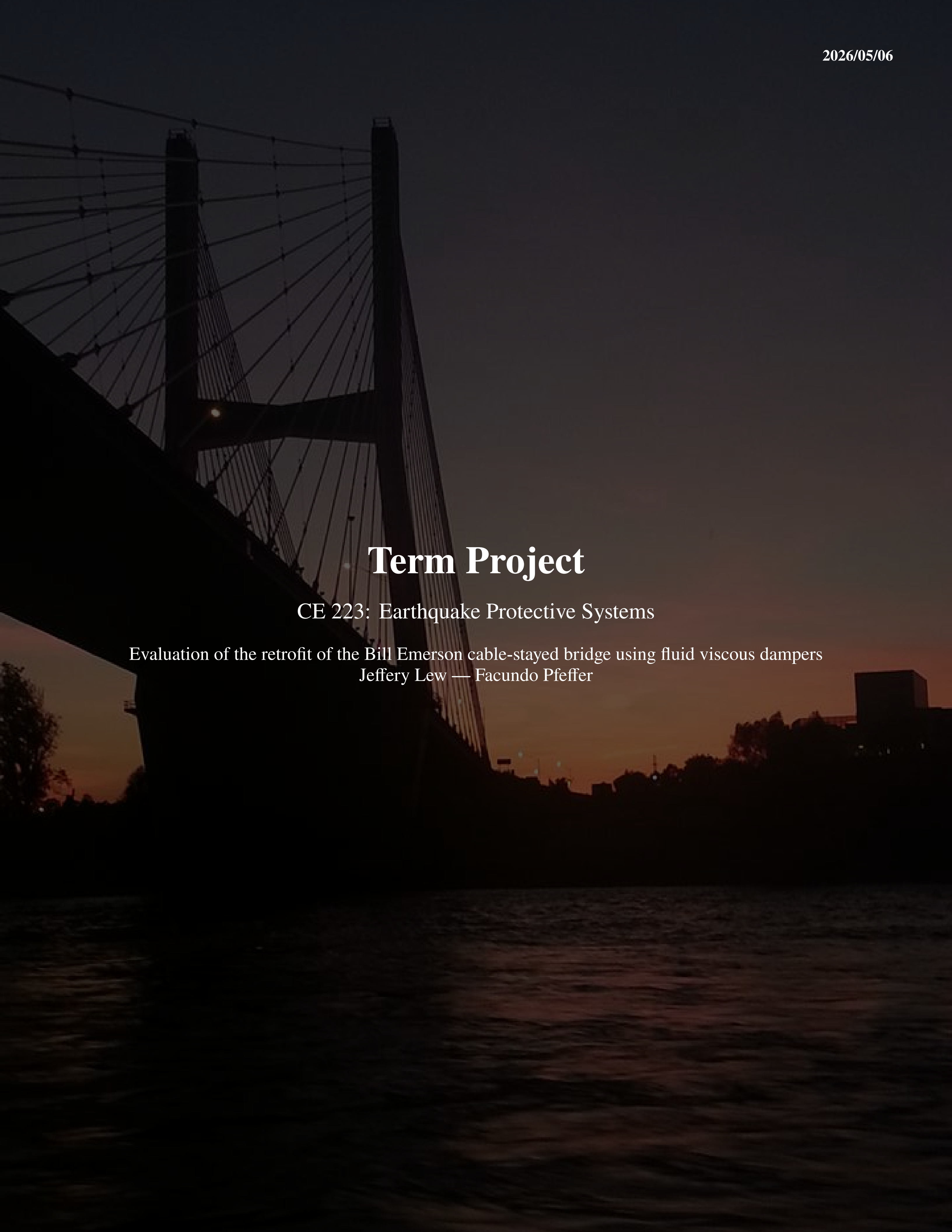

2026/05/06

Term Project

CE 223: Earthquake Protective Systems

Evaluation of the retrofit of the Bill Emerson cable-stayed bridge using fluid viscous dampers
Jeffery Lew — Facundo Pfeffer

Contents

1 Statement of Contributions

1.1 Contributions of Jeffery Lew

- Conducted the initial research and literature review on long-span bridges in seismic regions, including the identification of potential sources and reports related to the Bill Emerson Memorial Bridge.
- Assisted with the measurement and estimation of bridge-element dimensions during the preliminary modeling stage.
- Peer reviewed the general modeling decisions and assumptions adopted in the finite element model.
- Performed the seismic hazard deaggregation, ground-motion selection, and ground-motion scaling.
- Validated the implementation of fluid viscous dampers in MIDAS Civil using a simplified test model.
- Input the selected ground-motion time histories and corresponding load cases into the final finite element model.
- Created the time-history result settings for the quantities of interest, including displacements, accelerations, and element or nodal forces for each ground motion.
- Ran multiple nonlinear response-history analyses for the unretrofitted models in MIDAS Civil.
- Extracted model results and generated time-history responses for the selected quantities of interest.
- Contributed to the preparation and peer review of the final report.

1.2 Contributions of Facundo Pfeffer

- Conducted a literature review of available section properties, material properties, and benchmark information for the Bill Emerson Memorial Bridge.
- Conducted a literature review of seismic protective devices in large-span bridge applications with special emphasis in FVDS.
- Developed and calibrated the bridge finite element model in MIDAS Civil. Numerical model through comparison of modal properties and mode shapes, including multiple model-refinement iterations.
- Performed hand calculations to verify model integrity.
- Reviewed the MIDAS Civil finite element formulation, finite-difference implementation, and nonlinear analysis capabilities relevant to the bridge model. Developed appendixes A and C accordingly.
- Ran nonlinear response-history analyses for retrofitted cases as well as bounded analyses.
- Ran multiple nonlinear response-history analyses for retrofitted models, including bounding analyses and linear direct-integration checks in MIDAS Civil.
- Reviewed and tested the numerical damping behavior and exponential damping function used in the analyses, as discussed in **Section E**.
- Prepared the results analysis and conclusions.
- Peer reviewed the stages that led to the report.

2 Summary

Fluid viscous dampers (FVDs) are passive earthquake-protection devices commonly used in buildings and bridge structures. These devices provide significant supplemental damping with minimal additional stiffness contribution to the existing structure, making them strong candidates for retrofit applications. Their behavior is commonly described by the velocity-dependent exponential relation $P = C|v|^{\alpha}\,\mathrm{sgn}(v)$, where P is the damper force, v is the relative velocity across the device, C is the damping coefficient, and α is the velocity exponent. A linear FVD corresponds to $\alpha = 1.00$, while nonlinear FVDs use $\alpha \neq 1.00$.

This report investigates the influence of FVDs on the seismic performance of a long-span bridge. The Bill Emerson Memorial Bridge, a cable-stayed bridge crossing the Mississippi River between Missouri and Illinois, was selected as the case-study structure. The bridge is located near the New Madrid Seismic Zone, where large-magnitude earthquake scenarios have been historically recognized as a controlling seismic hazard. To represent this seismic demand, a suite of six representative ground motions was selected for the analysis to compare the structural performance of the unretrofitted bridge with that of a retrofitted configuration.

Benchmark reports with information on the geometry, material, and dynamic properties of the bridge were used as a reference to create a finite element model using Midas Civil with beam and plate elements with shear deformation. A nonlinear response history analysis (NLRHA) considering geometric nonlinearity was conducted for each of the selected ground motions, examining the bridge's response with and without FVDs. In this study, 10 FVDs are adopted in the longitudinal direction. The standard retrofitted configuration uses nonlinear dampers with $C = 4426\ \mathrm{kN}(s/m)^{0.40}$ and $\alpha = 0.40$, which places the device force level within the range of reported long-span cable-stayed bridge applications. To evaluate the sensitivity of the response to the damper capacity, a bounded analysis is also conducted using $C = 2725\ \mathrm{kN}(s/m)^{0.40}$ as a lower-bound case and $C = 11000\ \mathrm{kN}(s/m)^{0.40}$ as an upper-bound case, while keeping $\alpha = 0.40$. In addition, the response is compared with an equivalent linear viscous damper model with $\alpha = 1.00$ and $C = 7650\ \mathrm{kN\,s/m}$, selected to dissipate the same energy per cycle as the base nonlinear damper.

The response quantities of interest used for comparison were the longitudinal displacement and acceleration at the bridge east abutment modeled as a roller support, overturning moment and shear at the tower base, and transverse shear in the tower beam. It is concluded that the addition of FVDs significantly reduced the longitudinal displacement and accelerations of the bridge, as well as reduced the tower overturning moment. However, the retrofitted bridge base shear and tower shear experienced both reductions and slight demand increases, which is associated to the complex coupling behavior between the cables and the tower, potentially indicating the need of including transverse dampers in the retrofit. This is also in agreement with the bounding analysis, where dampers with more energy dissipation decreased the same quantities while keeping the shear responses without significant reductions. The linear case, in turn, enhanced the affected response quantities. It was also noted that the less intense earthquake ground motion actually increased the peak response quantities after the addition of FVDs, but the magnitude of these quantities is still significantly less than those for the MCER event.

3 Introduction

This report was prepared for CE223: Earthquake Protective Systems, offered as part of the Structural Engineering, Mechanics and Materials program at the University of California, Berkeley, under Prof. Dimitrios Konstantinidis[1]. The objective of the project is to investigate the influence of fluid viscous dampers (FVDs) on the seismic response of a long-span bridge.

The Bill Emerson Memorial Bridge was selected as the case-study structure because it is a well-documented cable-stayed bridge with available information on geometry, material properties, seismic instrumentation, modal identification, and finite element benchmark models[2, 3, 4], Due to its proximity to the New Madrid fault[5], the bridge has been used as a benchmark structure for seismic control studies of cable-stayed bridges, which makes it a suitable reference case for evaluating supplemental damping strategies. The available documentation supports the development of the numerical model presented later in detail in Section A.

3.1 Project Description

The Bill Emerson Memorial Bridge crosses the Mississippi River between Cape Girardeau, Missouri, and East Cape Girardeau, Illinois. The cable-stayed bridge carries Missouri State Highway 34, Missouri State Highway 74, and Illinois Route 146, and was opened to traffic in 2003 [2, 4]. General views of the bridge are shown in **Fig. 3.1** and **Fig. 3.2**.

3.1.1 General Description

The structure has a total length of approximately 1206 m (3956 ft). The cable-stayed portion consists of a 350.6 m (1150 ft) main span and two 142.7 m (468 ft) side spans. The main bridge includes two towers and 128 stay cables, while the Illinois approach is supported by additional piers [2, 4]. The longitudinal layout of the cable-stayed bridge is shown schematically in **Fig. 3.3**.

Figure 3.1: Artist rendering of the Bill Emerson Memorial Bridge [2].

Figure 3.2: Night view of the Bill Emerson Memorial Bridge [6].

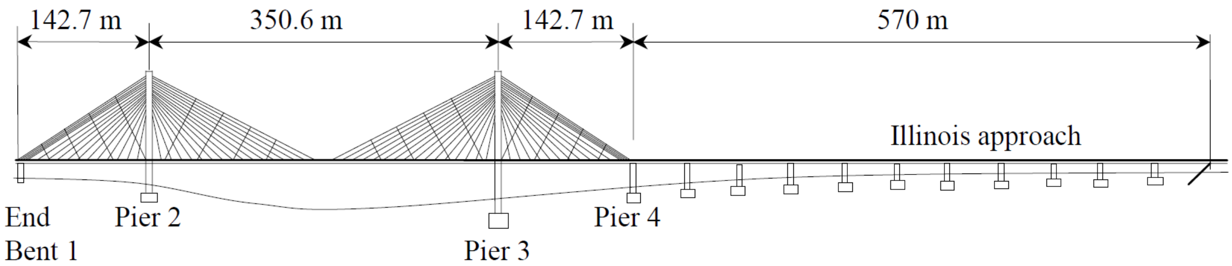

Figure 3.3: Schematic elevation of the Bill Emerson Memorial Cable-stayed Bridge [2].

The bridge is located near the New Madrid Seismic Zone [5], and seismic effects were therefore an important consideration in its design. Previous studies, together with the results discussed later in this report, indicate that the dynamic behavior of the bridge is highly coupled, with vertical, longitudinal, transverse, and torsional components contributing to the response of the cable-stayed system [2, 3]. This characteristic makes the bridge an appropriate case study for assessing the influence of supplemental damping devices on a flexible long-span structure [1].

3.1.2 Structural Typology

The deck is approximately 29.3 m (96 ft) wide and consists of steel framing with a concrete slab. The reported deck cross section, shown in **Fig. 3.4**, includes longitudinal steel girders, transverse steel I-beam floor beams (as observed in **Fig. 3.5**), concrete slab, barriers, railing anchorage, and stay-cable anchorage regions [3]. These features are relevant for the numerical idealization because the deck stiffness and mass distribution strongly influence the modal properties of the bridge. The tower elevation and representative tower cross sections, shown in **Fig. 3.6**, were also used to define the tower frame section regions in the numerical model. Steel ASTMA709 grade 50W is used, with $f_y = 344 MPa$ (50 ksi)[3]. The concrete slabs are made of prestressed concrete with $f_c' = 41.36 MPa$ (6000 psi).

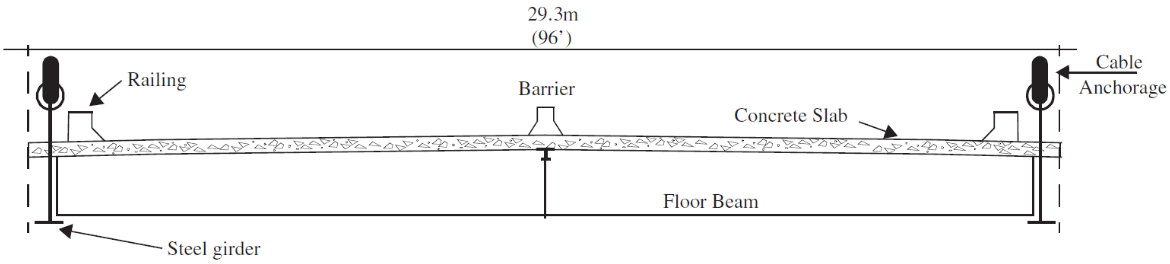

Figure 3.4: Typical cross section of the bridge deck [3].

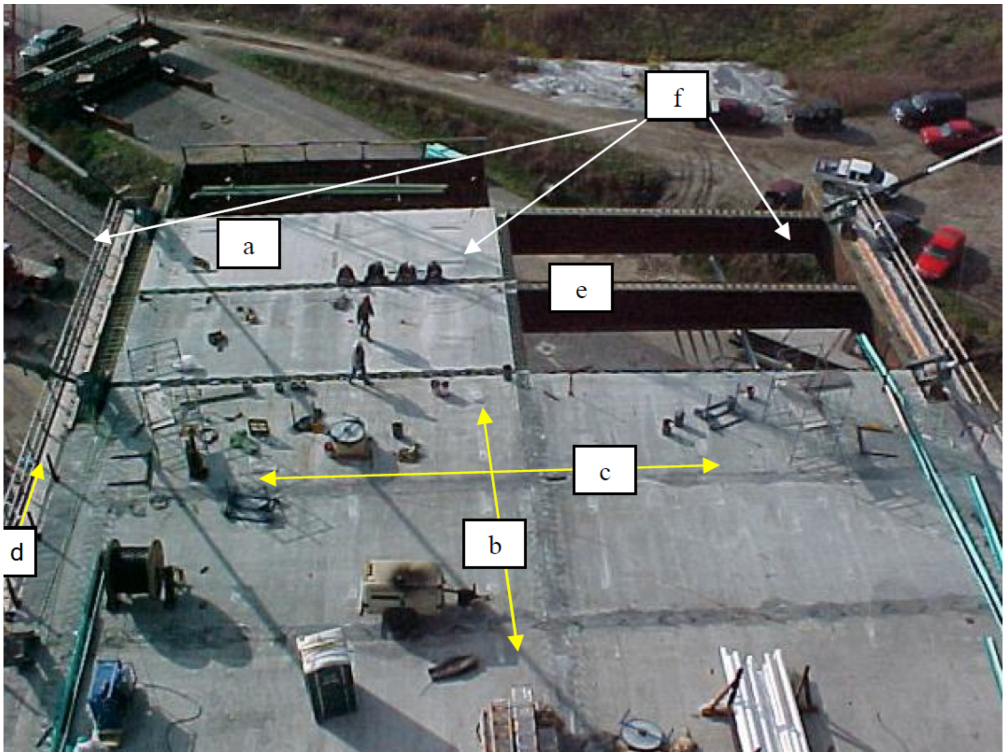

Figure 3.5: Construction-stage top view of the Bill Emerson Memorial Bridge deck system, identifying the main deck components: (a) typical precast concrete deck panel, (b) cast-in-place longitudinal joint, (c) cast-in-place transverse joint, (d) short cast-in-place cantilever region, (e) typical transverse floor beam, and (f) longitudinal girders[7].

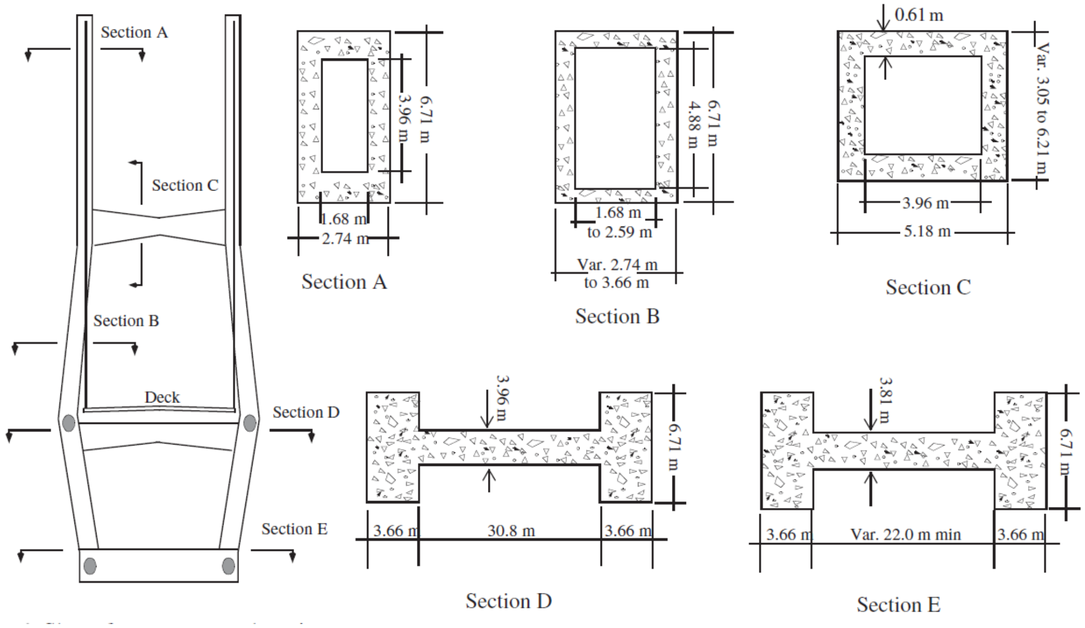

Figure 3.6: Tower elevation and representative tower cross sections at different levels [3].

3.1.3 Geological Site Description

The Bill Emerson Memorial Bridge span across the Mississippi River between Cape Girardaeu, Missouri and East Cape Girardaeu, Illinois, which positions the bridge in the northern-most portion of the Upper Mississippi Embayment. This part of the Mississippi River is mostly characterized by older Pleistocene-age terrace deposits and more recent Holocene-age alluvial deposits[8]. This characterization implies denser and stiffer layers of bedrock with softer, unconsolidated river sediments above. Therefore, the geology of the site results in moderately stiff soils, corresponding with Site Class D.

Additionally, the site is located near the New Madrid Seismic Zone, which is an intra-plate fault zone in the Central United States composed of multiple strike-slip faults and some reverse fautling.

3.2 Fluid Viscous Dampers as a Seismic Protection Device

Fluid viscous dampers (FVDs) are passive supplemental energy-dissipation devices used to reduce structural response under dynamic loading. In seismic applications, their purpose is to dissipate part of the input energy through a velocity-dependent resisting force, thereby reducing displacement demands, internal force demands, and acceleration-sensitive response quantities without relying exclusively on strength or damage/-ductility of the primary structural system [1, 9, 10]. Their use has been reported in buildings, bridges, towers, and elevated transportation structures, and they are commercially available through specialized manufacturers for project-specific seismic protection applications [9, 11].

In a typical installation, an FVD connects two structural points that experience relative motion during an earthquake. The device force is primarily governed by the relative velocity between its two ends. In idealized form, the constitutive behavior is commonly represented as a nonlinear exponential function:

$$P(t) = C_\alpha \left|\dot{u}(t)\right|^\alpha \operatorname{sgn}(\dot{u}(t)),$$

where $P(t)$ is the damper force, $\dot{u}(t)$ is the relative velocity along the damper axis, C_α is the damper coefficient, and α is the velocity exponent. The detailed interpretation of this force law, its force–displacement loops, and the associated energy dissipation per cycle are presented in Section C.

For design and numerical modeling, the relevant damper properties are not universal constants. They depend on the selected device location, the expected relative displacement and velocity demands, the target supplemental damping level, the allowable force transferred to the surrounding structure, and the practical limits imposed by stroke, connection detailing, temperature range, and manufacturer testing capacity. Therefore, the FVD parameters used in this project are treated as design variables to be selected from the response demands obtained from the bridge model, rather than as fixed properties known before the analysis.

In the context of the Bill Emerson Memorial Bridge, the objective is not to redesign the bridge, but to evaluate how supplemental viscous damping would modify the seismic response of a flexible cable-stayed system. This makes FVDs especially suitable for the present investigation: they can introduce additional energy dissipation through relative motion at selected locations while avoiding the large stiffness changes that would result from purely elastic restraining devices. The modeling strategy and final damper properties adopted for the numerical study are discussed the corresponding analysis sections.

3.3 Analysis Approach

A schematic workflow of the procedure is depicted in **Fig. 3.7**. The study begins with the extraction of the bridge geometry and structural information from the available reference sources, followed by the construction of a finite element model. The model is then calibrated through modal analysis by comparing the computed natural frequencies and mode shapes with reported data. In parallel, a suite of representative ground motions is selected to define the seismic demand. The calibrated model and selected ground motions are finally used to perform nonlinear response-history analyses of the unretrofitted and retrofitted bridge configurations.

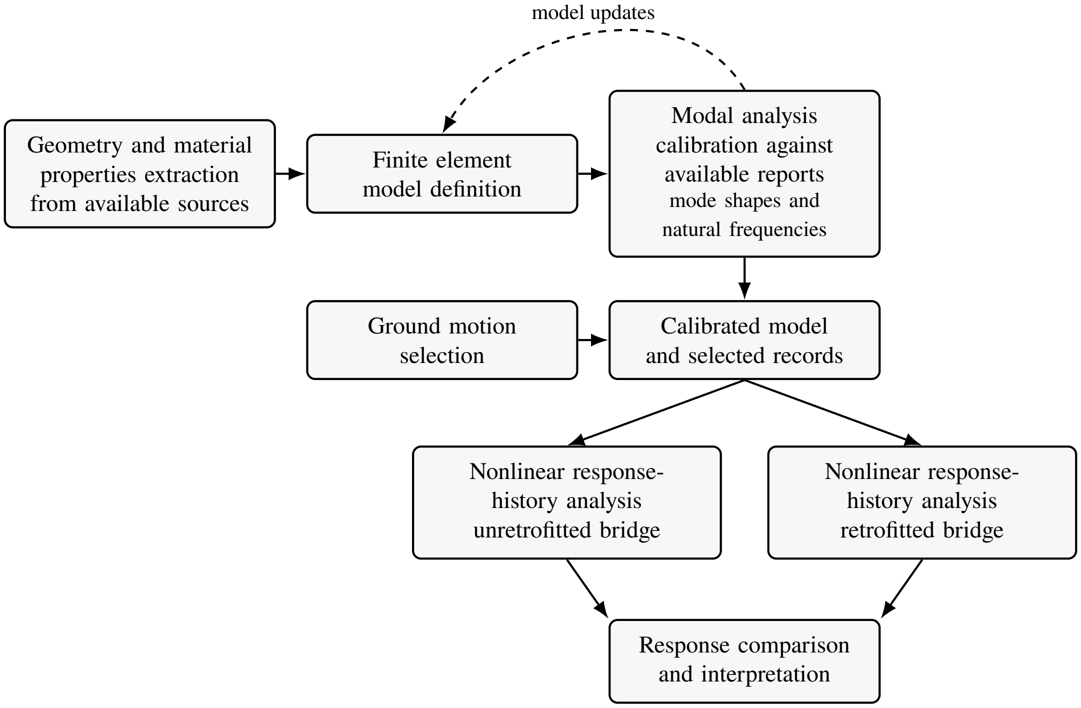

Figure 3.7: Analysis procedure followed for the seismic evaluation of the Bill Emerson Memorial Bridge with and without fluid viscous dampers.

4 Structural Analysis

A finite element model is constructed in MIDAS Civil[12] to assess the influence of the proposed retrofit. The model, introduced in **Section 4.2** and later detailed in **Section A**, is subjected to a Nonlinear Time History Analysis (NLRHA) for a suite of representative ground motions to assess influence of the retrofit. The selection of ground motions is treated in detail in **Section B**.

4.1 Fundamental Hypothesis Considered

4.1.1 Material Linearity

Material linearity is preserved for all structural materials in the bridge model. This assumption is reasonable for the response level considered because the main structural components, including the steel stay cables, are expected to remain within an approximately linear stress-strain range. The most relevant nonlinear effects in the cable system are instead associated with cable sag, initial tension, and tension-dependent stiffness. These effects are represented through geometric nonlinearity, as discussed next.

4.1.2 Geometric Nonlinearity

Geometric nonlinearity was considered consistently in the bridge model through the use of cable elements, prestress, and large-displacement nonlinear analysis. The modal properties were obtained from a prestressed configuration in which the stay cables were included as cable elements rather than removed or replaced by simplified boundary conditions. Therefore, the computed natural periods and mode shapes reflect the cable-supported stiffness of the bridge, including the influence of the initial cable forces on the tangent stiffness of the system.

The subsequent nonlinear response-history analyses were performed in MIDAS Civil using Newmark's integration with the *Large Displacement*[13]. This setting accounts for geometric nonlinearity by updating the stiffness and internal-force state as the structure deforms. As a result, second-order effects associated with axial force, cable tension, and changes in structural configuration are included in the dynamic equilibrium iterations. For the stay cables, this is especially important because their stiffness is tension-dependent and affected by sag.

4.1.3 Inherent Classical Damping

In large-scale cable-stayed bridges, the effective modal mass is often distributed over many coupled modes rather than concentrated in only a few dominant modes[14][1]. For this reason, adopting Rayleigh damping can introduce artificial damping distortion when only two modes are selected for calibration. In particular, modes outside the calibrated frequency interval may become excessively damped, while modes between the two calibration frequencies may receive damping ratios smaller than the target value.

A more appropriate choice for the present study is therefore to prescribe a constant modal damping ratio for all retained modes. This approach is also consistent with the Phase II benchmark study for the Bill Emerson Memorial Bridge, where the damping matrix was constructed by assigning 3% of critical damping to each mode[3]. Accordingly, the inherent structural damping ratio adopted in this work is

$$\xi = 0.03.$$

---

[1] This feature is also demonstrated for the present bridge model in Section 5.1.3.

4.2 Finite Element Model

The finite element model was constructed in MIDAS Civil[12]. Two main structural element types were used:

1. Shear-deformable three-dimensional beam elements were used for the bridge members whose response is governed by axial, flexural, and transverse shear deformation. This choice is consistent with the Timoshenko beam idealization, in which cross sections remain plane but not necessarily normal to the deformed beam axis[15, 16, 17].
2. Shear-deformable plate elements were used for the deck. In MIDAS Civil, the corresponding thick quadrilateral plate formulation is based on the Discrete Kirchhoff–Mindlin quadrilateral element, commonly denoted DKMQ, which is derived from Mindlin–Reissner plate theory and uses assumed shear strain fields to reduce shear locking[18].
3. Cable elements were used for the stay cables. In MIDAS Civil, cable elements are tension-only line elements for which pretension or unstrained-length data can be assigned at the element level. For linear analysis, MIDAS converts cable elements into equivalent truss elements; for geometric nonlinear analysis, the same cable elements are treated as elastic catenary elements. Therefore, when large-displacement nonlinear response-history analysis is used, the stay-cable stiffness is not represented as a constant axial stiffness only, but as a tension-dependent geometric stiffness that accounts for cable sagging effects through the catenary formulation[19].

4.3 Nonlinear Response-History Analysis Procedure

To assess the effectiveness of the proposed retrofit, Nonlinear Response-History Analysis (NRHA) is conducted. As described in Section 4.1.2, geometric nonlinearity is included in the model because it can significantly affect the response of the stay cables. The direct-integration analysis is ***performed about the deformed configuration obtained under dead load with cables pretention***.

The Newmark integration parameters adopted in the nonlinear analyses are:

$$\gamma = 0.60, \qquad \beta = 0.3025.$$

These values satisfy the usual unconditional-stability condition for the linear Newmark method, since $\gamma \geq 0.50$ and $\beta \geq \gamma/2$. The choice $\gamma > 0.50$ introduces algorithmic damping, which is useful for reducing high-frequency numerical oscillations but should not be interpreted as physical damping. Therefore, the selected parameters are treated as a numerical-damping choice rather than as a purely neutral time-integration scheme. Further discussion of this choice is provided in **Section E**.

4.4 Ground Motion Selection

A suite of representative ground motions were selected to conduct the NLRHA. Two different levels of earthquake intensities were considered to assess the retrofit. The main hazard level considered was the bridge's structural performance under a rare and extreme maximum considered earthquake (MCER) event; the secondary hazard level considered was a lower intensity but more probable representative design earthquake event.

Details regarding the ground motion selection criteria and procedure can be found in **Section B**. The full list of selected ground motions for both seismic hazards is presented in **Table B.1** and **Table B.2**.

Due to the time constraint of the project and the costly computational time to run a NLRHA in Midas Civil, ***only six of the ten selected ground motions are used in the NLRHA to assess the influence of the FVD retrofit.*** These six ground motions are:

- All 5 MCER level ground motions in **Table B.2**.
- The ”Mineral 2011-08-23” design earthquake level ground motion in **Table B.1**.

GM Record	Earthquake Name	Recording Site	Magnitude
W1	Kocaeli, Turkey	Bursa Tofas	7.51
W2	Chi-Chi, Taiwan	CHY004	7.62
W3	Chi-Chi, Taiwan	CHY065	7.62
W4	Manjil, Iran	Rudsar	7.37
W5	Denali, Alaska	R109 (temp)	7.90
E	Mineral 2011-08-23	NP.2225	5.74

Table 4.1: Ground Motion Records Used in the NLRHA of the Bill Emerson Bridge Retrofit Assessment

The GM Record label for each ground motion in **Table 4.1** is further referenced in **Section 5**.

4.5 Properties and Layout of the Selected Viscous Dampers

The definition of the retrofit required two modeling decisions: the placement of the dampers and the constitutive properties assigned to each device. Since a fluid viscous damper develops force from the relative velocity between its two end nodes, the damper locations were selected from the preliminary linear dynamic analyses of the unretrofitted bridge. The candidate locations were examined in terms of longitudinal relative velocity, rather than absolute deck velocity, because this is the velocity that enters the damper force law. Based on this criterion and on the available support layout of the bridge, ten longitudinal dampers were implemented: four devices at each tower and two devices at the left roller support, where longitudinal deck movement is permitted, as per **Fig. 4.1**.

The idealized behavior of a fluid viscous damper is presented in Section C. In that appendix, the local relative displacement $u(t)$, relative velocity $\dot{u}(t)$, and nonlinear force–velocity relation are defined in **Eq. (C.1)**. Therefore, the main modeling parameters for each device are the damper coefficient C_α and the velocity exponent α. These parameters are difficult to select uniquely because increasing damper capacity does not necessarily improve every response quantity at the same time. Previous studies on cable-stayed bridges have shown that viscous dampers can strongly reduce deck displacement and tower bending demand, while force-related quantities such as pylon base shear may remain less robust or become record-dependent [20, 21]. For this reason, the selected properties are treated as a preliminary design, followed by comparison cases that test the sensitivity of the response to the damper law.

The same ten-device longitudinal layout is retained in all the comparisons below. Therefore, the base nonlinear case, the equivalent linear case, and the bounded coefficient study differ only in the assigned damper properties. This allows the influence of the velocity exponent and the coefficient C_α to be evaluated without changing the number, location, or orientation of the devices.

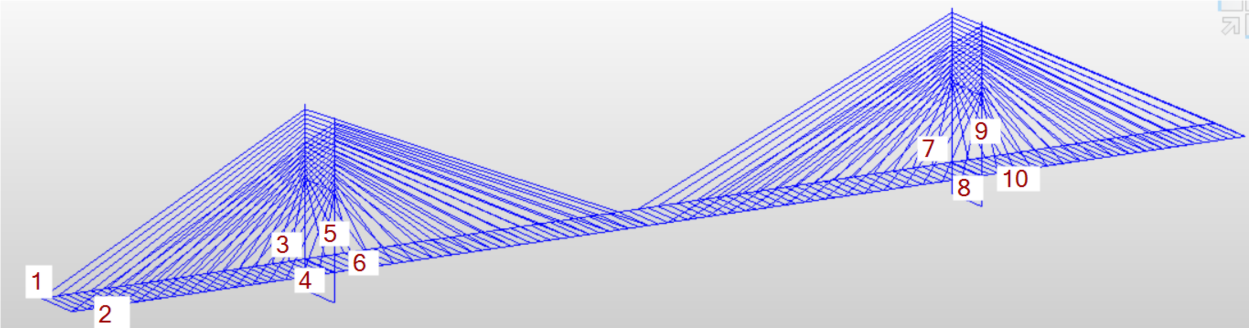

Figure 4.1: Selected Location of FVDs from 1 to 10.

4.5.1 Base Nonlinear Case

The base retrofit case uses the nonlinear force–velocity law introduced in Section C and defined in **Eq. (C.1)**. For each damper, the selected properties are:

$$C_\alpha = 4426\ \mathrm{kN}\,(\mathrm{s/m})^{0.40}, \qquad \alpha = 0.40.$$

The velocity exponent was selected based on reported bridge applications and on the expected behavior of nonlinear fluid viscous dampers. Several long-span cable-stayed bridge applications reported by Chen et al. [22] use nonlinear exponents in the range commonly associated with seismic fluid viscous dampers, including cases with $\alpha = 0.40$. In particular, the Sutong Bridge, a much longer cable-stayed bridge than the Bill Emerson Memorial Bridge, is reported with eight fluid viscous dampers, $C = 3750\ \mathrm{kN}\,(\mathrm{s/m})^{0.40}$, and $\alpha = 0.40$. The Xigu Yellow River Bridge, which has a main span of 360 m and a steel–concrete composite girder system comparable in scale to the Bill Emerson main span, was also studied with nonlinear viscous dampers; the optimized values reported by He et al. [23] were approximately $C = 10871\ \mathrm{kN}\,(\mathrm{s/m})^{\alpha}$ and $\alpha = 0.415$. These references support the use of $\alpha = 0.40$ as a representative nonlinear exponent for the present retrofit study.

The coefficient $C_\alpha = 4426\ \mathrm{kN}\,(\mathrm{s/m})^{0.40}$ was selected as an intermediate base-design value. It is larger than the lower coefficients reported in several bridge applications but also smaller than the high-capacity applications. It is also consistent with the Taylor Devices catalog for nonlinear fluid viscous dampers. For $\alpha = 0.40$, the conversion from the catalog units $(\mathrm{kip\,s/in})^{0.40}$ to $\mathrm{kN}\,(\mathrm{s/m})^{0.40}$ is:

$$C_{\mathrm{SI}} = 4.44822(39.3701)^{0.40} C_{\mathrm{US}} \approx 19.33 C_{\mathrm{US}}.$$

Therefore, the base-design value corresponds to:

$$C_{\mathrm{US}} = \frac{4426}{19.33} \approx 229 \quad (\mathrm{kip\,s/in})^{0.40},$$

which lies between adjacent tabulated commercial values in the Taylor Devices catalog [9]. Thus, the base coefficient is not treated as an optimized value, but as a practical intermediate value supported by reported bridge applications and by commercially available damper coefficient ranges.

4.5.2 Equivalent Linear Viscous Damper

As an additional comparison, the nonlinear dampers of the base retrofit case are replaced by linear viscous dampers. The number of dampers, their locations, and their local axes are kept unchanged. The purpose of this comparison is to isolate the effect of the velocity exponent while keeping the energy dissipation level comparable.

The linear damper is modeled as:

$$P(t) = C_{1,\mathrm{eq}}\dot{u}(t),$$

where $C_{1,\mathrm{eq}}$ is selected so that the linear device dissipates the same energy per cycle as the nonlinear device under a prescribed harmonic relative displacement. The energy-equivalent coefficient is derived in **Eq. (C.8)**. Writing the peak relative velocity of the harmonic motion as $V = \Omega u_0$, this coefficient is:

$$C_{1,\mathrm{eq}} = \frac{2}{\sqrt{\pi}} C_\alpha V^{\alpha-1} \frac{\Gamma\left(\frac{\alpha+2}{2}\right)}{\Gamma\left(\frac{\alpha+3}{2}\right)}.$$

For the present comparison, the representative peak relative velocity is taken as[2]:

$$V = 0.50 \text{ m/s}.$$

Substitution of $C_\alpha = 4426$ kN $(\mathrm{s/m})^{0.40}$, $\alpha = 0.40$, and $V = 0.50$ m/s gives:

$$C_{1,\mathrm{eq}} = \frac{2}{\sqrt{\pi}} (4426)(0.50)^{-0.60} \frac{\Gamma(1.20)}{\Gamma(1.70)}.$$

The gamma-function factor is:

$$\frac{2}{\sqrt{\pi}} \frac{\Gamma(1.20)}{\Gamma(1.70)} = 1.140.$$

Therefore:

$$C_{1,\mathrm{eq}} = 7649 \text{ kN s/m}.$$

The equivalent linear case is defined by:

$$C_{1,\mathrm{eq}} = 7650 \text{ kN s/m}$$

for each of the ten dampers.

This equivalence does not imply that the linear and nonlinear dampers produce the same force at every velocity. It only means that the two devices dissipate the same energy per cycle for the selected harmonic relative motion. The linear case is therefore used as an energy-equivalent reference case, not as a direct replacement for the nonlinear device.

4.5.3 Bounded Analysis of the Damper Coefficient

A bounded analysis is conducted to evaluate how sensitive the retrofit response is to the damper coefficient. The velocity exponent is kept fixed at:

$$\alpha = 0.40,$$

so that the comparison isolates changes in the force scale of the dampers. Three nonlinear coefficients are considered:

$$C = 2500, \qquad 4426, \qquad 11000 \quad \text{kN}\,(\mathrm{s/m})^{0.40}.$$

The middle value is the base design. The lower-bound value represents a moderate bridge-scale damper coefficient, while the upper-bound value represents a high-capacity commercial bound. This range is

---

[2] The peak relative velocity was obtained from a preliminar dynamic linear analysis conducted on the bridge.

intentionally broad enough to test whether the main trends observed in the retrofit response depend strongly on the assumed damper capacity.

The upper-bound value was selected using the Taylor Devices catalog for nonlinear fluid viscous dampers[9]. For $\alpha = 0.40$, the conversion from the tabulated coefficient in $(\text{kip s/in})^{0.40}$ to $\text{kN}\,(\text{s/m})^{0.40}$ is:

$$C_{\text{SI}} = 4.44822(39.3701)^{0.40} C_{\text{US}} \approx 19.33 C_{\text{US}}.$$

The selected upper-bound value therefore corresponds to:

$$C_{\text{US}} = \frac{11000}{19.33} \approx 569 \quad (\text{kip s/in})^{0.40},$$

which is one of the catalog values for $\alpha = 0.40$. The base-design value corresponds to:

$$C_{\text{US}} = \frac{4426}{19.33} \approx 229,$$

which also lies in a catalog value. The lower-bound value corresponds to:

$$C_{\text{US}} = \frac{2500}{19.33} \approx 129,$$

which is also available commercially.

The selected values therefore define a physically meaningful bounded range: a lower bridge-scale case, the base design, and a high-capacity commercial case. The purpose of this bounded study is not to identify a unique optimum value of C, but to determine whether the retrofit trends are robust to a substantial change in damper force capacity. In particular, the comparison helps distinguish response quantities that improve consistently as C increases from those that are governed by force redistribution within the deck–damper–tower system.

5 Results

5.1 Modal Analysis Calibration

5.1.1 Motivation for the Calibration: Uncertainties

After defining the material properties, section properties, cable properties, and boundary conditions from the available public information[2, 3, 4], several modeling uncertainties remain. The most relevant uncertainties are:

- The exact dimensions of the steel girders and steel floor beams are not fully defined in the available reports. These properties were initially inferred from sketches such as **Fig. A.2**[3] and from available photographs of the bridge and deck construction[24], but calibration was needed.
- The exact permanent dead load to be included in the model is not completely specified. This quantity directly affects the total mass, mass distribution, cable-force state, and dynamic properties of the structure[14, 25].

Because of these uncertainties, the model was calibrated using the measured natural frequencies and mode shapes reported for the actual bridge[3]. Mode shapes and natural frequencies provide a compact description of the global mass and stiffness distribution of a structure and are therefore useful indicators of the reasonableness of the numerical idealization[14, 25].

5.1.2 Eigenvalues and Eigenvectors Made

A detailed description of the comparison can be found in **Section A.5**, but an important distinction is made:

- Natural frequencies, i.e. eigenvalues, are compared ***against empirical data from the instrumented bridge***[2], results are found in **Table A.4**.
- Mode shapes, i.e. eigenvectors, are ***visually compared*** with the mode shapes presented in reports[2, 3].

Both criteria showed sufficient proximity and served as the calibrator for the geometrical uncertainties described in Section 5.1.1. A detailed description of the final section properties can be found at **Table A.2**.

5.1.3 Effective Modal Mass vs Mode Number

An eigenvalue analysis of the unretrofitted Bill Emerson Memorial Bridge model was conducted in Midas Civil to better understand the governing modes of vibration and overall dynamic behavior of a long-span bridge structure. It was observed that, unlike a typical building structure where the fundamental or first few modes (less than 10 modes) make up the majority of the effective modal mass, higher modes govern the dynamic behavior of long-span bridge structures such as the Bill Emerson Bridge. In fact, the modal analysis results show that it takes more than 100 modes in each translational direction of vibration to make up 90% of the effective modal mass for this bridge.

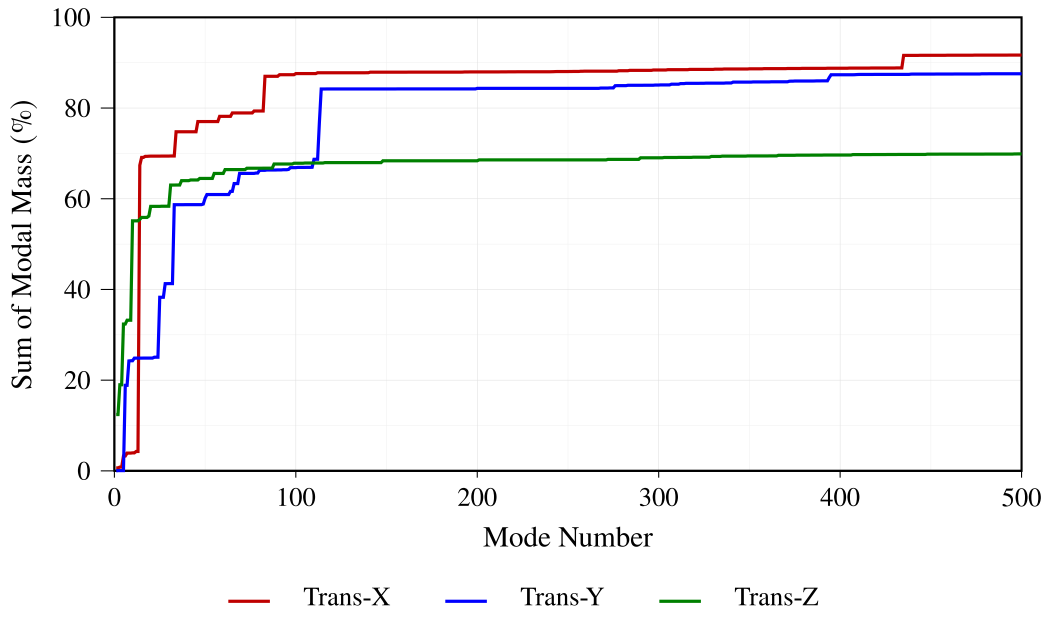

Figure 5.1: Sum of modal mass ratio for translation in X, Y, and Z directions over 500 modes.

5.2 Nonlinear Response-History Analysis

A nonlinear response-history analysis[3] is conducted for the structure under each selected ground-motion record. For each record, the response of the nonretrofitted bridge model is compared with the response of the bridge model retrofitted with longitudinal fluid viscous dampers.

The selected output locations are shown schematically in **Fig. 5.2**. The measured quantities are selected to capture both the global longitudinal response of the bridge and the force demands transmitted to the tower system:

- **(1) Roller-support longitudinal displacement.** The displacement u_x is measured at the roller support in the global x-direction. This quantity is used as the main measure of the longitudinal deck motion controlled by the dampers.
- **(2) Roller-support longitudinal acceleration.** The acceleration a_x is measured at the same support location and in the same global direction. This quantity is used to evaluate whether the dampers reduce the dynamic acceleration demand associated with the longitudinal bridge response.
- **(3) Tower overturning moment.** The bending moment M_y is extracted at Tower 1. This response quantity is used to evaluate how the reduction in longitudinal deck motion propagates through the deck–cable–tower force-transfer path.
- **(4) Tower base shear.** The base shear V_b is extracted at Tower 1. This quantity is used to evaluate the shear demand transmitted to the tower base after the dampers modify the longitudinal dynamic response of the bridge.

---

[3] Although nonlinear time-history analysis is often used as a synonym, the term nonlinear response-history analysis is adopted in this report because it more directly describes the objective of the procedure: evaluating the structural response generated by a prescribed ground-motion history. In the expression nonlinear time-history analysis, the words time and history both refer to the temporal nature of the analysis, which makes the terminology somewhat redundant.

- **(5) Transverse shear in the tower beam.** The transverse shear V_z is extracted at both ends of the monitored transverse tower beam, corresponding to elements E399 and E795. These two histories are plotted together because they represent the same local tower-beam demand measured at opposite ends of the selected member.

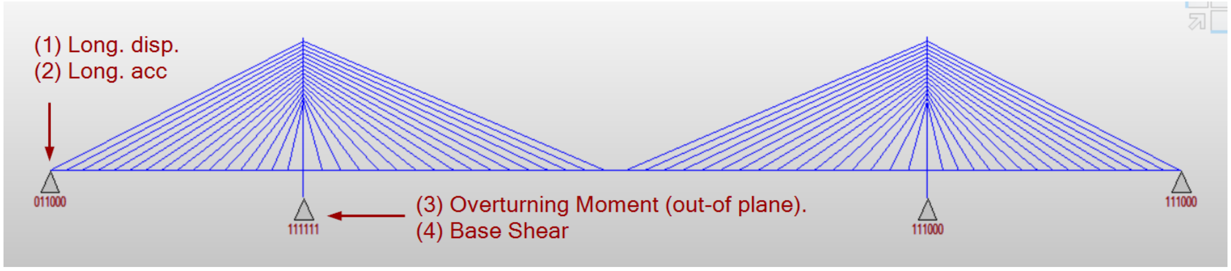

(a) Response quantities (1)-(5) used for the nonlinear response-history analysis.

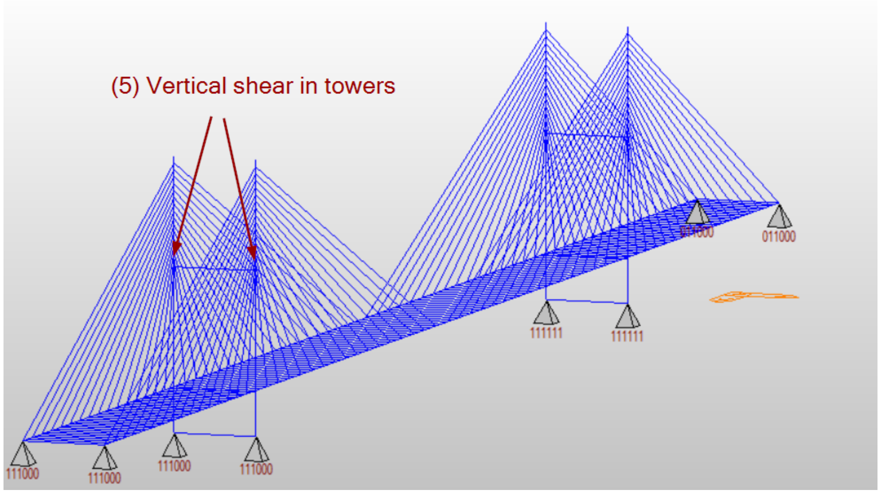

(b) Response quantity (6) transverse shear demand at both ends of the monitored beam.

Figure 5.2: Selected response quantities used to compare the nonretrofitted and retrofitted bridge models in the nonlinear response-history analyses.

For each ground motion, the response histories are presented in the following order: roller-support longitudinal displacement, roller-support longitudinal acceleration, tower overturning moment, tower base shear, and transverse shear in the tower beam. Displacements are reported in centimeters, accelerations in units of g, overturning moments in 10^6 kN m, and force resultants in 10^3 kN. For the displacement response, the plotted histories are measured with respect to the dead-load deformed configuration; therefore, the oscillatory response may fluctuate about a nonzero baseline rather than about the undeformed bridge configuration.

5.2.1 Base Case

The peak response quantites are summarized in **Table 5.1**:

Peak Response quantity	**Record**	**Nonretrofitted peak**	**Retrofitted peak**	**Change [%]**
Roller displacement, u_x [cm]	W1	25.15	10.99	-56.3
	W2	23.24	12.05	-48.2
	W3	24.75	16.91	-31.7
	W4	17.27	13.46	-22.1
	W5	11.94	10.26	-14.0
	E	4.83	5.22	7.9
Long. acc., a_x [g]	W1	1.82	0.93	-48.6
	W2	1.68	0.85	-49.4
	W3	1.77	1.25	-29.3
	W4	1.40	1.22	-13.3
	W5	1.02	0.77	-24.0
	E	0.14	0.18	29.6
Ovrt. moment, M_y [10^6 kN m]	W1	2.06	1.68	-18.3
	W2	2.30	1.54	-32.8
	W3	3.10	2.25	-27.2
	W4	2.16	1.92	-11.3
	W5	1.81	1.13	-37.6
	E	0.24	0.29	22.4
Tower base shear, V_b [10^3 kN]	W1	24.83	24.34	-2.0
	W2	21.51	22.51	4.6
	W3	38.95	40.48	3.9
	W4	29.83	30.11	0.9
	W5	33.15	33.78	1.9
	E	3.81	7.06	85.2
Tower-beam shear, V_z [10^3 kN]	W1	18.50	18.50	0.0
	W2	17.38	17.38	0.0
	W3	23.78	23.78	0.0
	W4	17.33	17.32	-0.1
	W5	23.60	23.61	0.1
	E	2.07	1.15	-44.2

Table 5.1: Peak absolute response comparison between the nonretrofitted bridge model and the bridge model retrofitted with nonlinear fluid viscous dampers. The maximum tower-beam shear is taken as the larger peak absolute value between elements E399 and E795 for each model. Negative percentage changes indicate a reduction after adding the fluid viscous dampers.

5.2.2 W1: 1999 Kocaeli, Turkey Earthquake Record at the Bursa Tofas Station

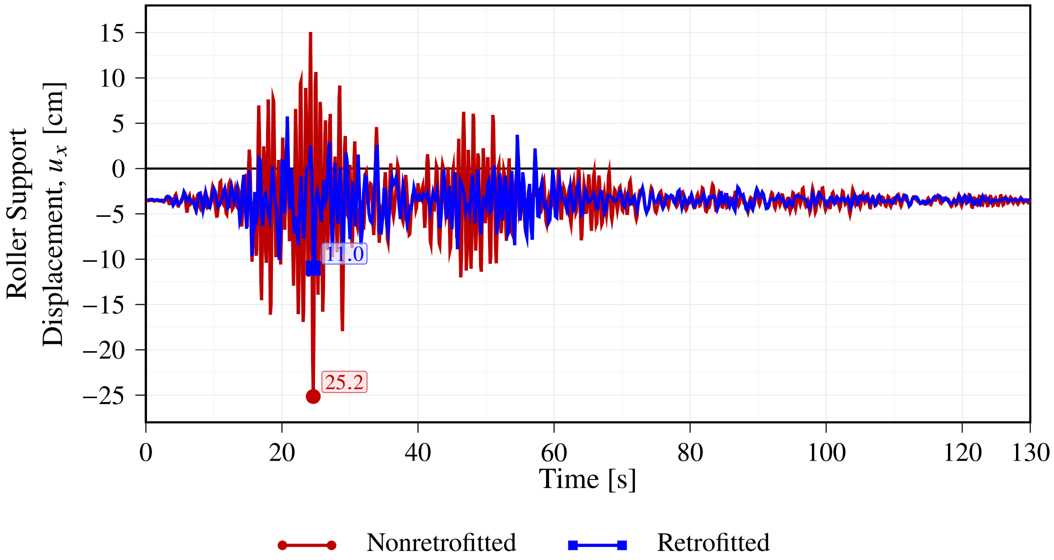

Figure 5.3: Time-history comparison of the longitudinal displacement at the roller support between the nonretrofitted and retrofitted bridge models under the 1999 Kocaeli, Turkey earthquake record at the Bursa Tofas station, plotted in centimeters. The oscillatory response is shifted by the displacement of the dead-load deformed configuration, so the motion fluctuates about a nonzero baseline rather than about the undeformed configuration.

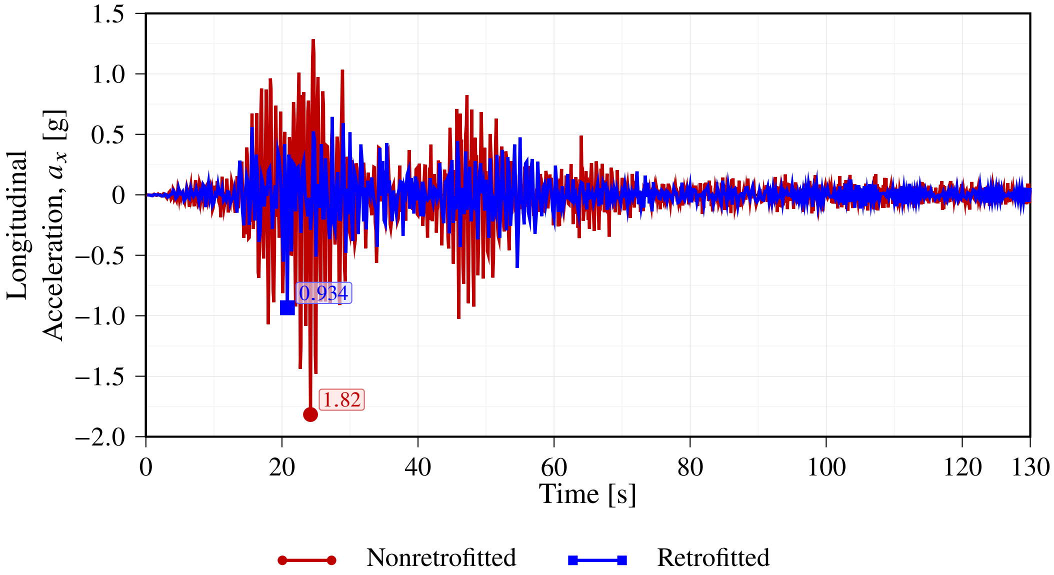

Figure 5.4: Time-history comparison of the longitudinal acceleration at the roller support between the nonretrofitted and retrofitted bridge models under the 1999 Kocaeli, Turkey earthquake record at the Bursa Tofas station, plotted in units of g.

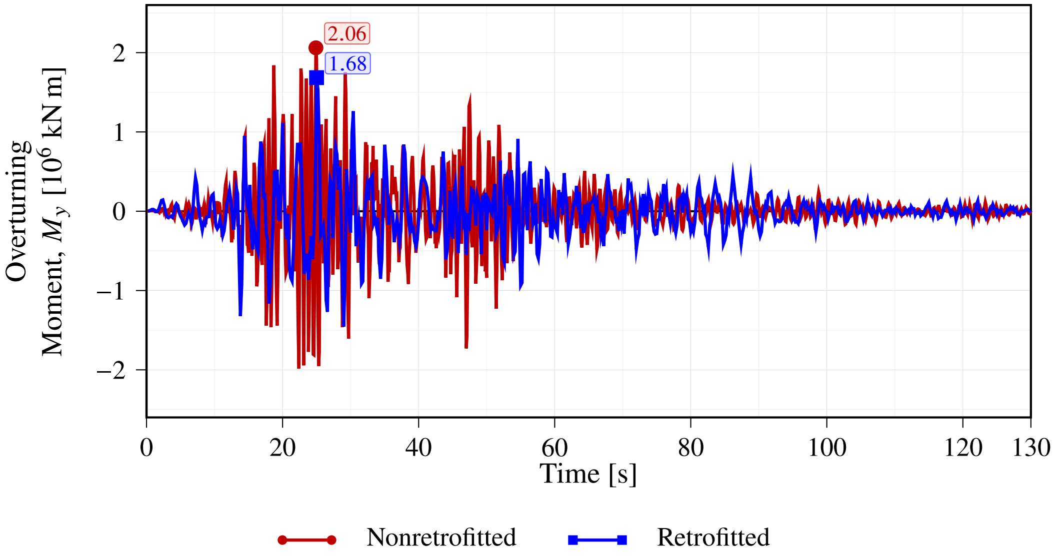

Figure 5.5: Time-history comparison of the overturning moment at Tower 1 between the nonretrofitted and retrofitted bridge models under the 1999 Kocaeli, Turkey earthquake record at the Bursa Tofas station.

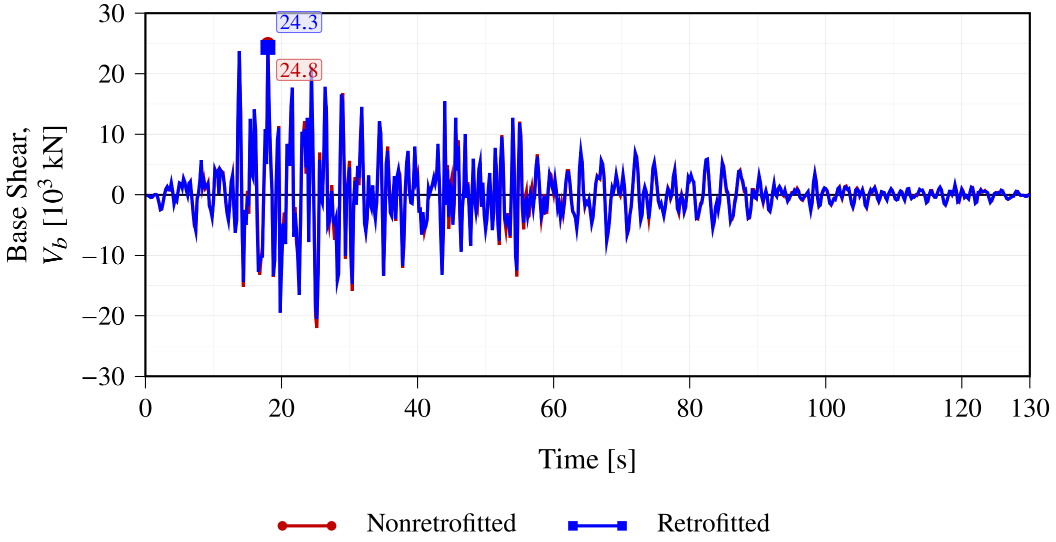

Figure 5.6: Time-history comparison of the base shear at Tower 1 between the nonretrofitted and retrofitted bridge models under the 1999 Kocaeli, Turkey earthquake record at the Bursa Tofas station.

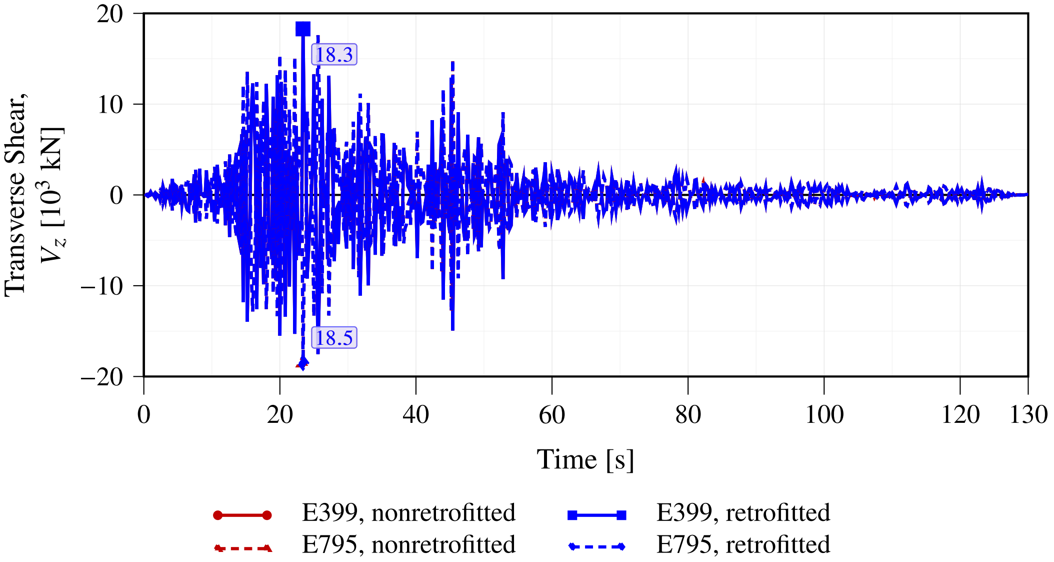

Figure 5.7: Time-history comparison of the transverse shear in the tower beam at elements E399 and E795 for the nonretrofitted and retrofitted bridge models under the 1999 Kocaeli, Turkey earthquake record at the Bursa Tofas station.

5.2.3 W2: 1999 Chi-Chi, Taiwan Earthquake Record at the CHY004 Station

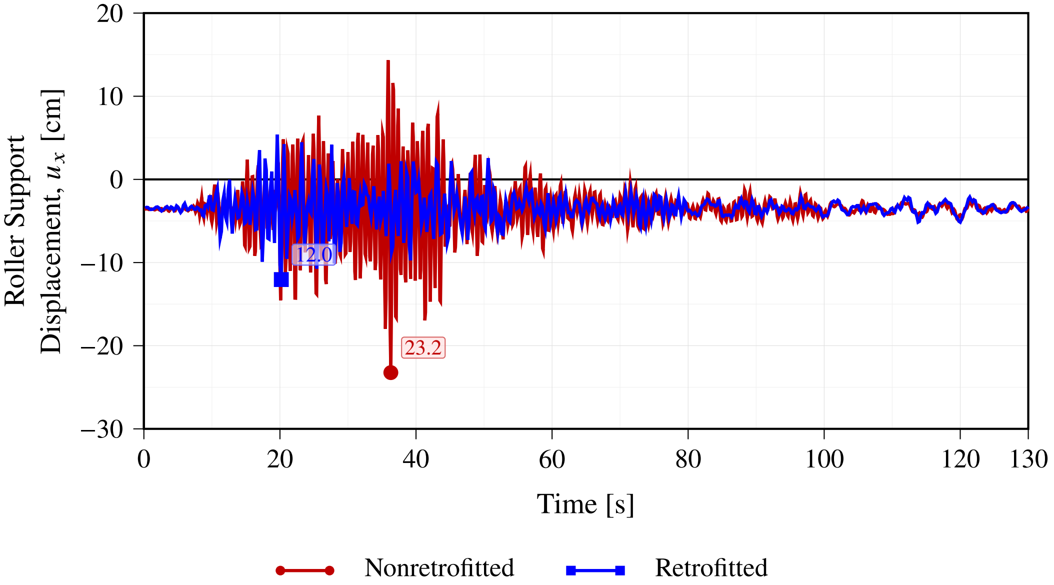

Figure 5.8: Time-history comparison of the longitudinal displacement at the roller support between the nonretrofitted and retrofitted bridge models under the 1999 Chi-Chi, Taiwan earthquake record at the CHY004 station, plotted in centimeters. The oscillatory response is shifted by the displacement of the dead-load deformed configuration, so the motion fluctuates about a nonzero baseline rather than about the undeformed configuration.

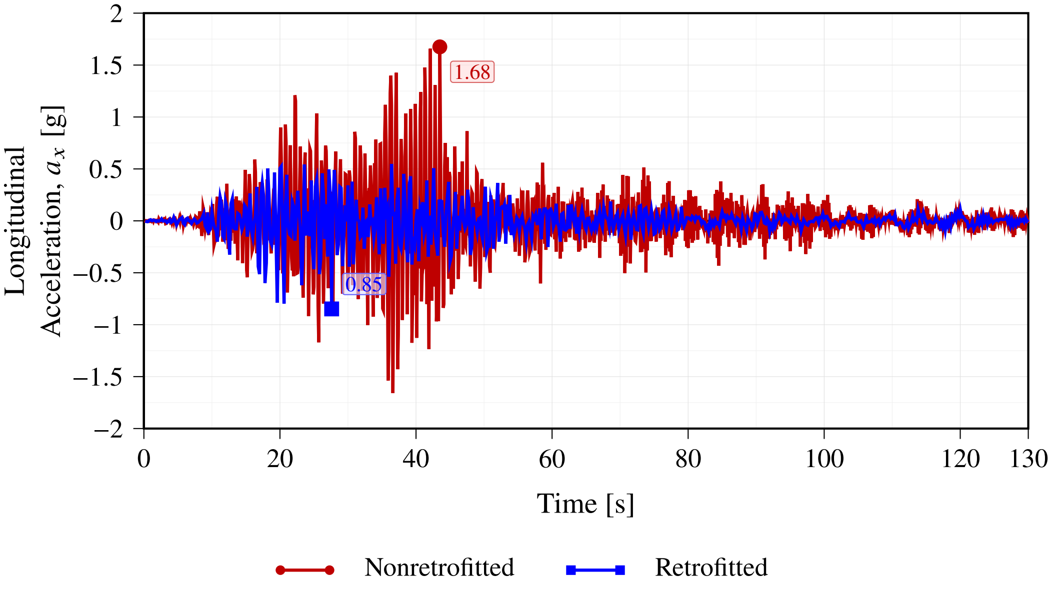

Figure 5.9: Time-history comparison of the longitudinal acceleration at the roller support between the nonretrofitted and retrofitted bridge models under the 1999 Chi-Chi, Taiwan earthquake record at the CHY004 station, plotted in units of g.

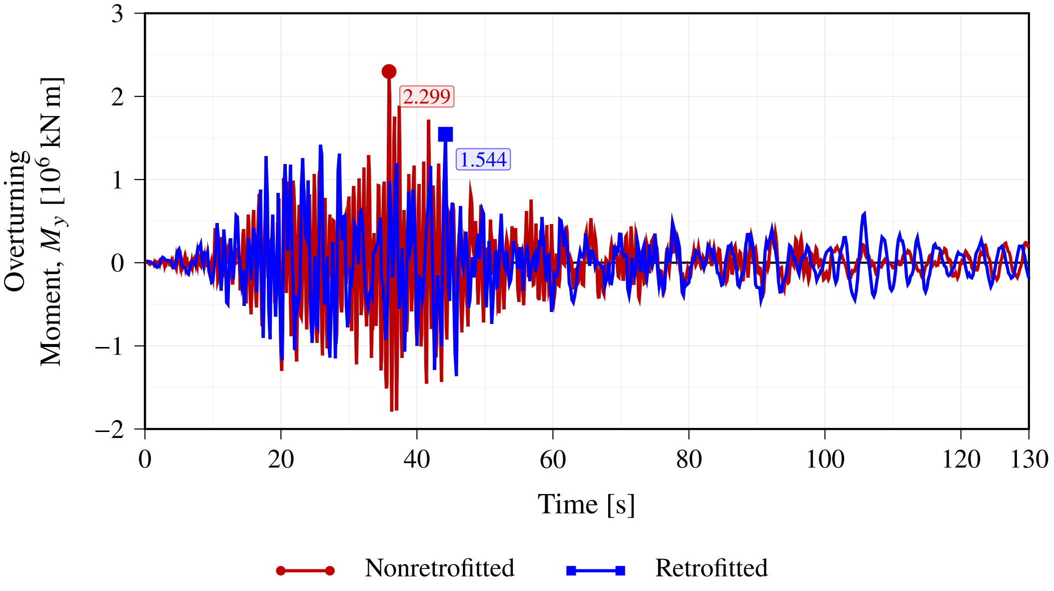

Figure 5.10: Time-history comparison of the overturning moment at Tower 1 between the nonretrofitted and retrofitted bridge models under the 1999 Chi-Chi, Taiwan earthquake record at the CHY004 station.

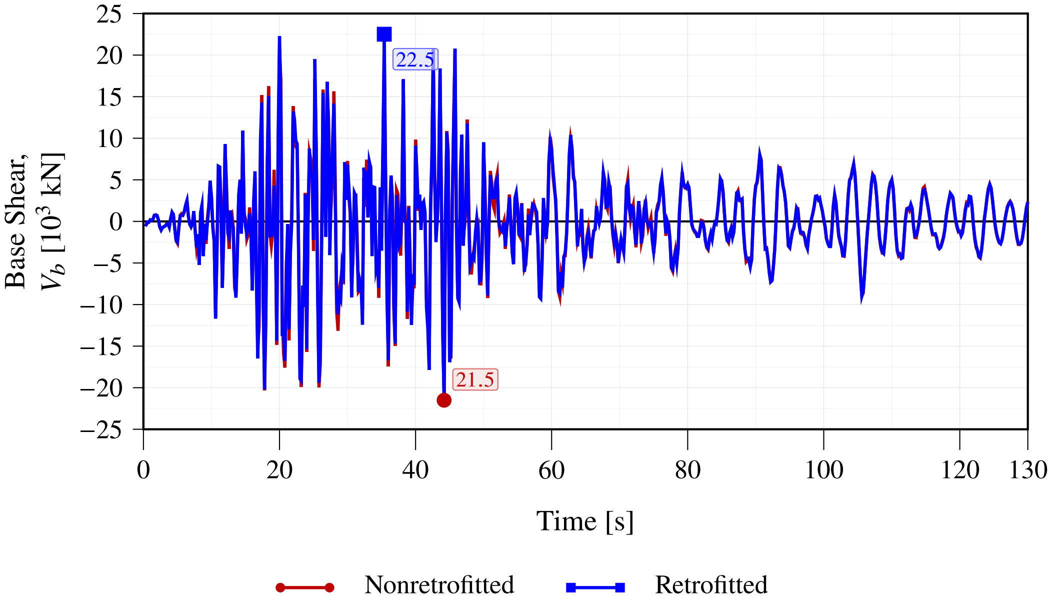

Figure 5.11: Time-history comparison of the base shear at Tower 1 between the nonretrofitted and retrofitted bridge models under the 1999 Chi-Chi, Taiwan earthquake record at station TCU052.

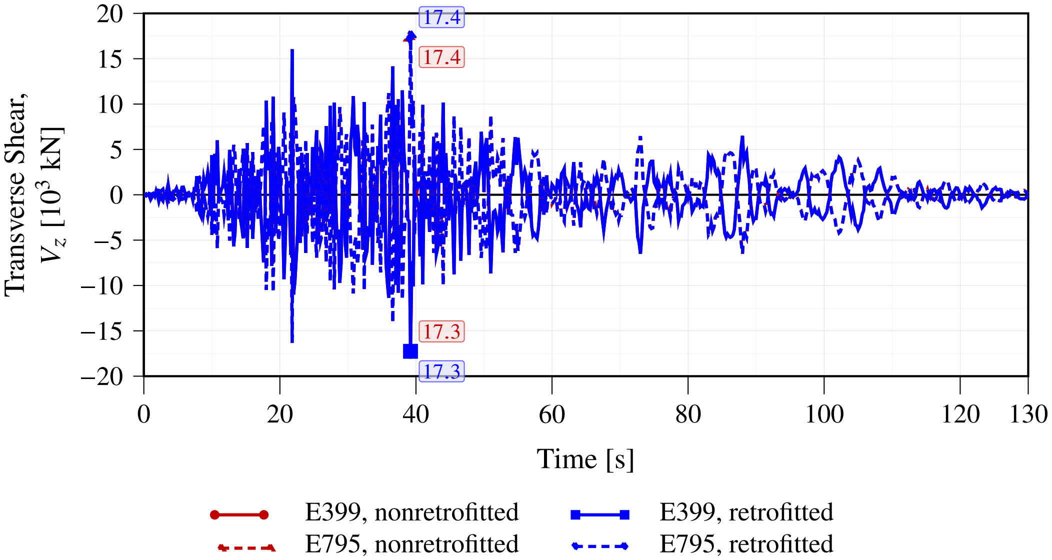

Figure 5.12: Time-history comparison of the transverse shear in the tower beam at elements E399 and E795 for the nonretrofitted and retrofitted bridge models under the 1999 Chi-Chi, Taiwan earthquake record at station TCU052.

5.2.4 W3: 1999 Chi-Chi, Taiwan Earthquake Record at the CHY065 Station

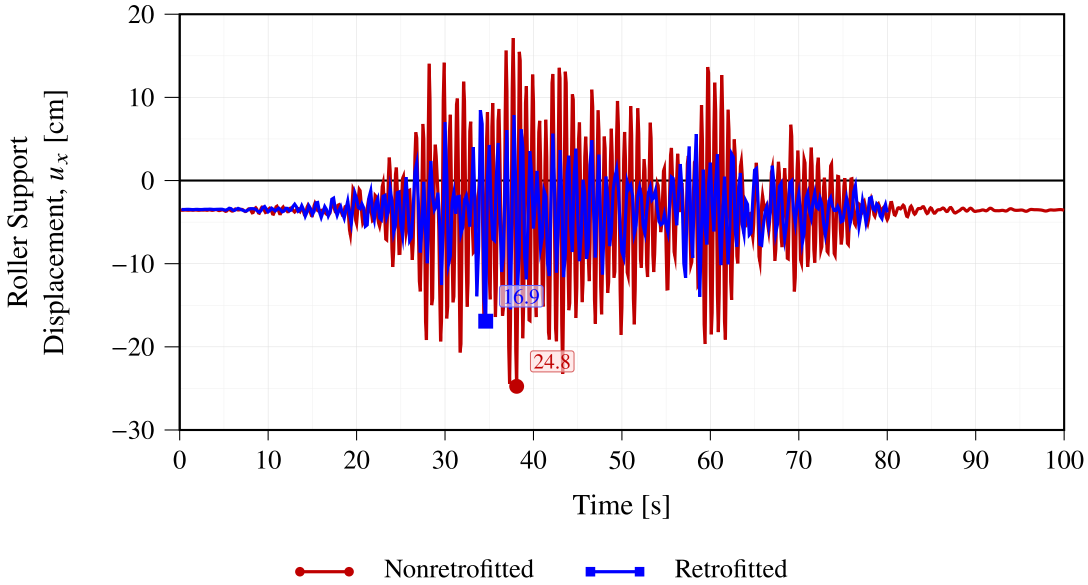

Figure 5.13: Time-history comparison of the longitudinal displacement at the roller support between the nonretrofitted and retrofitted bridge models under the selected W3 ground-motion record, plotted in centimeters. The oscillatory response is shifted by the displacement of the dead-load deformed configuration, so the motion fluctuates about a nonzero baseline rather than about the undeformed configuration.

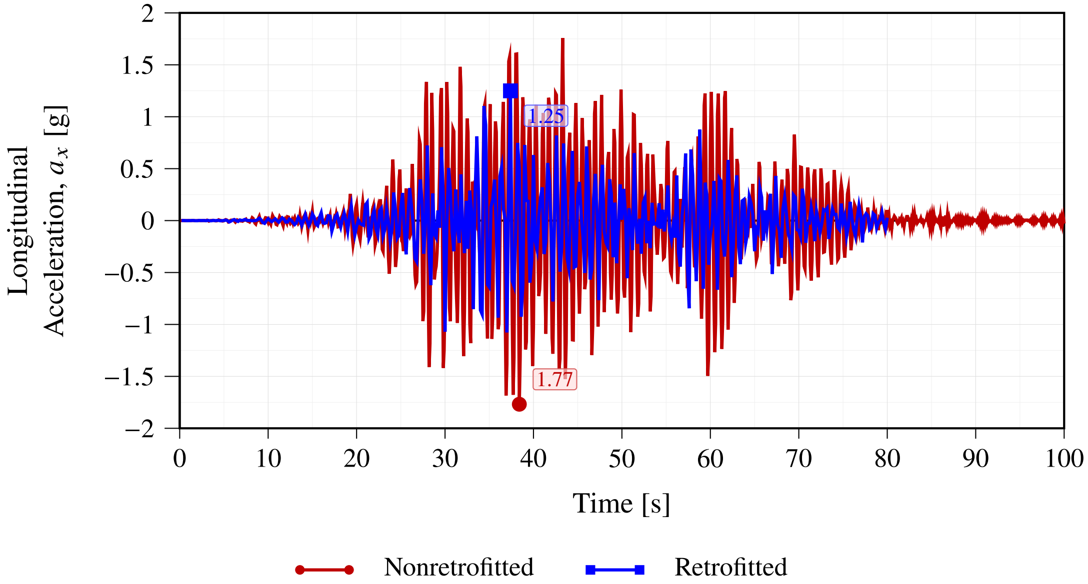

Figure 5.14: Time-history comparison of the longitudinal acceleration at the roller support between the nonretrofitted and retrofitted bridge models under the selected W3 ground-motion record, plotted in units of g.

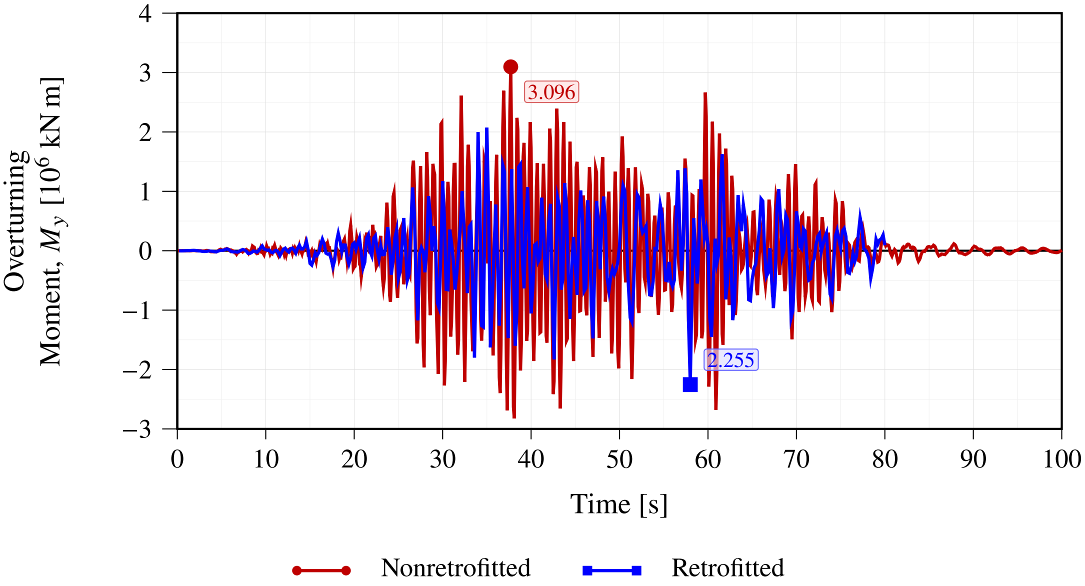

Figure 5.15: Time-history comparison of the overturning moment at Tower 1 between the nonretrofitted and retrofitted bridge models under the selected W3 ground-motion record.

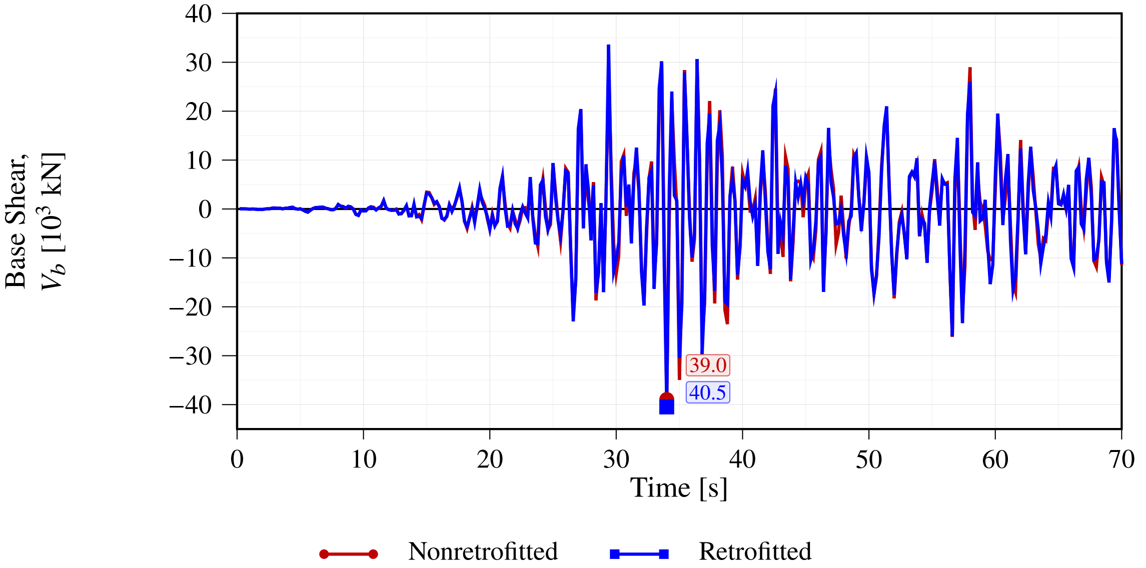

Figure 5.16: Time-history comparison of the base shear at Tower 1 between the nonretrofitted and retrofitted bridge models under the selected W3 ground-motion record.

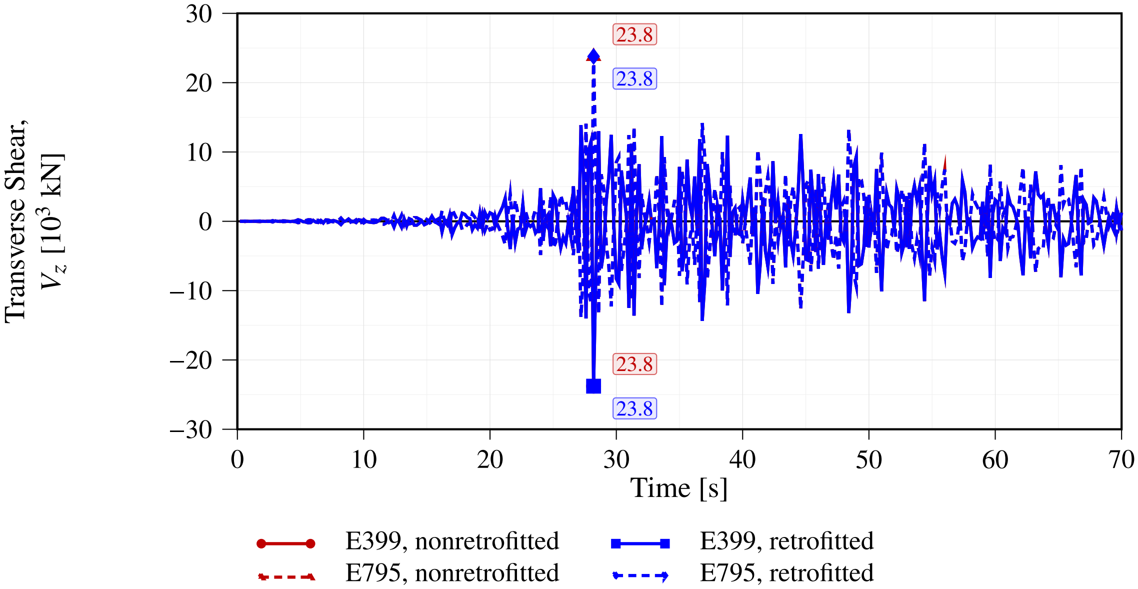

Figure 5.17: Time-history comparison of the transverse shear in the tower beam at elements E399 and E795 for the nonretrofitted and retrofitted bridge models under the selected W3 ground-motion record.

5.2.5 W4: 1990 Manjil, Iran Earthquake Record at the Rudsar Station

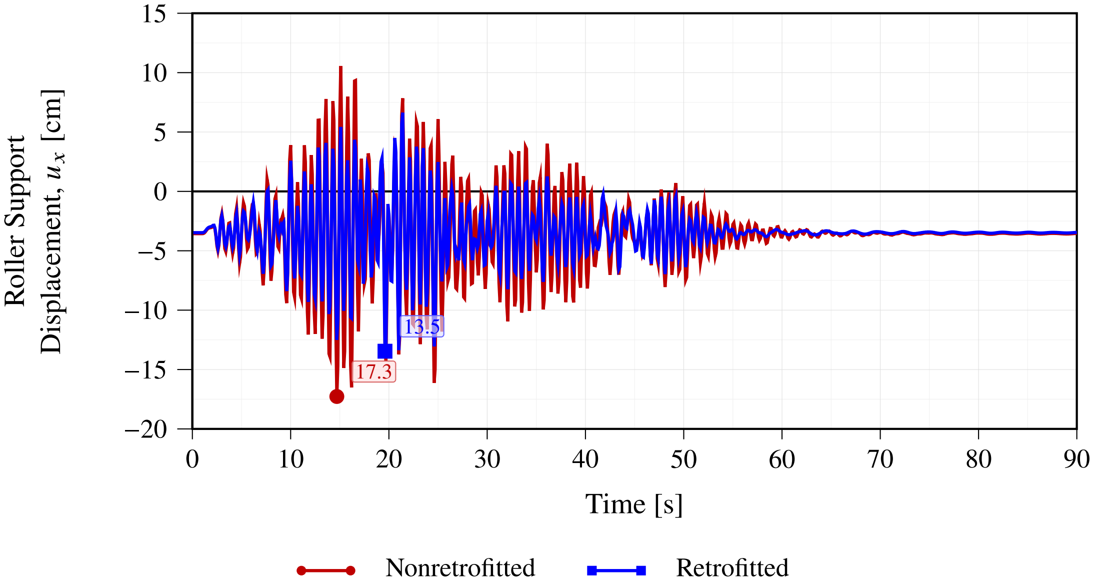

Figure 5.18: Time-history comparison of the longitudinal displacement at the roller support between the nonretrofitted and retrofitted bridge models under the 1990 Manjil, Iran earthquake record at the Rudsar station, plotted in centimeters. The oscillatory response is shifted by the displacement of the dead-load deformed configuration, so the motion fluctuates about a nonzero baseline rather than about the undeformed configuration.

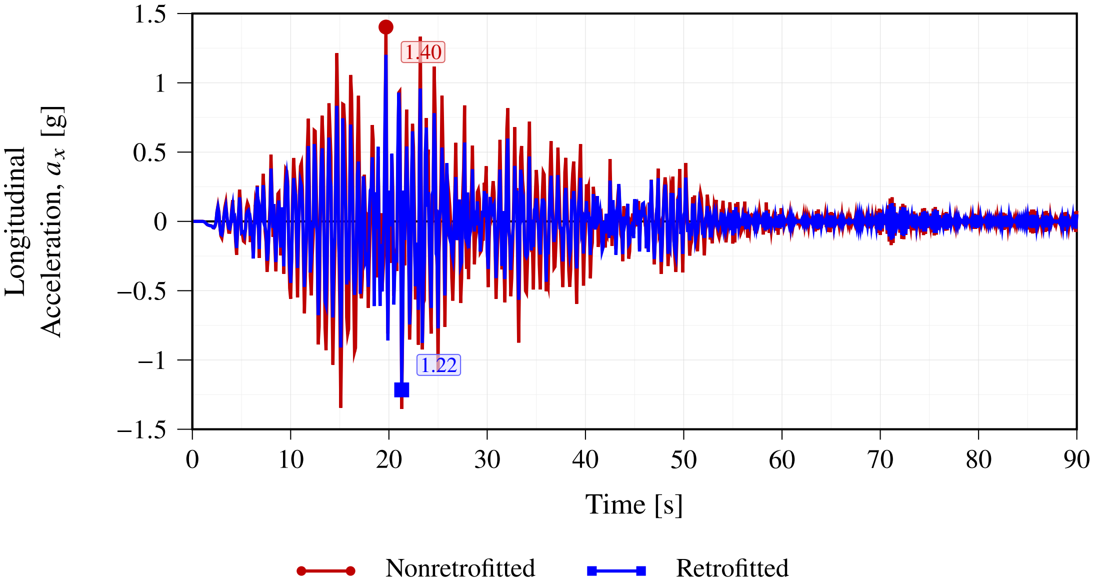

Figure 5.19: Time-history comparison of the longitudinal acceleration at the roller support between the nonretrofitted and retrofitted bridge models under the 1990 Manjil, Iran earthquake record at the Rudsar station, plotted in units of g.

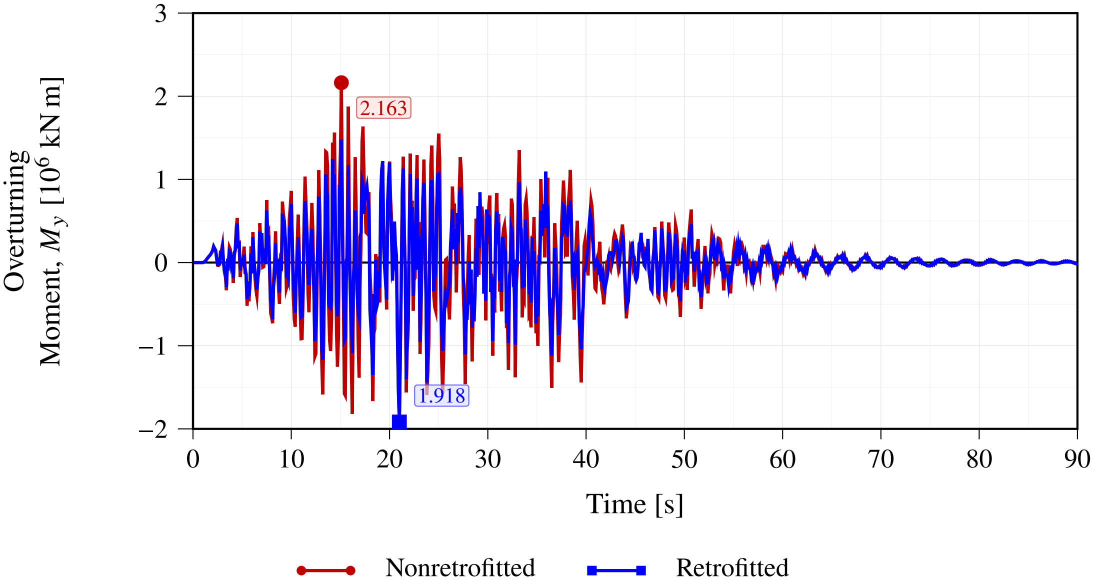

Figure 5.20: Time-history comparison of the overturning moment at Tower 1 between the nonretrofitted and retrofitted bridge models under the 1990 Manjil, Iran earthquake record at the Rudsar station.

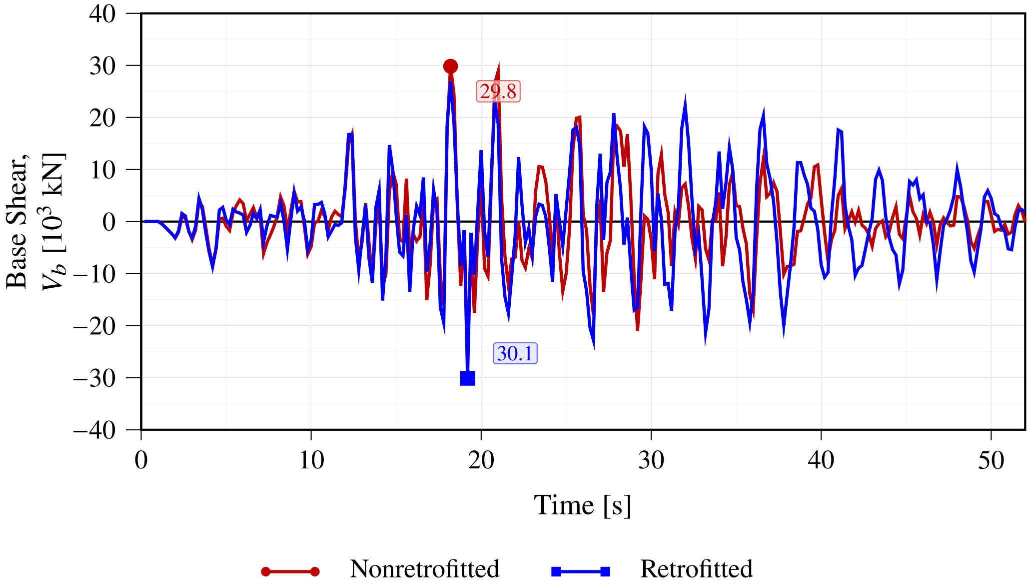

Figure 5.21: Time-history comparison of the base shear at Tower 1 between the nonretrofitted and retrofitted bridge models under the 1990 Manjil, Iran earthquake record at the Rudsar station.

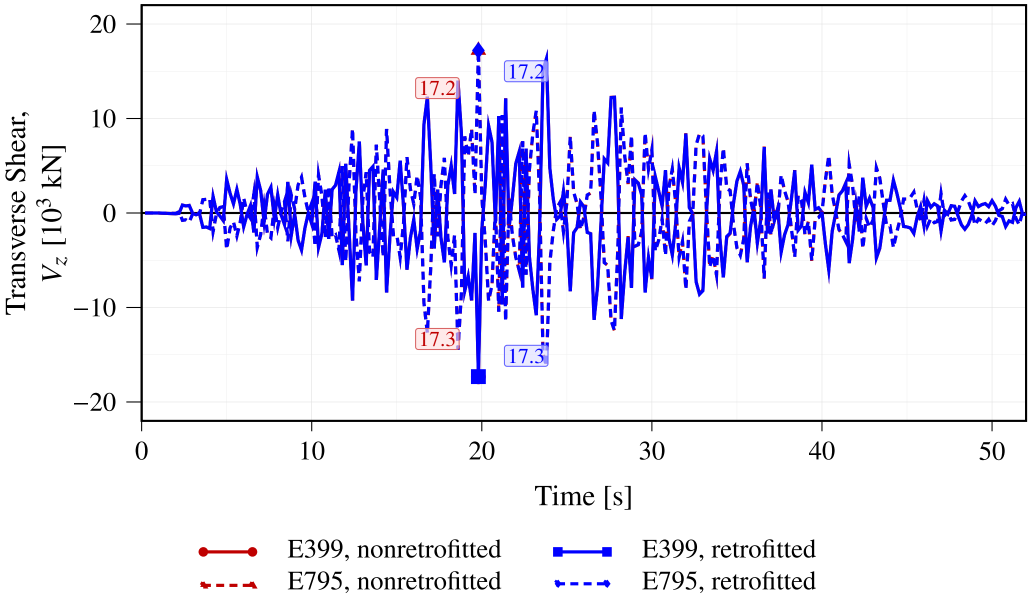

Figure 5.22: Time-history comparison of the transverse shear in the tower beam at elements E399 and E795 for the nonretrofitted and retrofitted bridge models under the 1990 Manjil, Iran earthquake record at the Rudsar station.

5.2.6 W5: 2002 Denali, Alaska Earthquake Record at Station R109 (temp)

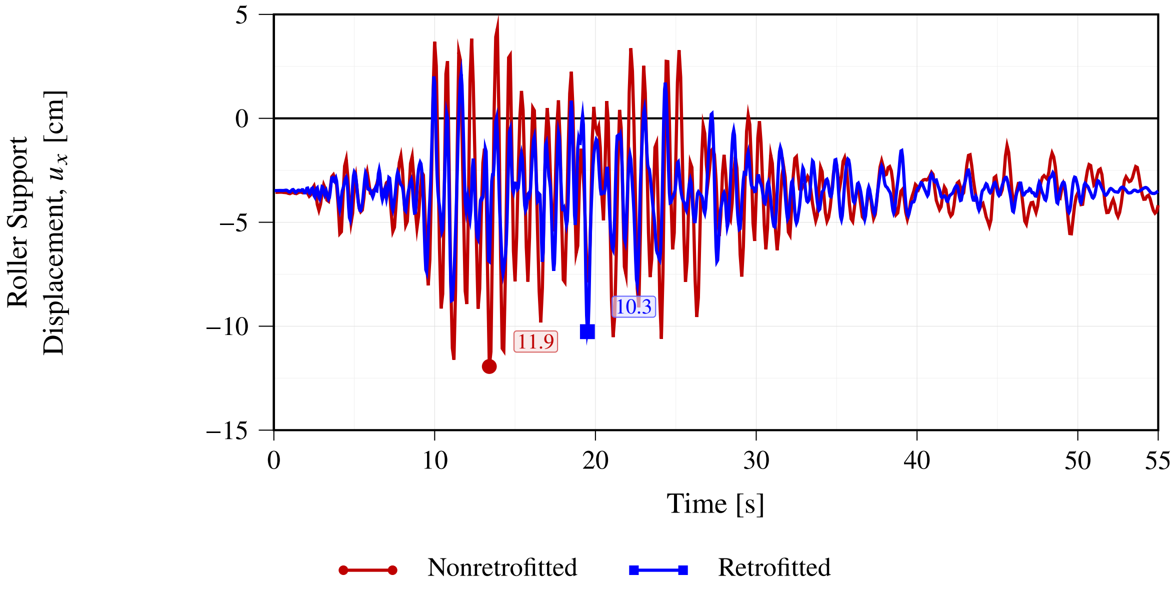

Figure 5.23: Time-history comparison of the longitudinal displacement at the roller support between the nonretrofitted and retrofitted bridge models under the 2011 Sparks, Oklahoma earthquake record at station GS.OK009, plotted in centimeters. The oscillatory response is shifted by the displacement of the dead-load deformed configuration, so the motion fluctuates about a nonzero baseline rather than about the undeformed configuration.

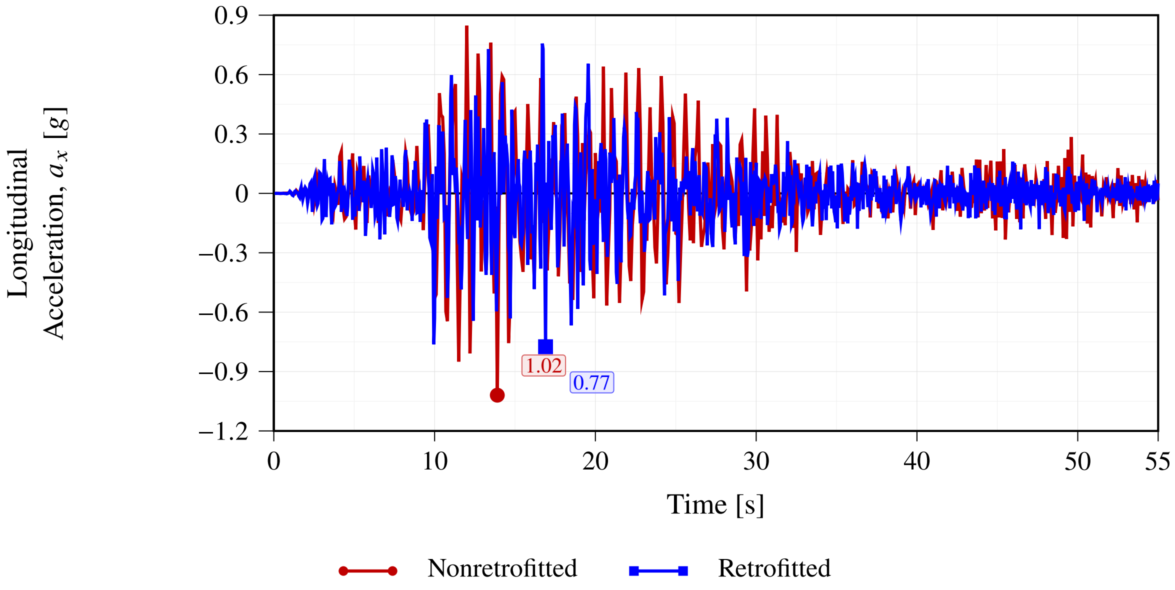

Figure 5.24: Time-history comparison of the longitudinal acceleration at the roller support between the nonretrofitted and retrofitted bridge models under the 2011 Sparks, Oklahoma earthquake record at station GS.OK009, plotted in units of g.

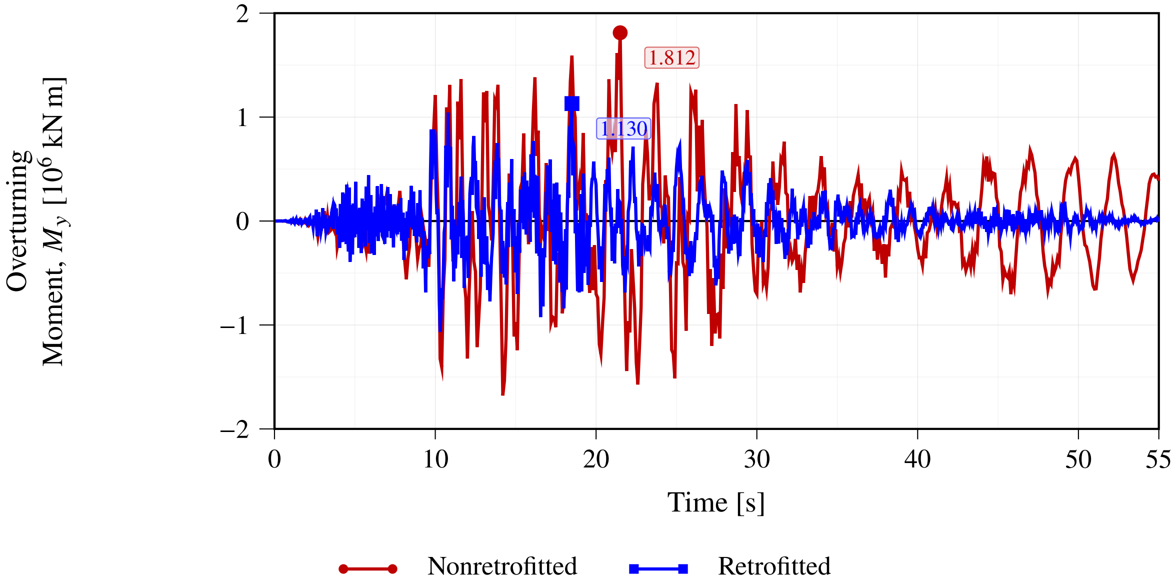

Figure 5.25: Time-history comparison of the overturning moment at Tower 1 between the nonretrofitted and retrofitted bridge models under the 2011 Sparks, Oklahoma earthquake record at station GS.OK009.

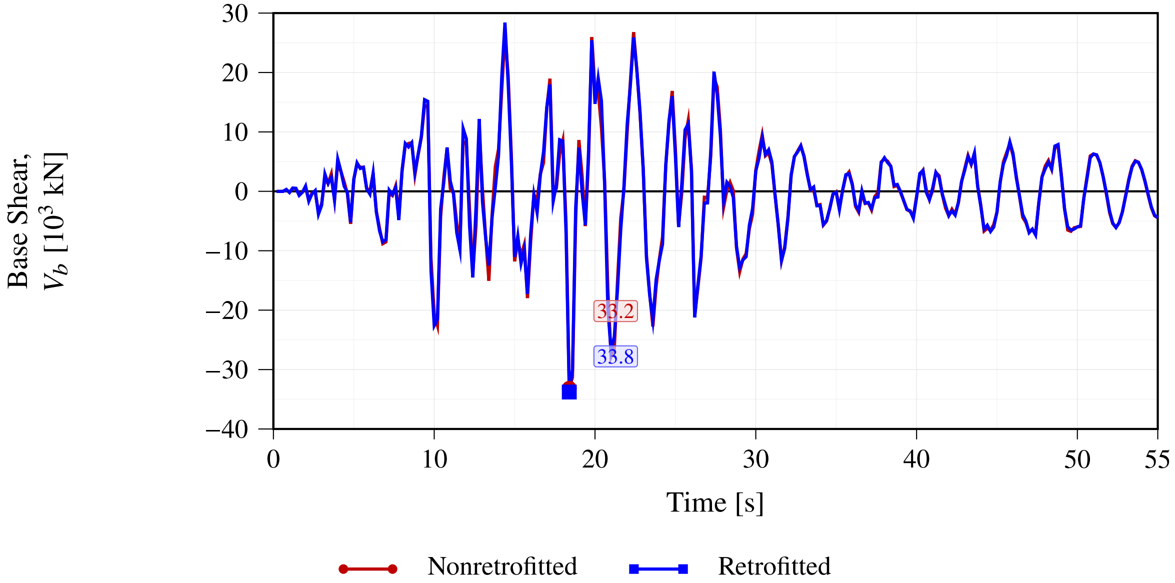

Figure 5.26: Time-history comparison of the base shear at Tower 1 between the nonretrofitted and retrofitted bridge models under the 2011 Sparks, Oklahoma earthquake record at station GS.OK009.

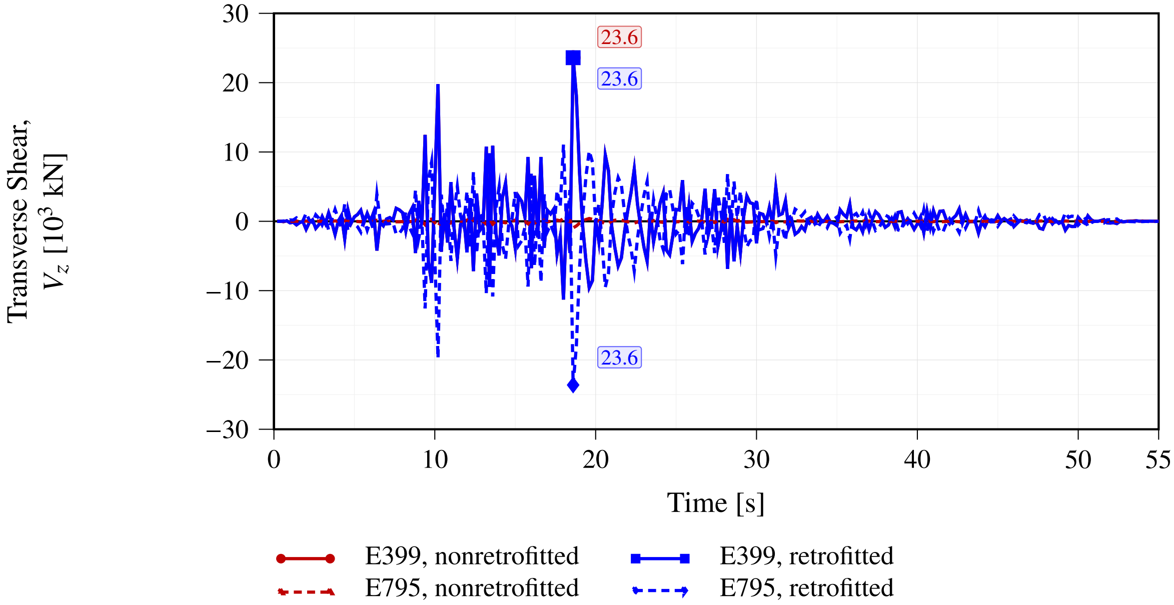

Figure 5.27: Time-history comparison of the transverse shear in the tower beam at elements E399 and E795 for the nonretrofitted and retrofitted bridge models under the 2011 Sparks, Oklahoma earthquake record at station GS.OK009.

5.2.7 E: 2011 Mineral, Virginia Earthquake Record at Station NP.2555, East Component

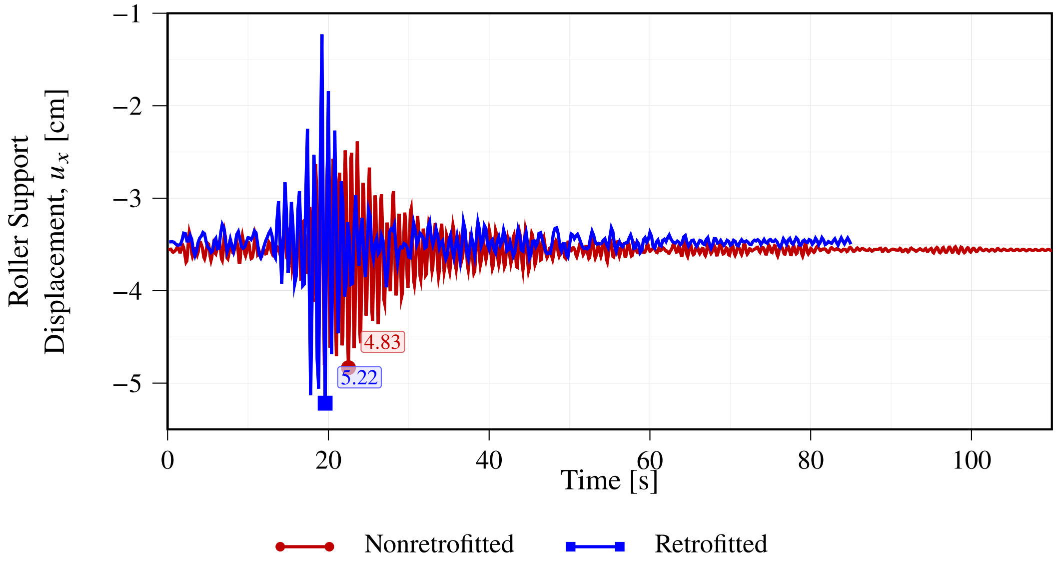

Figure 5.28: Time-history comparison of the longitudinal displacement at the roller support between the nonretrofitted and retrofitted bridge models under the 2011 Mineral, Virginia earthquake record at station NP.2555, east component, plotted in centimeters. The oscillatory response is shifted by the displacement of the dead-load deformed configuration, so the motion fluctuates about a nonzero baseline rather than about the undeformed configuration.

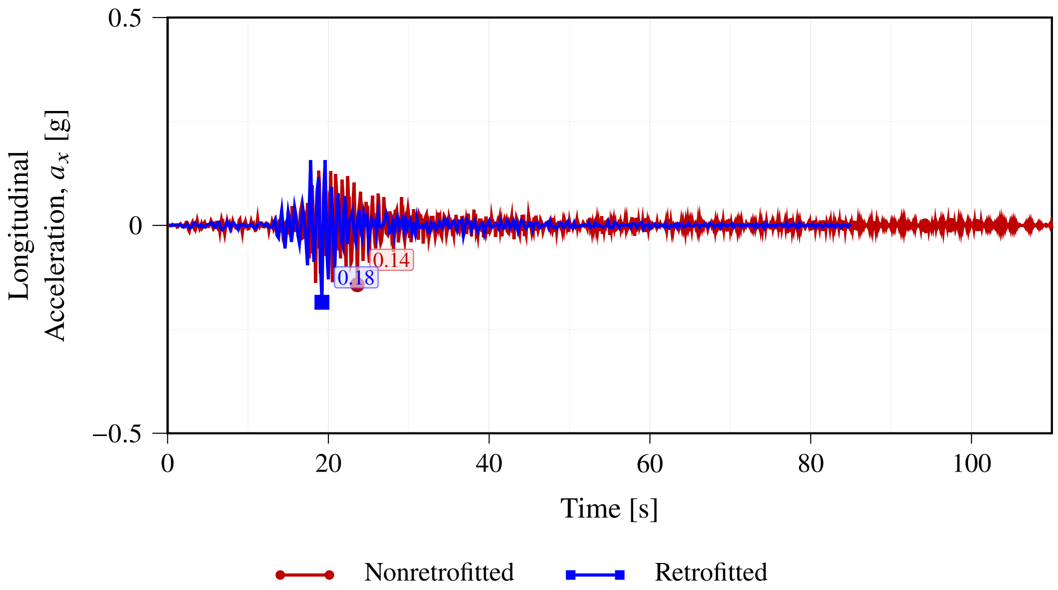

Figure 5.29: Time-history comparison of the longitudinal acceleration at the roller support between the nonretrofitted and retrofitted bridge models under the 2011 Mineral, Virginia earthquake record at station NP.2555, east component, plotted in units of g.

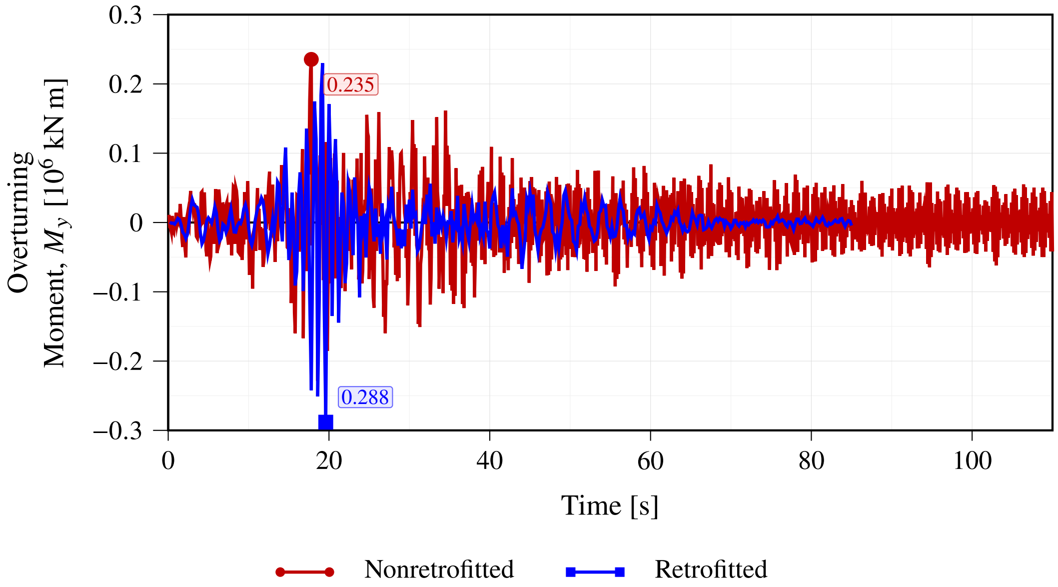

Figure 5.30: Time-history comparison of the overturning moment at Tower 1 between the nonretrofitted and retrofitted bridge models under the 2011 Mineral, Virginia earthquake record at station NP.2555, east component.

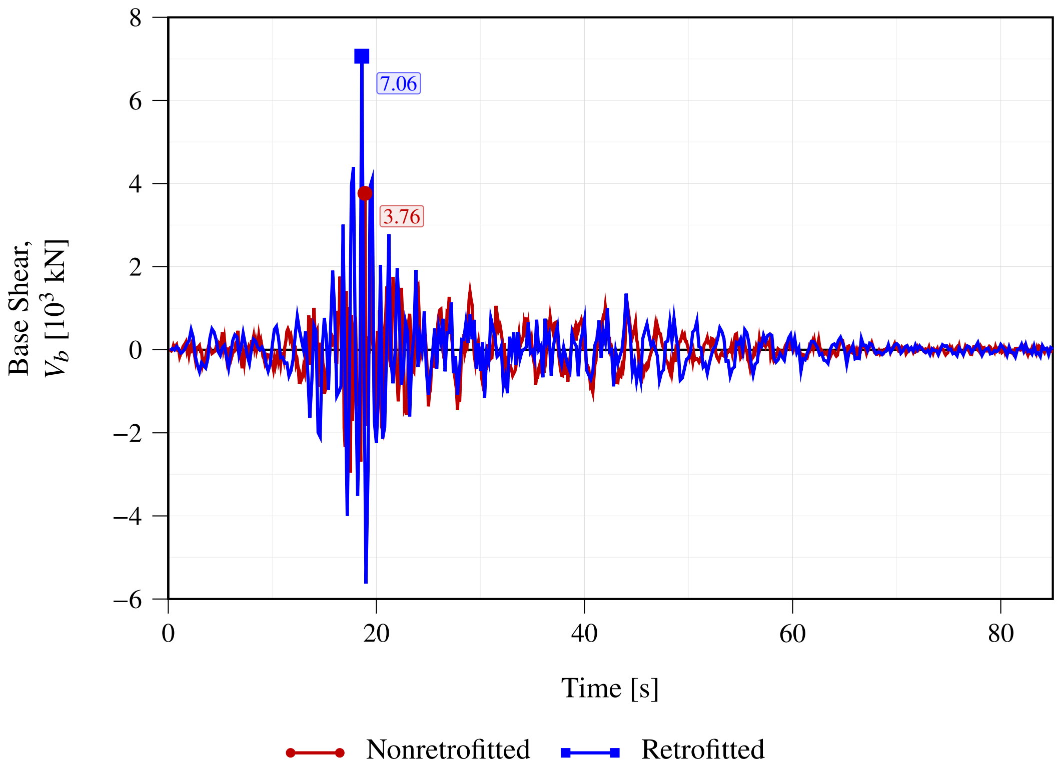

Figure 5.31: Time-history comparison of the base shear at Tower 1 between the nonretrofitted and retrofitted bridge models under the 2011 Mineral, Virginia earthquake record at station NP.2555, east component. No shaded late-time region is highlighted in this plot because the base-shear response does not show the same clearly persistent underdamped numerical integration oscillation observed in the transverse-shear response.

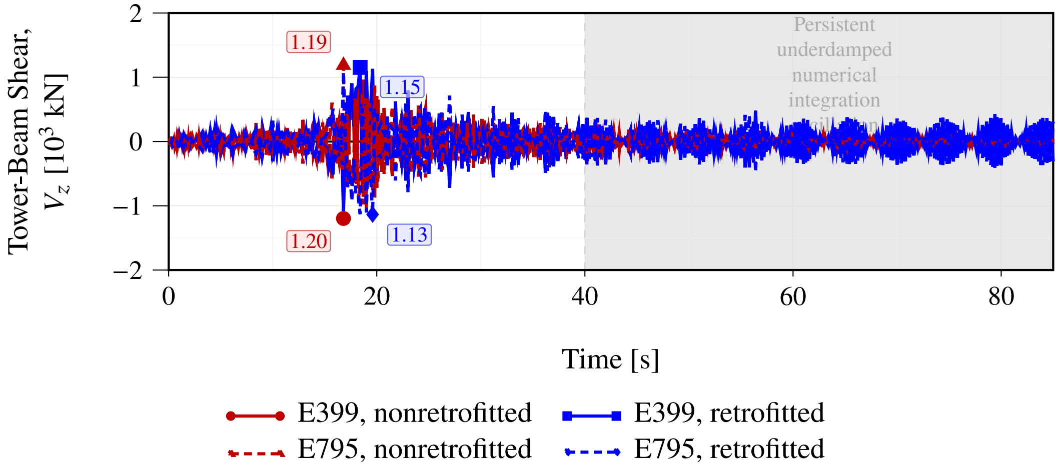

Figure 5.32: Time-history comparison of the transverse shear in the tower beam at elements E399 and E795 for the nonretrofitted and retrofitted bridge models under the 2011 Mineral, Virginia earthquake record at station NP.2555, east component. The shaded interval highlights the late-time portion interpreted as a persistent underdamped numerical integration oscillation.

5.2.8 Alternative Linear Viscous Damper Case

The results for the peak quantities for the equivalent linear system are presented in **Table 5.2**.

Peak response quantity	**R**	**Nonretrofitted peak**	$\alpha = 0.40$ **peak**	$\Delta_{0.40}$ **[%]**	$\alpha = 1.00$ **peak**	$\Delta_{1.00}$ **[%]**
Roller disp., u_x [cm]	W1	25.15	10.99	-56.3	10.50	-58.3
	W2	23.24	12.05	-48.2	11.25	-51.6
	W3	24.75	16.91	-31.7	15.23	-38.5
	W4	17.27	13.46	-22.1	11.61	-32.8
	W5	11.94	8.77	-26.5	10.14	-15.1
Long. acc., a_x [g]	W1	1.82	0.93	-48.6	0.87	-51.8
	W2	1.68	0.85	-49.4	0.71	-57.7
	W3	1.77	1.25	-29.3	1.19	-32.7
	W4	1.40	1.22	-13.3	0.73	-47.7
	W5	1.02	0.76	-25.2	0.53	-47.6
Ovrt. moment, M_y [10^6 kN m]	W1	2.06	1.68	-18.3	1.64	-20.5
	W2	2.30	1.54	-32.8	1.56	-32.3
	W3	3.10	2.25	-27.2	2.09	-32.6
	W4	2.16	1.92	-11.3	1.84	-14.8
	W5	1.81	1.07	-41.1	2.31	27.5
Tower base shear, V_b [10^3 kN]	W1	37.52	27.76	-26.0	28.16	-24.9
	W2	42.43	28.07	-33.8	28.89	-31.9
	W3	57.23	47.87	-16.3	50.01	-12.6
	W4	36.87	36.71	-0.5	33.31	-9.7
	W5	33.14	46.29	39.7	45.22	36.4
Tower-beam shear, V_z [10^3 kN]	W1	27.91	22.04	-21.0	22.04	-21.0
	W2	42.43	17.43	-58.9	17.43	-58.9
	W3	27.10	23.62	-12.9	23.62	-12.9
	W4	40.42	40.42	0.0	20.09	-50.3
	W5	33.65	48.95	45.5	55.50	64.9

Table 5.2: Peak absolute response comparison among the nonretrofitted bridge model, the nonlinear fluid viscous damper retrofit with $\alpha = 0.40$, and the linear damper retrofit with $\alpha = 1.00$. The percentage changes $\Delta_{0.40}$ and $\Delta_{1.00}$ are computed with respect to the nonretrofitted peak response. The maximum tower-beam shear is taken as the larger peak absolute value between elements E399 and E795 for each model. Negative percentage changes indicate a reduction with respect to the nonretrofitted model.

5.2.9 Bounded Analysis of the Damper Coefficient

Lastly, the bounded analysis peak responses are summarized from **Fig. 5.33** to **Fig. 5.37**

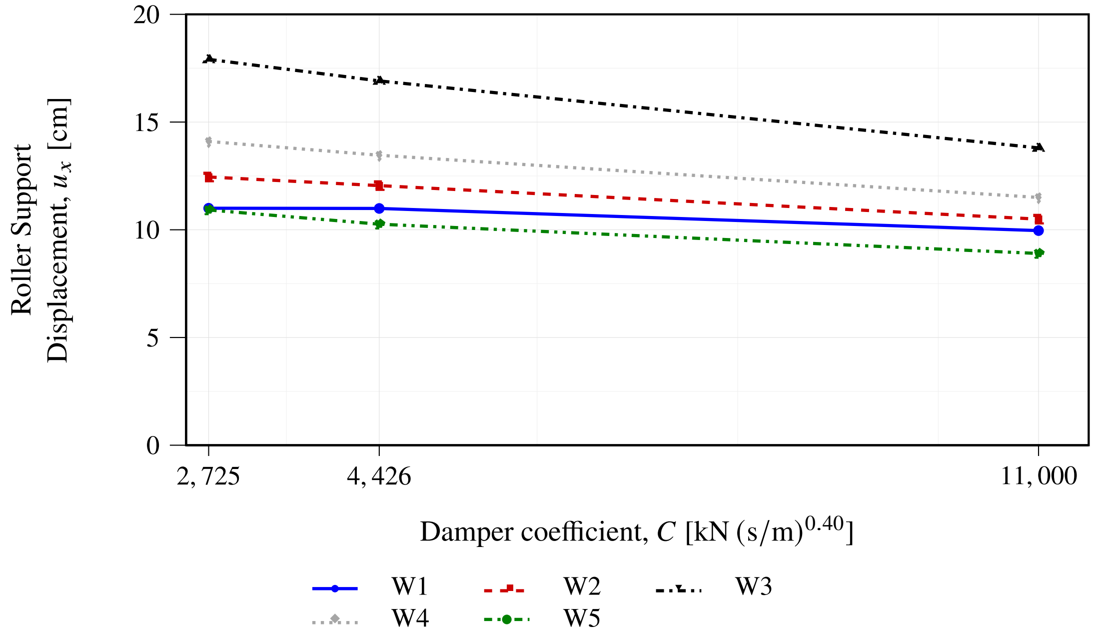

Figure 5.33: Bounded analysis of the damper coefficient C for the roller-support longitudinal displacement.

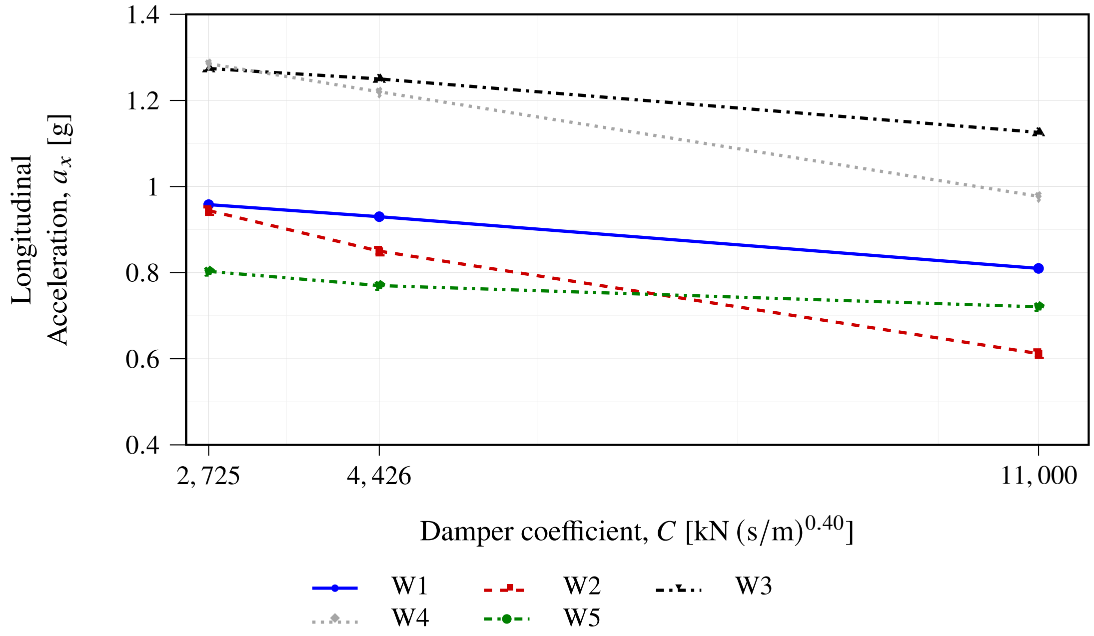

Figure 5.34: Bounded analysis of the damper coefficient C for the longitudinal acceleration at the roller support.

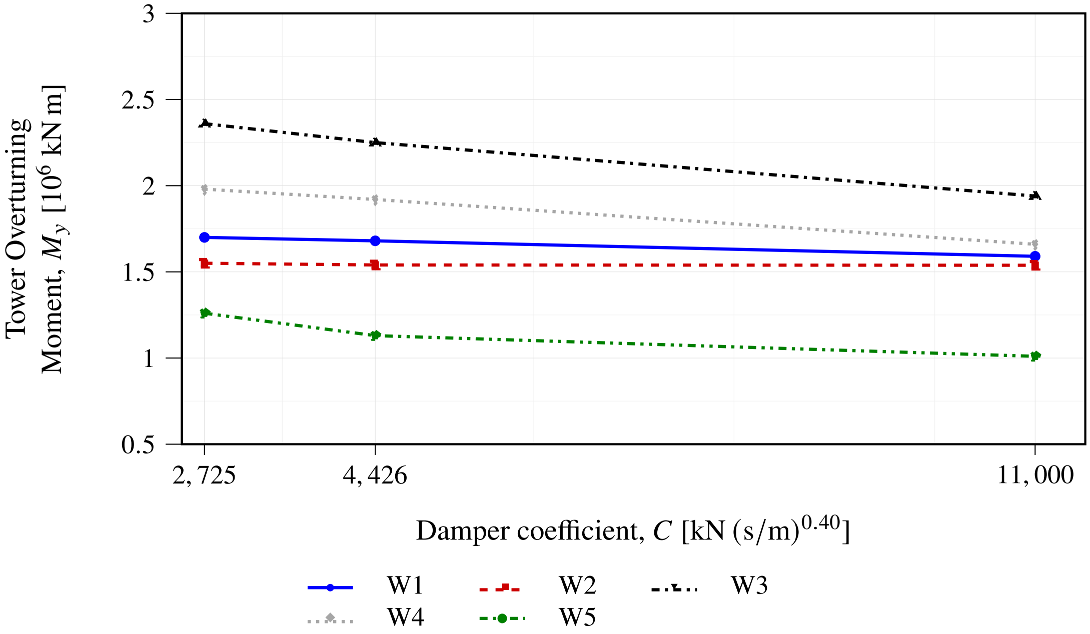

Figure 5.35: Bounded analysis of the damper coefficient C for the tower overturning moment.

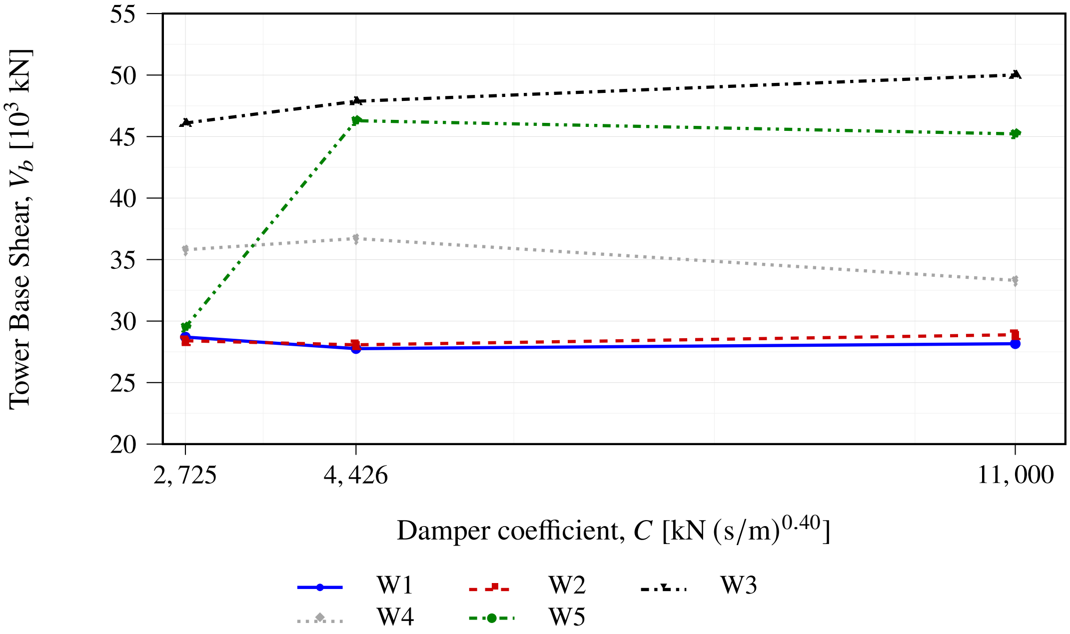

Figure 5.36: Bounded analysis of the damper coefficient C for the tower base shear.

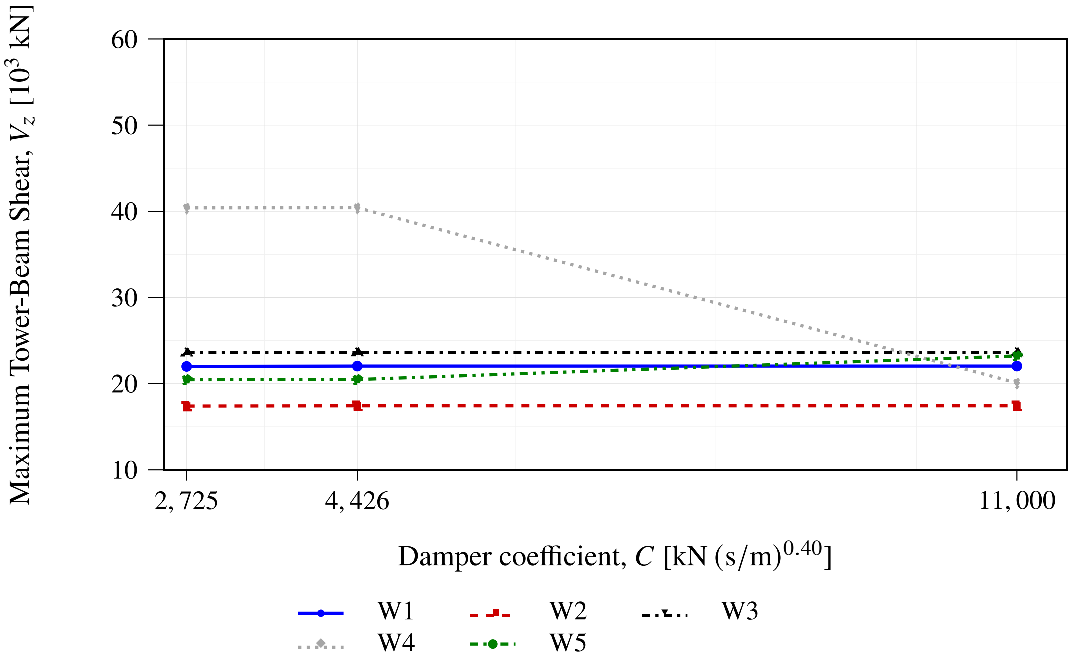

Figure 5.37: Bounded analysis of the damper coefficient C for the maximum tower-beam shear.

.

6 Discussion on Results: Influence of Fluid Viscous Dampers on Seismic Response

6.1 Response Histories Comparison for C=4446 α=0.40

The corresponding time-history comparisons are shown in **Fig. 5.3–Fig. 5.7**, **Fig. 5.8–Fig. 5.12**, **Fig. 5.13–Fig. 5.17**, **Fig. 5.18–Fig. 5.22**, **Fig. 5.23–Fig. 5.27**, and **Fig. 5.28–Fig. 5.32**. The peak absolute values extracted from these figures are summarized in **Table 5.1**. This section will focus on discussing the results.

6.1.1 Reduction of Longitudinal Displacement and Acceleration

The results show that the longitudinal fluid viscous dampers are generally effective in reducing the global longitudinal response of the bridge. For the W1–W5 records, the peak longitudinal displacement at the roller support is reduced in every case. The largest reduction occurs for W1, where the peak displacement decreases from 25.15 cm to 10.99 cm, while the smallest reduction occurs for W5, where the peak displacement decreases from 11.94 cm to 10.26 cm.

The same general trend is observed for the longitudinal acceleration, which is also reduced for all W-series records. These results indicate that the dampers provide a consistent source of energy dissipation in the longitudinal direction and reduce the response quantities most directly associated with deck motion.

6.1.2 Effect on Tower Overturning Moment

The reduction in longitudinal response also propagates to the overturning moment at Tower 1. This behavior is mechanically consistent with the force-transfer path of the cable-stayed bridge. Longitudinal deck motion is transferred through the deck–cable–tower system; consequently, a reduction in deck motion also reduces the dynamic demand transmitted to the towers.

For the W1–W5 records, the peak overturning moment is reduced in every case, with reductions ranging from approximately 11.3% for W4 to 37.6% for W5. This confirms that the dampers do not only reduce a local support displacement but also influence the global dynamic demand transmitted into the tower system.

6.1.3 Effect on Base Shear

The response of the tower base shear is less uniform. Base shear is reduced for W1, W2, and W3, is essentially unchanged for W4 and W5. Therefore, the damper retrofit cannot be described as uniformly beneficial for all internal force components.

Although the dampers reduce longitudinal displacement and acceleration, they also modify the dynamic force redistribution within the bridge. Base shear depends on the coupled interaction between the deck, cables, towers, support conditions, and damper forces, and is not governed only by the peak longitudinal displacement.

6.1.4 Effect on Tower Shear

A similar observation applies to the transverse shear in the tower beam, where the peak values essentially remanin constant across ground motions.

6.1.5 Response of the E Record

The E record provides an additional indication of this complexity. Unlike the W1–W5 records, the E case shows increases in peak longitudinal displacement, longitudinal acceleration, overturning moment, and base shear after the dampers are added. The percentage increases in the E case should not be interpreted without considering the much smaller absolute demand level. The E record indicates that the dampers can slightly amplify some response quantities for lower-demand records or for records with different frequency content, even though the demands remain comparatively small.

6.2 Equivalent Linear Viscous Damper

The comparison in **Table 5.2** shows that both damper alternatives reduce the main longitudinal response of the bridge relative to the nonretrofitted model. The linear damper ($\alpha = 1.00$) generally produces smaller roller-support displacements and accelerations than the nonlinear damper ($\alpha = 0.40$), especially for W1–W4. This indicates that, for the selected properties, the linear alternative provides stronger control of the global longitudinal motion.

However, this trend does not extend uniformly to the internal force demands. The tower overturning moment and base shear show a more record-dependent behavior. In particular, W5 is a critical case: the nonlinear damper reduces the tower overturning moment, whereas the linear damper increases it above the nonretrofitted value. Similarly, the base shear remains unfavorable for W5 under both damper alternatives, even though the longitudinal displacement and acceleration are reduced.

The tower-beam shear also confirms that neither damper law is uniformly superior. For W1–W3, the nonlinear and linear alternatives produce similar peak shear values, while W4 favors the linear damper and W5 favors the nonlinear damper. Therefore, the velocity exponent should not be selected only from displacement or acceleration reduction. The results indicate that the final damper design should be based on both global response quantities and local force demands, supported by a parametric study of the damper coefficient, velocity exponent, and damper layout.

6.3 Bounded Analysis of the Damper Coefficient

The results of the bounded analysis can be found at **Fig. 5.33–Fig. 5.37**.

6.3.1 Reduction of Longitudinal Displacement and Acceleration

The roller-support longitudinal displacement, shown in **Fig. 5.33**, exhibits a consistent reduction as C increases. Relative to the base design, the upper-bound value of C reduces the displacement response for all five records, with reductions ranging from approximately 9.4% to 18.4%.

A similar trend is observed for the longitudinal acceleration at the roller support, shown in **Fig. 5.34**. The upper-bound value of C reduces the acceleration response for all records relative to the base design, with reductions ranging from approximately 6.4% to 28.0%. This indicates that, within the range considered, increasing C does not merely reduce displacement by transferring the demand into larger acceleration response at this location. Instead, the response suggests that the additional damping is effective in reducing both longitudinal displacement and longitudinal acceleration at the roller support.

6.3.2 Effect on Tower Overturning Moment

The tower overturning moment, shown in **Fig. 5.35**, also decreases as C increases. The upper-bound value reduces the tower overturning moment for all records relative to the base design, with reductions ranging from approximately 0.1% to 13.8%. The effect is therefore less pronounced than for the roller displacement, but the trend remains favorable. This is consistent with the results reported by Zhu et al. [20], where fluid viscous dampers produced strong reductions in displacement and tower bending moment in a long-span cable-stayed bridge.

6.3.3 Effect on Base Shear

The tower base shear, shown in **Fig. 5.36**, does not follow the same trend. Relative to the base design, the upper-bound value of C produces only a negligible change in the mean response and the effect is record-dependent. This behavior is also consistent with the trends reported in previous studies. Zhu et al. [20] found that the use of nonlinear fluid viscous dampers produced large reductions in deck displacement, tower displacement, and tower base moment, while the tower base shear reduction was much smaller. Liu et al. [21] also treated pylon base shear as an independent objective in the optimization of fluid viscous dampers for cable-stayed bridges, rather than assuming that it would automatically decrease together with the displacement response. The present bounded analysis shows the same type of trade-off: increasing C improves the displacement-controlled response quantities, but the tower base shear remains much less robust and may increase for some ground motions.

6.3.4 Effect on Tower Shear

The maximum tower-beam shear, shown in **Fig. 5.37**, is nearly insensitive to C for records W1, W2, and W3. For W4, the upper-bound value of C produces a significant reduction, from 40.42×10^3 kN in the base design to 20.09×10^3 kN. For W5, however, the upper-bound value increases the response from 20.48×10^3 kN to 23.22×10^3 kN. This record-to-record variability agrees with experimental observations reported by Guo et al. [26], where the effectiveness of viscous dampers in long-span cable-stayed bridges was shown to depend strongly on the characteristics of the ground motion and on spatial excitation effects.

Overall, the base-design value of C provides a balanced choice within the bounded range considered. The upper-bound value gives the most consistent improvement in roller displacement, longitudinal acceleration, and tower overturning moment, but it does not provide a uniformly better tower base shear response. The lower-bound value reduces tower base shear for some cases but at the cost of larger displacement, acceleration, and overturning moment demands. Therefore, the results should not be interpreted as a lack of effectiveness of the retrofit. Rather, they show the expected multi-objective nature of the design: the damper coefficient controls deck motion effectively, while tower base shear is governed by the force path between the deck, dampers, tower, and foundation. This interpretation is also consistent with the passive-control results of Soneji and Jangid [27], where stronger deck–tower restraint can reduce displacement demands but may increase force demands transmitted to the tower.

The base design is therefore reasonable if the primary retrofit objective is to reduce longitudinal displacement and tower overturning demand while avoiding excessive sensitivity to the damper coefficient. If tower base shear is a governing design criterion, however, it should be retained as an explicit performance objective rather than treated as a secondary consequence of displacement reduction.

7 Conclusions

Overall, the nonlinear response-history analyses show that the proposed longitudinal damper configuration is effective in reducing the main longitudinal response quantities for the W-series records of extreme events. The strongest and most consistent improvements are observed in the roller-support displacement, roller-support acceleration, and tower overturning moment. However, the base shear and tower-beam shear responses show a more complex behavior, including cases with negligible change or increased demand. This distinction is important because it shows that the effectiveness of fluid viscous dampers cannot be evaluated only from displacement reduction.

The bounded analysis of the damper coefficient showed that increasing C generally amplifies the beneficial effects observed in the longitudinal response quantities. Larger values of C produced additional reductions in roller-support displacement, roller-support acceleration, and tower overturning moment. However, the same trend was not observed for the tower base shear or the tower-beam shear. These force quantities remained more record-dependent and, in some cases, increased as the damper coefficient was increased. The equivalent linear viscous damper, defined to dissipate the same energy per cycle as the base nonlinear damper, also improved the main longitudinal response quantities, but did not provide a clear advantage in the shear demands. This indicates that the longitudinal dampers are effective in controlling deck motion and overturning demand, while the tower shear response is governed by a more complex redistribution of forces within the deck–damper–tower system. The possible incorporation of transverse supplemental damping could therefore be investigated in future work as a means of directly targeting the shear demands of the tower beams that were not reduced by the longitudinal damper configuration.

These results also demonstrate the value of performing full nonlinear response-history analysis for damper-retrofit studies. A simpler displacement-based assessment would suggest that the retrofit is clearly effective. The nonlinear analyses provide a richer view of the coupled bridge mechanics, showing that the dampers reduce the global longitudinal motion while also modifying internal force paths.

For these reasons, the studied configurations should be interpreted as a preliminary retrofit study rather than an optimized design. A more extensive bounding study should be performed by varying the damper coefficient, velocity exponent, and primairly number or distribution of dampers. Such a study would help determine whether a stronger or differently distributed damper configuration can preserve the observed reductions in longitudinal displacement and overturning moment while avoiding undesirable increases in base shear and transverse tower-beam shear.

8 References

[1] D. Konstantinidis, "Lectures for cee223: Earthquake protective systems." Course lectures, University of California, Berkeley, 2026. Spring 2025 semester SEMM MS Program.

[2] G. Chen, D. Yan, W. Wang, M. Zheng, L. Ge, and F. Liu, "Assessment of the Bill Emerson Memorial Cable-Stayed Bridge Based on Seismic Instrumentation Data," Final Report OR08-003, University Transportation Center at the University of Missouri-Rolla, Rolla, Missouri, Sept. 2007. Prepared for Missouri Department of Transportation, Organizational Results. Contract or Grant No. RI05-023.

[3] J. M. Caicedo, S. J. Dyke, S. J. Moon, L. A. Bergman, G. Turan, and S. Hague, "Phase II Benchmark Control Problem for Seismic Response of Cable-Stayed Bridges," *Journal of Structural Control*, vol. 10, pp. 137–168, 2003.

[4] Y. X. Zhang, J. M. Caicedo, S. H. Sim, C. M. Chang, B. F. Spencer, Jr., and X. Guo, "Modal Identification of Bill Emerson Bridge," in *Proceedings of the 14th World Conference on Earthquake Engineering*, (Beijing, China), Oct. 2008. October 12–17, 2008.

[5] U.S. Geological Survey, "The New Madrid Seismic Zone." `https://www.usgs.gov/programs/earthquake-hazards/new-madrid-seismic-zone`, 2026. Earthquake Hazards Program. Accessed: 2026-05-04.

[6] Buckenmyer, Daniel and Dreama, Jennifer, "Photographs of the Bill Emerson Memorial Bridge." `https://www.facebook.com/groups/707233279324256`, n.d. Photos extracted from posts in the Facebook group *Mississippi River photos*. Accessed: 2026-05-04.

[7] S. S. Badie, M. K. Tadros, and A. F. Girgis, "Full-Depth, Precast-Concrete Bridge Deck Panel Systems," NCHRP Project 12-65 Final Report, National Cooperative Highway Research Program, Transportation Research Board, National Research Council, Washington, DC, Nov. 2006. Section A.2.4.6, Missouri Department of Transportation; Bill Emerson Memorial Bridge.

[8] S. M. Romero and G. J. Rix, "Ground Motion Amplification of Soils in the Upper Mississippi Embayment," Tech. Rep. GIT-CEE/GEO-01-1, Georgia Institute of Technology, School of Civil and Environmental Engineering, March 2005. Sponsored by National Science Foundation and Mid America Earthquake Center.

[9] Taylor Devices, Inc., "Fluid Viscous Dampers." Online, 2026. Accessed 2026-05-04.

[10] L. Zoccolini, "Fluid Viscous Dampers for Seismic Protection of Bridges," *Procedia Structural Integrity*, 2024.

[11] Taylor Devices, Inc., "Earthquake Protective Systems for Buildings and Bridges." Technical document, n.d. Accessed 2026-05-04.

[12] MIDAS Information Technology, "General Link." Online, 2026. Accessed 2026-04-28.

[13] MIDAS Support, "Time History Load Cases." `https://support.midasuser.com/hc/en-us/articles/18100039617945-Time-History-Load-Cases`, 2023. Accessed 2026-05-04.

[14] A. K. Chopra, *Dynamics of Structures: Theory and Applications to Earthquake Engineering*. Boston: Pearson Education, 4th, global edition ed., 2014.

[15] S. P. Timoshenko and J. N. Goodier, *Theory of Elasticity*. New York: McGraw–Hill, 3rd ed., 1970. Chapter on torsion of noncircular shafts; thin-rectangle limit $J \to \frac{1}{3}ab^3$.

[16] O. C. Zienkiewicz, R. L. Taylor, and S. Govindjee, *The Finite Element Method: Its Basis and Fundamentals*. Elsevier, 8 ed., Nov. 2024.

[17] S. Govindjee, "Lectures for ce 222: Finite element methods." Course lectures, University of California, Berkeley, 2025. Spring 2026 semester.

[18] I. Katili, "A new discrete kirchhoff–mindlin element based on mindlin–reissner plate theory and assumed shear strain fields–part ii: An extended dkq element for thick-plate bending analysis," *International Journal for Numerical Methods in Engineering*, vol. 36, no. 11, pp. 1885–1908, 1993.

[19] MIDAS Information Technology, *Analysis Guide*. MIDAS Information Technology, 2026. MIDAS Civil Online Manual. Accessed 2026-05-06.

[20] J. Zhu, W. Zhang, K. F. Zheng, and H. G. Li, "Seismic design of a long-span cable-stayed bridge with fluid viscous dampers," *Practice Periodical on Structural Design and Construction*, vol. 21, no. 1, p. 04015006, 2016.

[21] Q. Liu, Z. Liu, J. Zhao, Y. Lei, S. Zhu, and X. Wu, "Seismic optimization of fluid viscous dampers in cable-stayed bridges: A case study using surrogate models and nsga-ii," *Buildings*, vol. 15, no. 9, p. 1446, 2025.

[22] Y. Chen, L. Ma, T. Cao, R. Schneider, and C. Winters, "Shock control of bridges in china using taylor devices' fluid viscous devices," in *Proceedings of the 14th World Conference on Earthquake Engineering*, (Beijing, China), Oct. 2008.

[23] X. He, Y. Yang, X. Xiao, and Y. Deng, "Research on fluid viscous damper parameters of cable-stayed bridge in northwest china," *Shock and Vibration*, vol. 2017, pp. 1–9, 2017.

[24] S. S. Badie, M. K. Tadros, and A. F. Girgis, "Full-Depth, Precast-Concrete Bridge Deck Panel Systems," Final Report NCHRP Project 12-65, National Cooperative Highway Research Program, Transportation Research Board, National Research Council, Washington, DC, Nov. 2006. Prepared for the National Cooperative Highway Research Program.

[25] D. Konstantinidis, "Lectures for cee223: Earthquake protective systems." Course lectures, University of California, Berkeley, 2025. Spring 2026 semester SEMM MS Program.

[26] W. Guo, J. Li, and Z. Guan, "Shake table test on a long-span cable-stayed bridge with viscous dampers considering wave passage effects," *Journal of Bridge Engineering*, vol. 26, no. 2, p. 04020118, 2021.

[27] B. B. Soneji and R. S. Jangid, "Passive hybrid systems for earthquake protection of cable-stayed bridge," *Engineering Structures*, vol. 29, no. 1, pp. 57–70, 2007.

[28] MIDAS Information Technology Co., Ltd., "MIDAS CIVIL NX," 2026. Bridge and civil structure analysis software. Accessed 2026-05-02.

[29] Missouri Department of Transportation, "SE Bill Emerson Bridge Fun Facts." Online, 2026. Accessed 2026-05-02.

[30] American Association of State Highway and Transportation Officials, *AASHTO LRFD Bridge Design Specifications*. American Association of State Highway and Transportation Officials, Washington, DC, 10th ed., 2024. Pub. Code: LRFDBDS-10.

[31] U.S. Geological Survey, "USGS Earthquake Hazard Toolbox: Dynamic Hazard." Online, 2026. Accessed 2026-04-26.

[32] American Society of Civil Engineers, "ASCE 7 Hazard Tool." Online, 2026. Accessed 2026-04-26.

[33] U.S. Geological Survey, "USGS Earthquake Hazard Toolbox: Disaggregation." Online, 2026. Accessed 2026-04-26.

[34] Pacific Earthquake Engineering Research Center, "PEER Ground Motion Database." Online, 2026. Accessed 2026-05-01.

[35] Wikipedia contributors, "Gamma function." https://en.wikipedia.org/wiki/Gamma_function, 2026. Accessed: 2026-05-06.

[36] MIDAS Information Technology, "General Link Properties." Online, 2026. Accessed 2026-04-28.

[37] N. M. Newmark, "A method of computation for structural dynamics," *Journal of the Engineering Mechanics Division*, vol. 85, no. 3, pp. 67–94, 1959.

[38] MOOSE Framework, "NewmarkBeta." https://mooseframework.inl.gov/source/timeintegrators/NewmarkBeta.html, 2024. Accessed 2026-05-04.

[39] DIANA FEA, "Newmark Time Integration." https://manuals.dianafea.com/d100/Theory/node165.html, 2015. DIANA 10.0 User's Manual, Theory Manual. Accessed 2026-05-06.

A APPENDIX A: Bill Emerson Finite Element Model in MIDAS Civil

The purpose of this appendix is to document the finite element model of the Bill Emerson Memorial Bridge implemented in MIDAS Civil[28]. The geometric, material, and dynamic properties of the bridge were assembled from the available reference studies[2, 3, 4]. The information extracted from these sources includes:

- Material properties for the concrete and steel components, as discussed in Section A.2.
- Section properties and element idealizations, as discussed in Section A.3.
- Stay-cable areas, lengths, and initial tensions.
- Support conditions and measured modal properties used for calibration of the numerical model.

The resulting finite element model and global reference frame are shown in **Fig. A.1**.

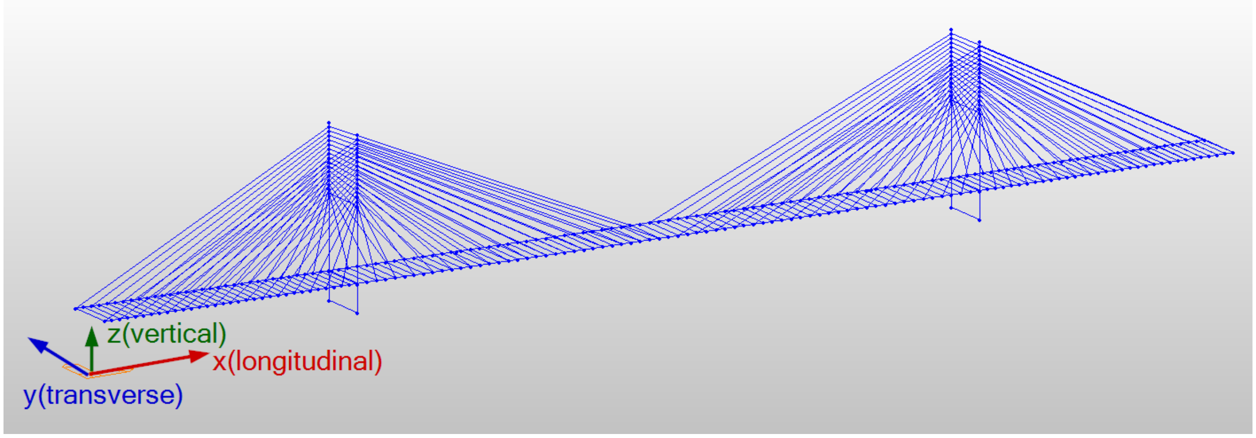

Figure A.1: General view of the finite element model and adopted global reference frame.

A.1 General Description

The numerical model represents the cable-stayed portion of the Bill Emerson Memorial Bridge. The main structural components included in the model are the concrete towers, longitudinal steel girders, transverse floor beams, concrete deck slab, stay cables, and support restraints. The deck system was represented through a combination of frame and plate elements, while the stay cables were modeled using axial cable elements with prescribed initial tensions.

The model was developed for global dynamic analysis rather than for local stress recovery. Therefore, the primary objective of the idealization was to reproduce the global stiffness, mass distribution, cable-force state, and modal characteristics of the bridge with sufficient accuracy for the seismic-response studies performed in this project. Particular attention was given to the adopted permanent weight, cable initial tensions, boundary conditions, and modal-frequency agreement, since these quantities directly affect the dynamic response of long-span cable-supported bridges.

A.2 Material Properties

The material properties adopted in the model are summarized in **Table A.1**. All materials were idealized as isotropic and linear elastic. The elastic moduli and Poisson's ratios were selected to remain consistent with the values reported in the reference models[2, 3, 4].

The adopted weight densities were adjusted to account for permanent components that were not explicitly modeled, including barriers, railings, attachments, and other secondary deck components. The adjustment was made by calibrating the total permanent-load resultants of the model against the values reported by the Department of Transportation[29]. This adjustment is important because the bridge mass distribution directly affects the computed modal properties. In addition, the adopted permanent weight determines the gravity-load state from which the cable forces and initial-stress stiffness are obtained before the linear eigenvalue analysis discussed in **Section A.5**.

Component	E **[kN/m^2]**	ν	γ **[kN/m^3]**	**Damping ratio**
Concrete deck slab and lumped deck weight	2.482×10^7	0.20	40.0	0.05
Concrete towers	2.482×10^7	0.20	23.6	0.05
Stay cables	1.999×10^8	0.30	90.0	0.02
Steel girders and floor beams	1.999×10^8	0.30	90.0	0.02

Table A.1: Isotropic linear-elastic material properties adopted in the numerical model.

A.3 Section Properties and Element Formulation

The section properties and element idealizations adopted in the numerical model are summarized in **Table A.2** and **Table A.3**. Only the section types assigned in the model are listed. Consistent with the reported as-built geometry[2, 3, 4], the tower members were modeled using box, solid rectangular, and tapered box frame sections. The deck system was modeled using longitudinal steel girder frame elements, transverse floor-beam frame elements, and plate elements for the concrete deck slab.

The tower section regions used in the model are shown in **Fig. A.4**. This figure is used to identify the locations of the assigned tower section regions listed in **Table A.2**.

Shear deformation was included in the frame sections, whereas the warping degree of freedom was not activated[4].

A.3.1 Section Summary

The assigned frame and plate section properties are summarized in **Table A.2**.

---

[4] This corresponds to the use of a Timoshenko beam formulation, in which the cross-section rotation is independent of the slope of the transverse displacement field and transverse shear deformation is included in addition to flexural deformation[15].

Component	**Model idealization**	**Section properties**
Top	Prismatic box frame section assigned to the upper tower region.	A = 12.998 m^2, A_{sy} = 8.800 m^2, A_{sz} = 7.113 m^2, I_{xx} = 32.183 m^4, I_{yy} = 69.489 m^4, I_{zz} = 14.702 m^4.
C–D	Tapered box frame section assigned to the tower region between C and D.	End i: H = 6.710 m, B = 3.660 m, t_w = 0.530 m, t_f = 0.910 m. End j: H = 6.710 m, B = 2.740 m, t_w = 0.530 m, t_f = 0.910 m.
D–E	Prismatic solid rectangular frame section assigned to the lower tower legs.	A = 24.559 m^2, A_{sy} = 20.466 m^2, A_{sz} = 20.466 m^2, I_{xx} = 72.254 m^4, I_{yy} = 92.144 m^4, I_{zz} = 27.415 m^4.
Transverse D–E	Prismatic solid rectangular frame section assigned to the transverse tower member at level D–E.	A = 24.592 m^2, A_{sy} = 20.493 m^2, A_{sz} = 20.493 m^2, I_{xx} = 77.615 m^4, I_{yy} = 79.029 m^4, I_{zz} = 32.136 m^4.
Steel girders	Longitudinal steel frame elements assigned to the deck girder lines.	A = 1.005 m^2, A_{sy} = 0.250 m^2, A_{sz} = 0.750 m^2, I_{xx} = 0.008 m^4, I_{yy} = 3.063 m^4, I_{zz} = 0.026 m^4.
Floor beams	Transverse steel I-section frame elements.	d = 1.000 m, b_{f1} = b_{f2} = 0.400 m, t_w = 0.050 m, t_{f1} = 0.050 m, t_{f2} = 0.052 m.
Deck slab	Four-node thin-plate elements without plate offset.	t = 0.320 m for both in-plane and out-of-plane behavior.
Stay cables	Axial cable elements.	Cable areas, lengths, and initial tensions are listed separately in **Table A.3**.

Table A.2: Section properties assigned in the numerical model. Here, A is the cross-sectional area, A_{sy} and A_{sz} are the effective shear areas in the local y and z directions, I_{xx} is the torsional constant used by the frame section, I_{yy} and I_{zz} are the second moments of area about the local y and z axes, H is the box-section depth, B is the box-section width, d is the I-section depth, b_f is a flange width, t_w is the web thickness, t_f is a flange thickness, and t is the plate thickness.

A.3.2 Deck Representation

The concrete deck was modeled using four-node thin-plate elements. The plate nodes were shared with the beam elements representing the longitudinal steel girders; therefore, displacement compatibility between the concrete deck and the steel girder lines was enforced directly at the common nodes[16, 17]. This idealization approximates the composite behavior of the concrete deck and steel framing while preserving the flexural and torsional flexibility of the deck system.

The transverse floor beams were included explicitly. The longitudinal spacing between cable-support locations along each edge girder is approximately 5.49 m, while the floor beams are placed at half of this spacing, giving an approximate longitudinal floor-beam separation of 2.74 m. The contractor report states that the length of each precast deck panel was selected so that each panel spans between two adjacent floor beams[24].

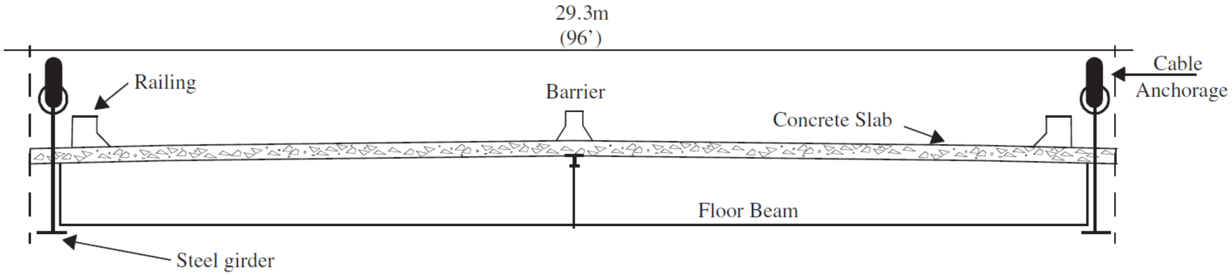

Figure A.2: Deck cross section of the Bill Emerson Memorial Bridge, adapted from Caicedo et al.[3].

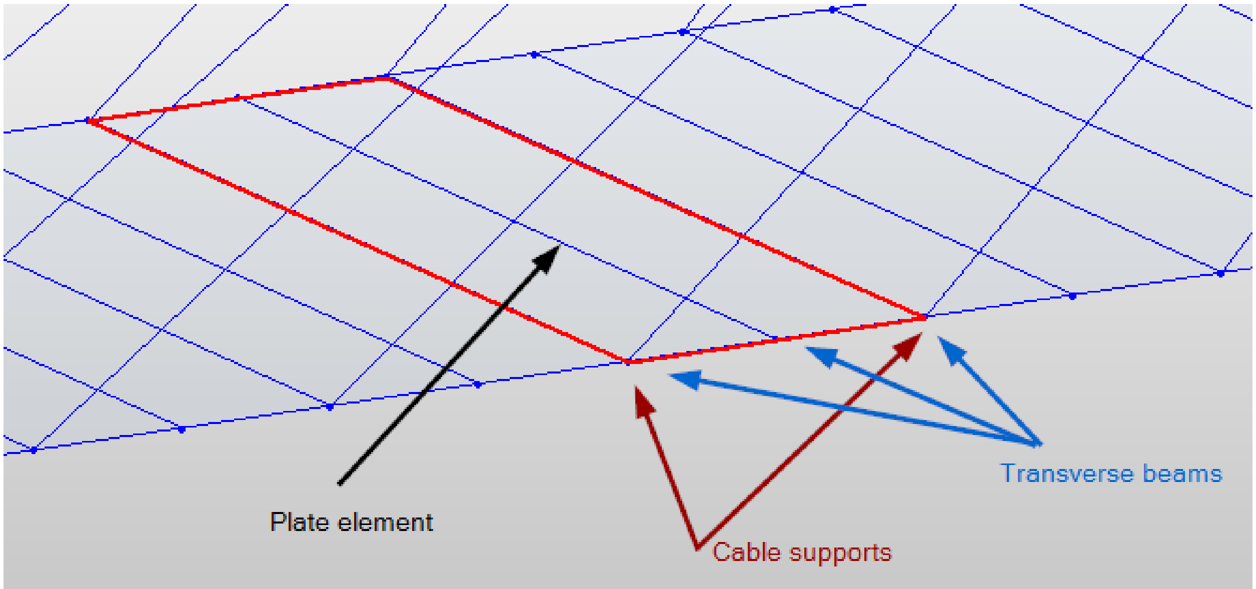

Figure A.3: Detail of the deck idealization between cable-support regions, including plate elements, longitudinal steel girders, and transverse floor beams.

A.3.3 Stay Cable Properties and Initial Tensions

The stay cables were modeled using axial cable elements. The reported cable areas, lengths, and initial tensions were adopted from the reference finite element model[2, 3]. The columns denoted *I* and *J* in **Table A.3** correspond to the two local ends of each cable element.

The values listed in **Table A.3** are the prescribed initial cable tensions. These forces are subsequently updated through the gravity-load procedure to account for force redistribution after the permanent loads are applied. Therefore, the modal analysis is performed about the gravity-loaded configuration, as discussed in **Section A.5**.

Cable No.	Diameter [m]	Area [m^2]	Initial tension *I* [kN]	Initial tension *J* [kN]	Length [m]
1	0.1014	0.00808	7837.90	7983.60	158.86
2	0.1014	0.00808	8233.26	8375.67	154.84
3	0.0976	0.00749	7742.66	7876.65	150.84
4	0.0926	0.00674	5514.69	5614.38	147.02
5	0.0905	0.00644	5409.74	5504.57	143.02
6	0.0884	0.00614	4920.66	5009.63	132.86
7	0.0840	0.00554	5337.23	5418.88	122.68
8	0.0840	0.00554	5058.98	5137.07	112.77
9	0.0817	0.00524	3649.84	3710.51	103.11
10	0.0769	0.00464	3851.38	3904.72	93.49
11	0.0769	0.00464	3672.04	3722.04	84.25
12	0.0756	0.00449	3118.39	3163.43	75.45
13	0.0717	0.00404	2459.85	2495.78	66.95
14	0.0662	0.00345	1829.71	1858.27	58.96
15	0.0632	0.00314	1189.74	1211.57	51.77
16	0.0602	0.00285	1209.04	1223.27	44.25
17	0.0602	0.00285	1110.97	1125.04	43.57
18	0.0632	0.00314	1361.75	1383.21	50.47
19	0.0662	0.00345	1783.06	1810.92	57.21
20	0.0676	0.00359	1965.90	1998.42	64.85
21	0.0744	0.00434	2927.96	2970.52	73.06
22	0.0756	0.00449	3395.19	3441.46	81.66
23	0.0769	0.00464	3935.02	3985.24	90.71
24	0.0805	0.00509	3973.45	4028.74	100.17
25	0.0840	0.00554	5252.55	5324.99	109.74
26	0.0840	0.00554	5228.18	5303.43	119.60
27	0.0894	0.00628	5094.98	5177.92	129.68
28	0.0916	0.00659	5121.93	5209.80	139.82
29	0.0926	0.00674	5543.83	5635.09	150.00
30	0.0966	0.00734	7709.35	7832.12	160.10
31	0.1015	0.00808	8558.47	8690.27	170.43
32	0.1015	0.00808	7482.38	7617.77	180.94

Table A.3: Reported cable areas, lengths, and initial tensions adopted in the numerical model.

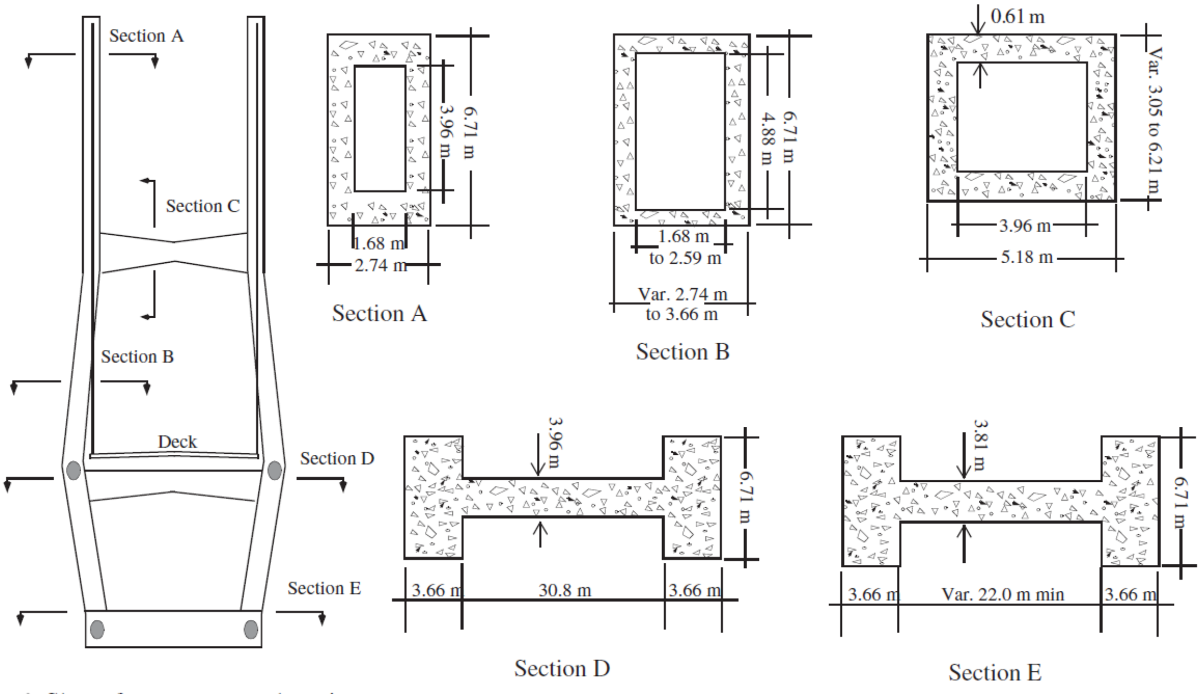

Figure A.4: Tower geometry used to define the frame section regions in the numerical model.

A.4 Boundary Conditions

Boundary conditions play a critical role in the dynamic response of flexible long-span structures. For the Bill Emerson Memorial Bridge, a boundary-condition sensitivity study was reported by Chen et al.[2], where different support idealizations were evaluated against the measured dynamic properties of the bridge.

In the present model, the Illinois approach span was not explicitly included. Therefore, the boundary conditions were selected to represent the support behavior of the cable-stayed portion of the bridge while approximately accounting for the restraint effect introduced by the omitted approach span. The selected configuration follows the boundary-condition idealization that provided the most suitable agreement with the modal response discussed in **Section A.5**.

The adopted boundary conditions are summarized as follows:

- The tower piers were modeled as fixed supports.
- The deck end support was restrained in the vertical and transverse directions.
- Longitudinal translation at the deck end support was left free to allow longitudinal expansion of the deck.

The adopted boundary-condition idealization is shown in **Fig. A.5**.

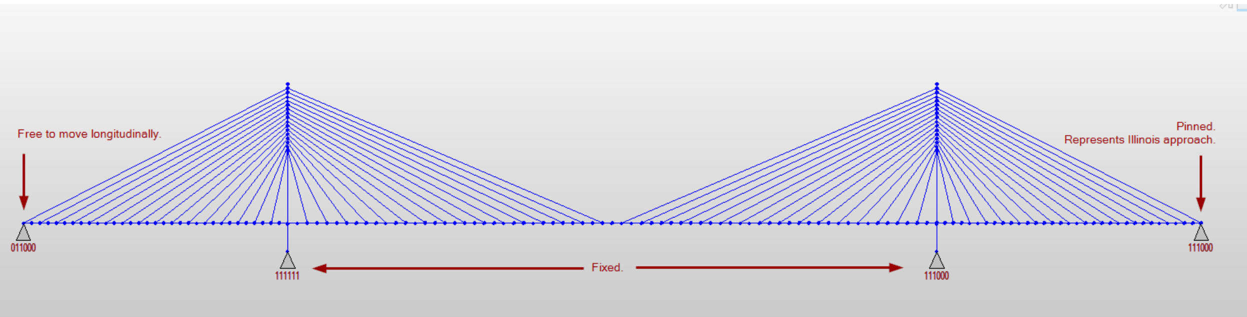

Figure A.5: Boundary-condition idealization adopted in the numerical model.

A.5 Model Calibration: Linear Eigenvalue Analysis

After defining the material properties, section properties, cable properties, and boundary conditions from the available public information[2, 3, 4], several modeling uncertainties remain. The most relevant uncertainties are:

- The exact dimensions of the steel girders and steel floor beams are not fully defined in the available reports. These properties were initially inferred from sketches such as **Fig. A.2**[3] and from available photographs of the bridge and deck construction[24], but need calibration.
- The exact permanent dead load to be included in the model is not completely specified. This quantity directly affects the total mass, mass distribution, cable-force state, and dynamic properties of the structure[14, 25].

Because of these uncertainties, the model was calibrated using the measured natural frequencies and mode shapes reported for the actual bridge[3]. Mode shapes and natural frequencies provide a compact description of the global mass and stiffness distribution of a structure and are therefore useful indicators of the reasonableness of the numerical idealization[14, 25].

It is important to note that the benchmark model used for comparison was an equivalent spine model, in which the bridge was represented with beam elements and the deck was connected to the cable anchorage points through rigid links. This modeling strategy is shown in **Fig. A.6**. In contrast, the present model includes an explicit deck idealization with plate elements, longitudinal girders, and transverse floor beams. For this reason, exact one-to-one agreement between individual local modes is not expected; the calibration is instead evaluated through the agreement of the principal global modes and their associated measured frequencies, which are made available in the instrumented bridge[2].

Table A.4 showcases the measured available natural frequency information along with the obtained in the FEM model. THe relative error is computed as:

$$\text{Error} = \frac{f_{\text{FE}} - f_{\text{measured}}}{f_{\text{measured}}} \times 100.$$

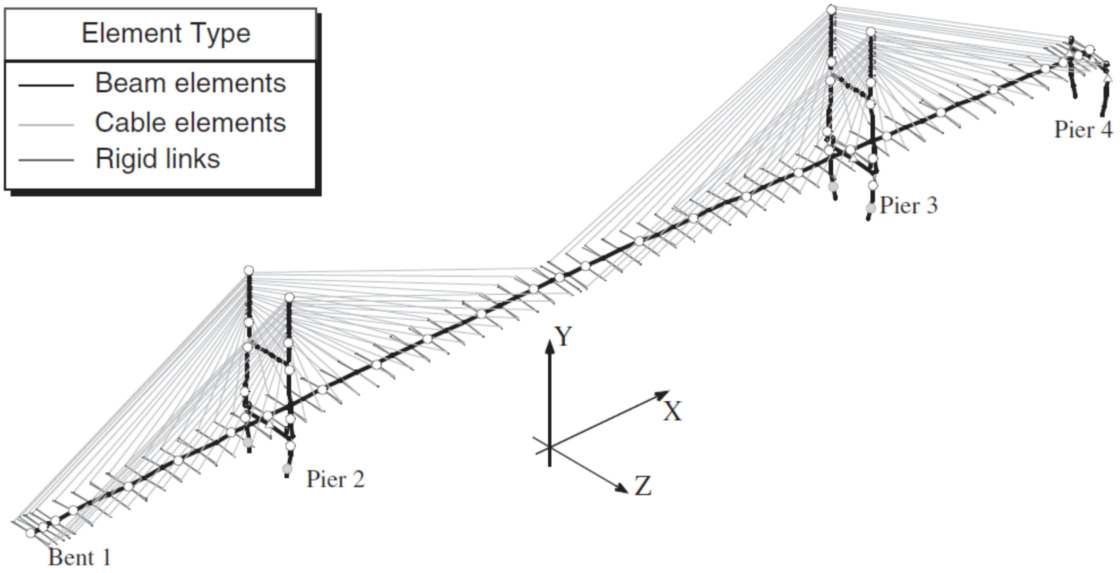

Figure A.6: Equivalent spine model used for dynamic eigenanalysis comparison, adapted from Caicedo et al.[3].

Measured mode ID	Matched FE mode ID	FE frequency [Hz]	Measured frequency [Hz]	Error [%]	Largest translational modal mass [%] (global direction)
1	1	0.290	0.338	-14.35	11.84 (Z)
2	2	0.408	0.438	-6.88	0.06 (Y)
3	3	0.491	0.500	-1.84	6.49 (Z)
4	4	0.575	0.588	-2.14	0.00 (-)
5	5	0.664	0.650	2.20	12.91 (Z)
6	6	0.735	0.713	3.04	18.17 (Y)
7	9	0.782	0.775	0.96	0.04 (Y)
8	10	0.848	0.825	2.74	21.14 (Z)
9	11	0.855	0.850	0.64	0.56 (Y)
10	12	1.177	1.075	9.47	0.29 (X)
11	14	1.410	1.338	5.37	62.20 (X)
12	18	1.709	1.725	-0.91	0.00 (-)
13	22	1.933	2.038	-5.13	0.18 (Y)
14	24	2.320	2.338	-0.77	0.00 (-)
15	28	3.291	3.263	0.86	2.90 (Y)
16	51	7.343	7.625	-3.69	0.79 (Y)
17	57	8.702	8.775	-0.83	0.00 (-)
18	64	10.939	10.850	0.82	0.67 (Y)
19	71	11.907	12.010	-0.86	0.00 (-)

Table A.4: Comparison between calculated and measured natural frequencies for the selected numerical model. The last column reports the largest translational modal participation percentage and the corresponding global direction.

Although the fundamental mode shows the largest relative discrepancy, with an error of 14.35%, this mode was not used as the sole indicator of the quality of the model calibration. Its largest translational modal participation occurs in the vertical Z direction, equal to 11.84%, and therefore it does not by itself govern the principal horizontal seismic response of the structure. For long-span bridges, the calibration should be evaluated from the broader modal response rather than from only the first natural frequency, which is consistent with the need for multimode dynamic characterization in bridge analysis[30].

The selected model therefore reflects a compromise between the available public geometric information, the inferred permanent-load distribution, the adopted boundary-condition idealization, and the measured modal properties of the bridge. The resulting agreement is considered adequate for the global seismic-response comparisons performed in this study, especially because the main objective is to evaluate the relative effect of adding fluid viscous dampers rather than to recover local member stresses with design-level accuracy.

A.5.1 Representative Mode Shapes

Representative computed mode shapes for the calibrated finite element model are shown in **Fig. A.7**–**Fig. A.12**. The plotted deformed shapes are shown with arbitrary scale factors for visualization; therefore, only the relative deformation pattern is meaningful. The sign of each mode shape is also arbitrary and has no physical significance by itself.

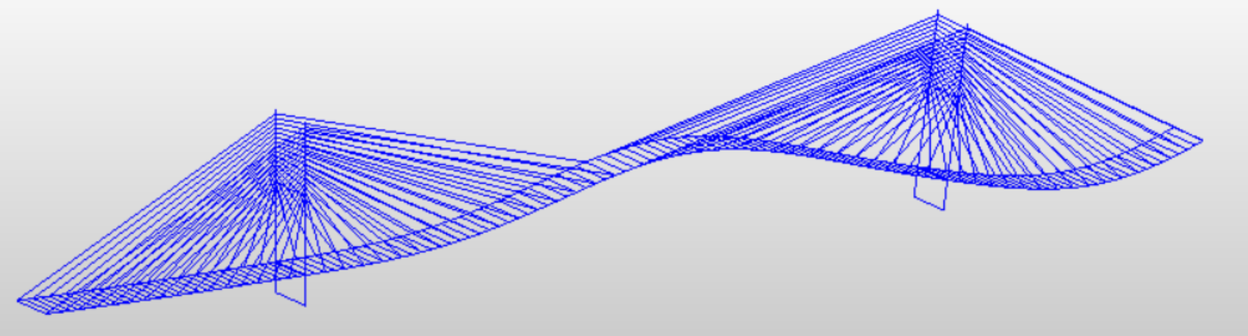

Figure A.7: Computed mode shape for FE mode 1, with natural frequency $f = 0.290$ Hz. The largest translational modal participation occurs in the global Z direction.

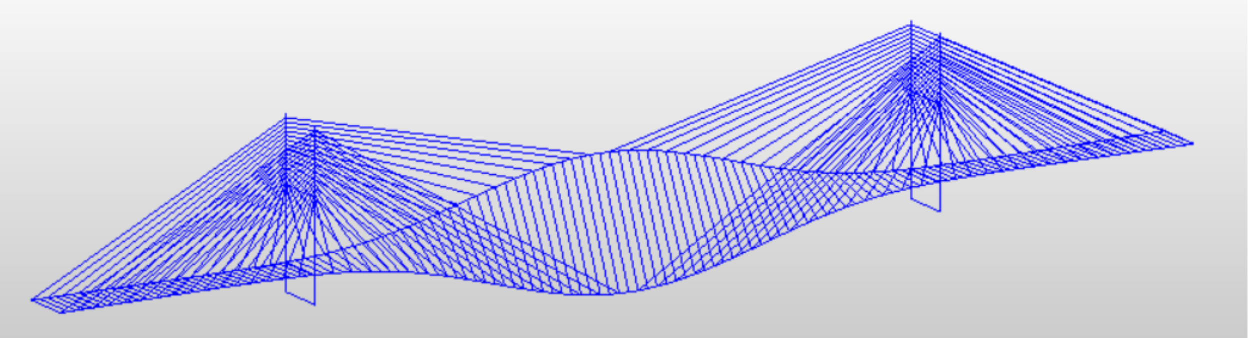

Figure A.8: Computed mode shape for FE mode 2, with natural frequency $f = 0.408$ Hz. This mode is included as part of the comparison with the measured dynamic properties of the bridge.

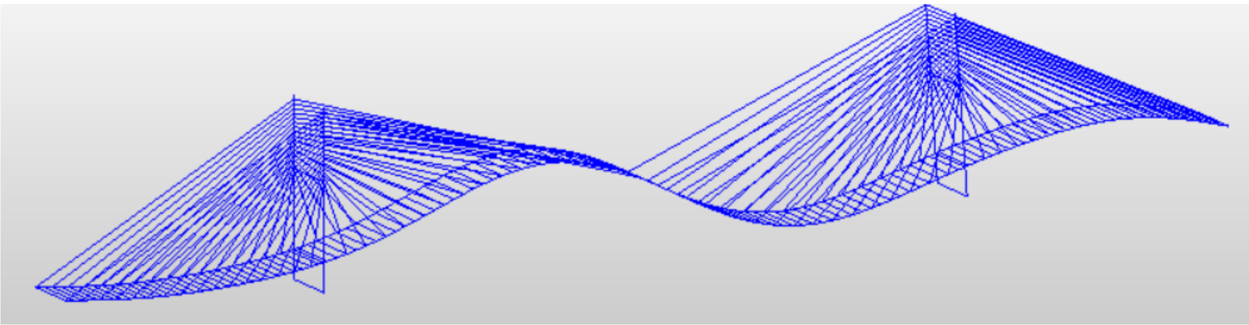

Figure A.9: Computed mode shape for FE mode 3, with natural frequency $f = 0.491$ Hz. The largest translational modal participation occurs in the global Z direction.

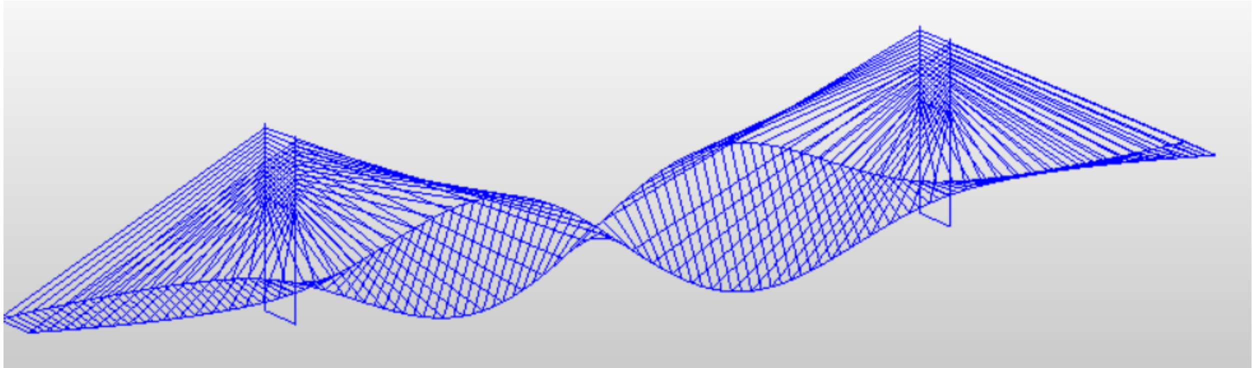

Figure A.10: Computed mode shape for FE mode 5, with natural frequency $f = 0.664$ Hz. This mode contributes to the vertical modal response of the calibrated bridge model.

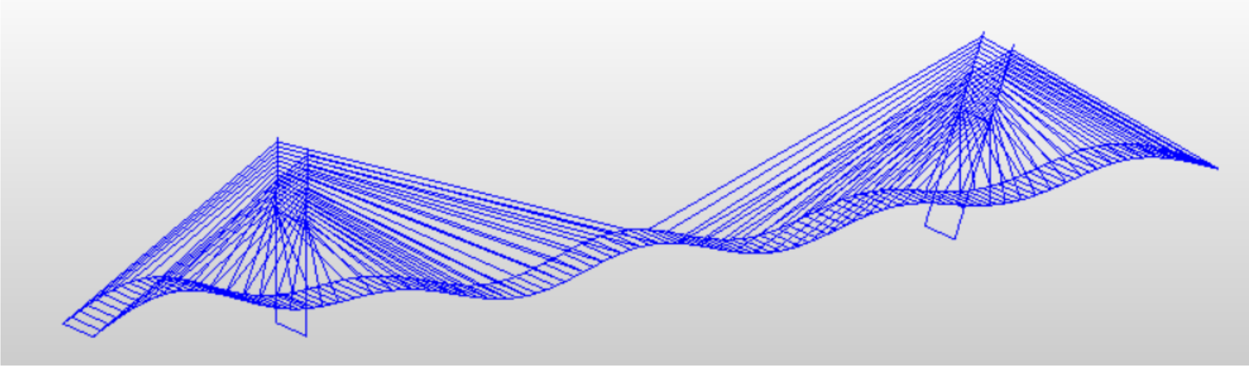

Figure A.11: Computed mode shape for FE mode 14, with natural frequency $f = 1.410$ Hz. This mode has the largest longitudinal translational modal participation among the matched modes listed in **Table A.4**.

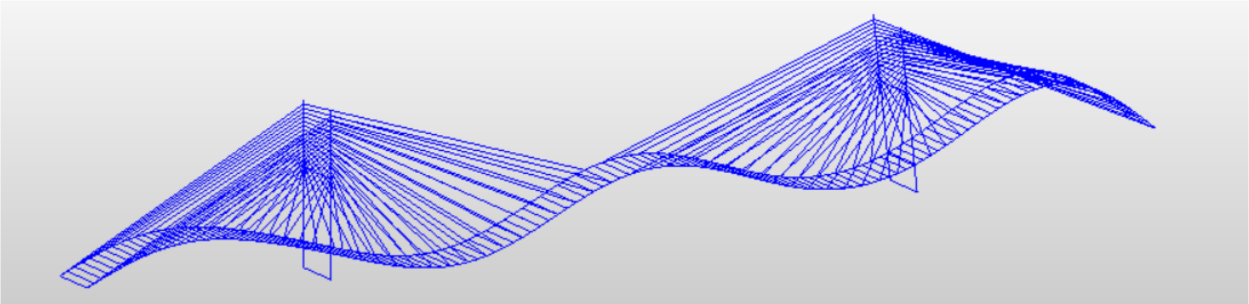

Figure A.12: Computed mode shape for FE mode 6, with natural frequency $f = 0.7343$ Hz. This higher-frequency mode is included to illustrate the range of matched modes used in the modal-calibration comparison.

Figure 5.2 1st mode shape (0.339Hz)

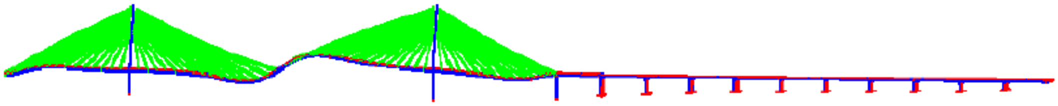

Figure 5.3 2nd mode shape (0.400Hz)

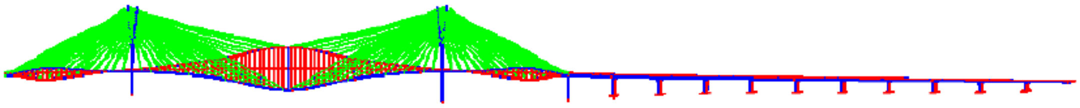

Figure 5.4 3rd mode shape (0.484Hz)

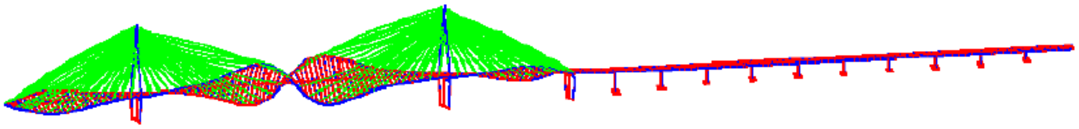

Figure 5.5 4th mode shape (0.573Hz)

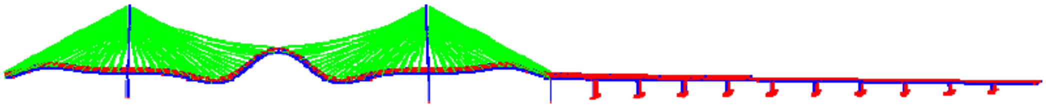

Figure 5.6 5th mode shape (0.602Hz)

Figure A.13: Available mode shapes from report[2]. Used for qualitative comparison

B APPENDIX B: Ground Motion Selection

The goal of this section is to present details regarding the selection of ground motions used in the nonlinear time history analysis of the Bill Emerson Bridge model in Midas Civil[28].

B.1 Site and Target Spectrum

The USGS Earthquake Hazard Toolbox [31] is used to generate hazard curves and a uniform hazard spectrum for a specified hazard level. This uniform hazard spectrum is then used as the target spectrum for selecting ground motions. The inputs required for the USGS Hazard Toolbox are the coordinate location of the site, site class or V_{S30} value, and the level seismic hazard being considered.

The exact coordinate location of the Bill Emerson Bridge, determined from the ASCE Hazard Tool [32], is (37.295189 N, -89.518536 W). The soil conditions for the site was determined to be Site Class D from a research report on the geology and soil conditions of the Upper Mississippi Embayment [8].

It was decided to select ground motions for two different levels of seismic hazard:

- A representative design earthquake with a 475 year return period (10% probability in 50 yrs)
- An extreme maximum considered earthquake (MCER) with a 2475 year return period (2% probability in 50 yrs)

The hazard curves and target spectra for both hazard levels, generated by the USGS Hazard Toolbox are shown below.

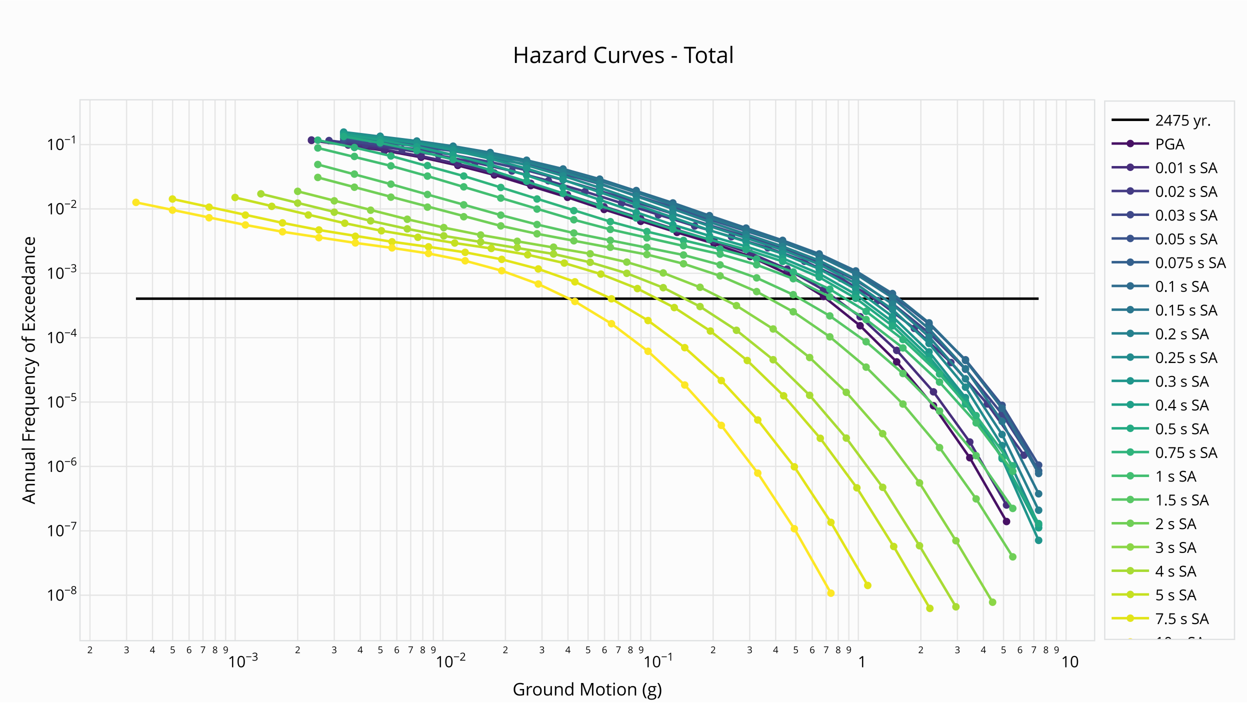

Figure B.1: Dynamic Hazard Curves Generated by USGS Earthqauke Hazard Toolbox

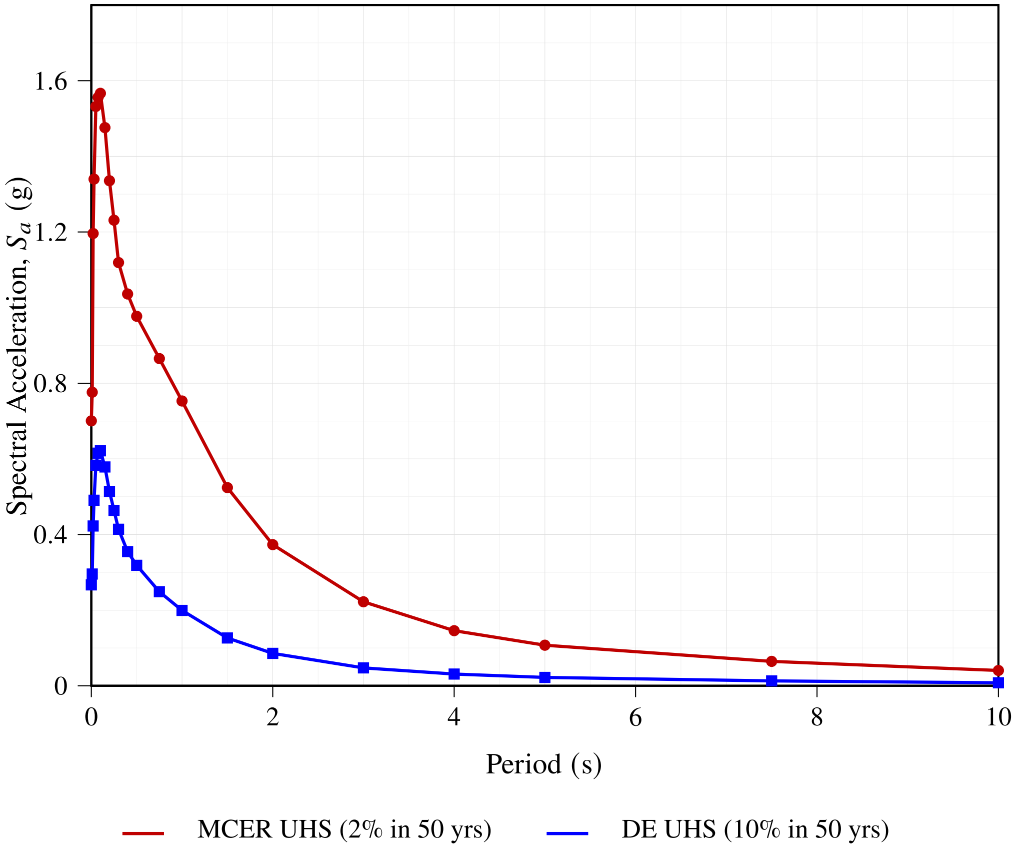

Figure B.2: Target Uniform Hazard Spectra (UHS) for the Design Earthquake (DE, 10% in 50 yrs) and Maximum Considered Earthquake (MCER, 2% in 50 yrs).

B.2 Hazard Disaggregation

A hazard deaggregation was performed using the USGS Earthquake Hazard Toolbox [33] for the specific site to determine the contribution of all potential earthquake magnitudes, distances, and sources. This information is used as the search criteria when selecting ground motions for each seismic hazard level.

AASHTO does not provide a specific period range of interest for scaling ground motions, so we assume the same scaling philosophy as ASCE-7, which is $0.2T_n - 2.0T_n$. However, upon further investigation of the mode shapes and modal participation factors, it was discovered that the fundamental mode of the bridge is not the dominant mode and higher modes actually govern the behavior of the bridge. For example, the first significant mode is the 14th mode, making up of approximately 62% of the total effective modal mass, with even higher modes contributing to the rest of the effective modal mass. See **Fig. B.3** for the sum of effective modal mass as a function of the mode number, for each translational direction.

Therefore, a broader period range of interest was used for scaling ground motions. This broader period range is from $T = 0.01\ s$ to around $T = 5\ s$, which includes the very short period range to account for much higher modes that govern the dynamic behavior of the bridge.

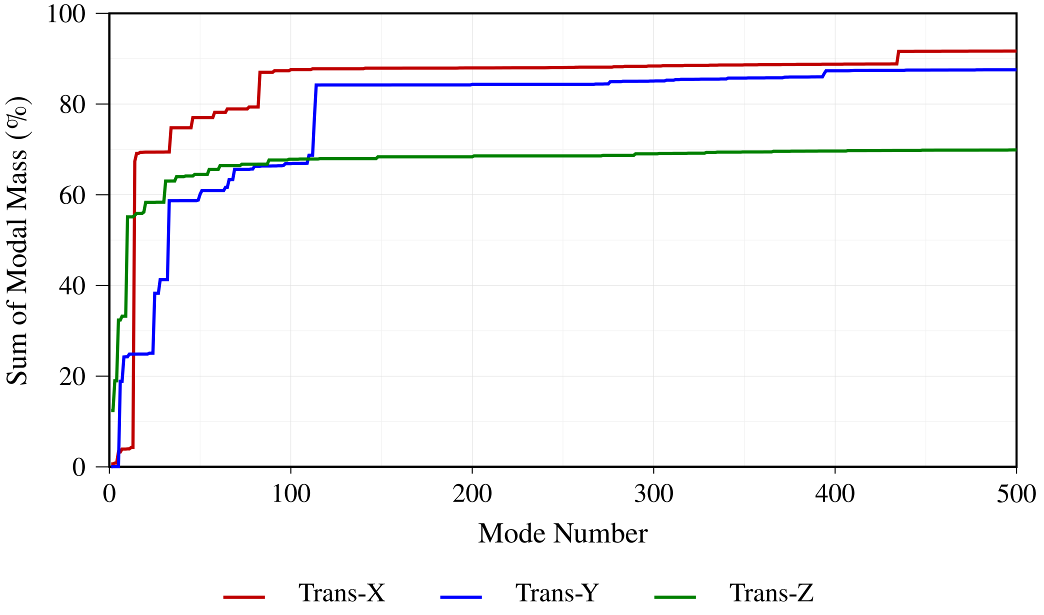

Figure B.3: Sum of modal mass ratio for translation in X, Y, and Z directions over 500 modes.

The results of the deaggregation plots for periods ranging from $T = 0.01\ s$ to $T = 5.0\ s$ is shown below:

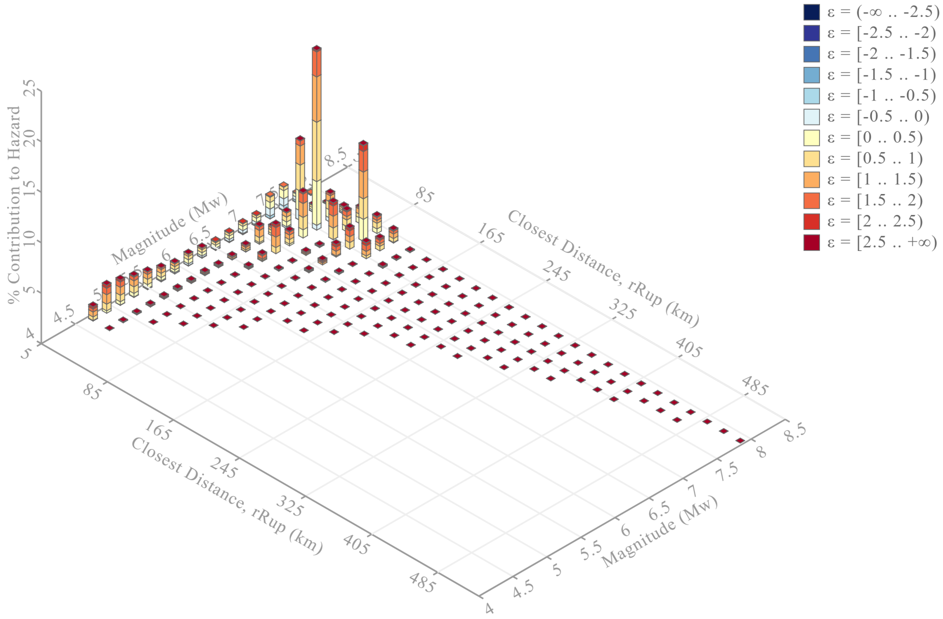

Figure B.4: Deaggregration: 2475 yr, $T = 0.01\ s$

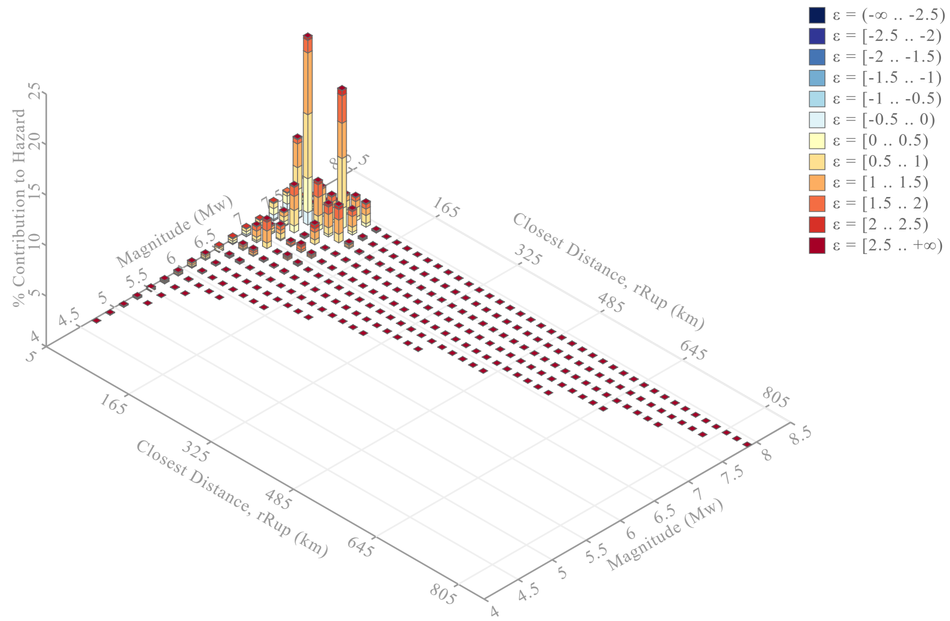

Figure B.5: Deaggregration: 2475 yr, T = 0.5 s

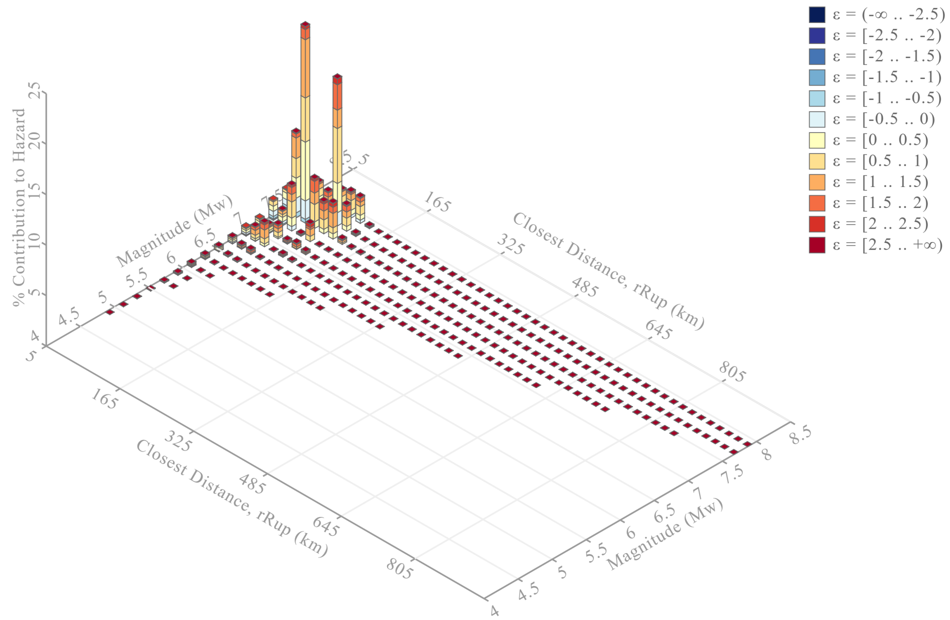

Figure B.6: Deaggregration: 2475 yr, T = 1.0 s

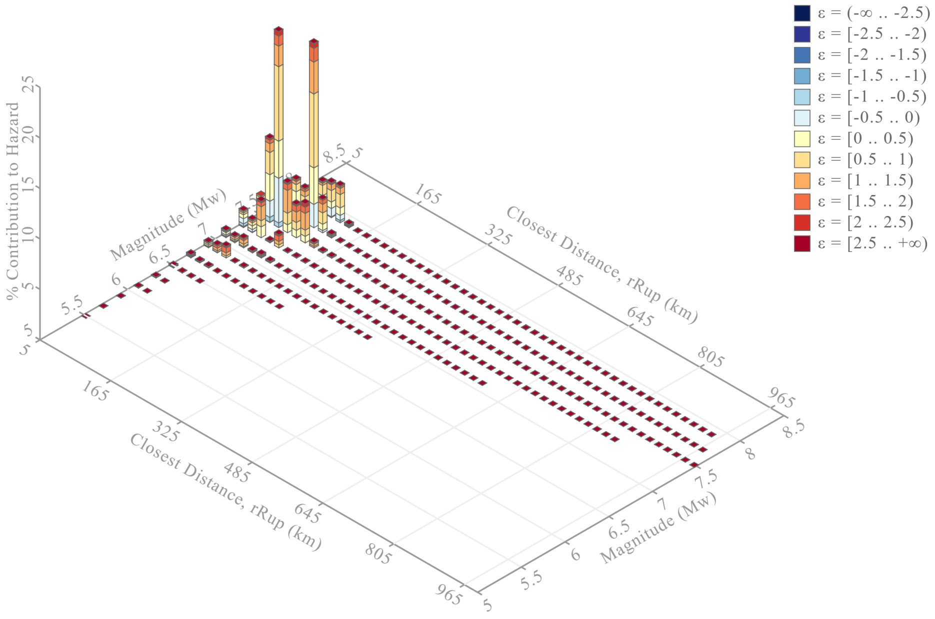

Figure B.7: Deaggregration: 2475 yr, T = 3.0 s

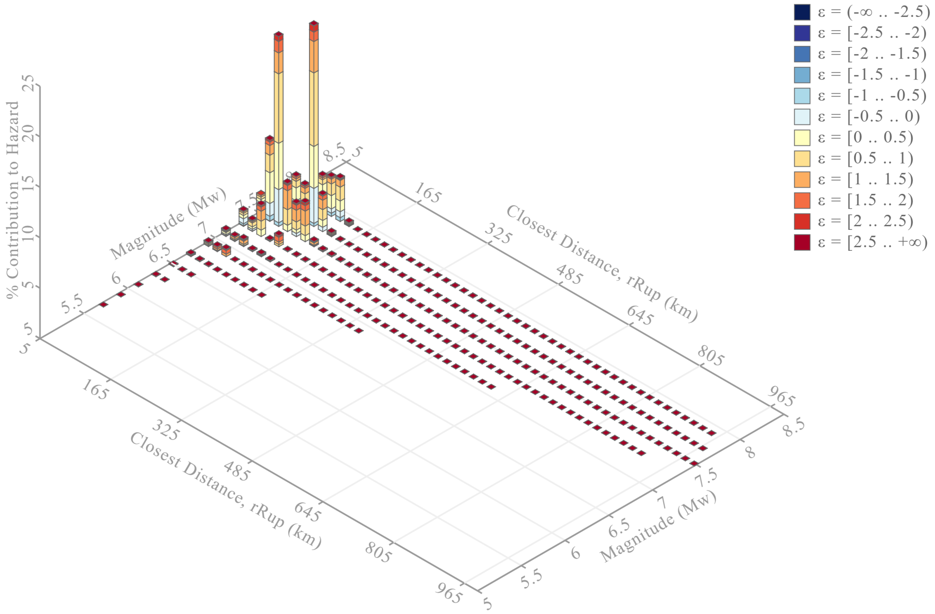

Figure B.8: Deaggregration: 2475 yr, T = 5.0 s

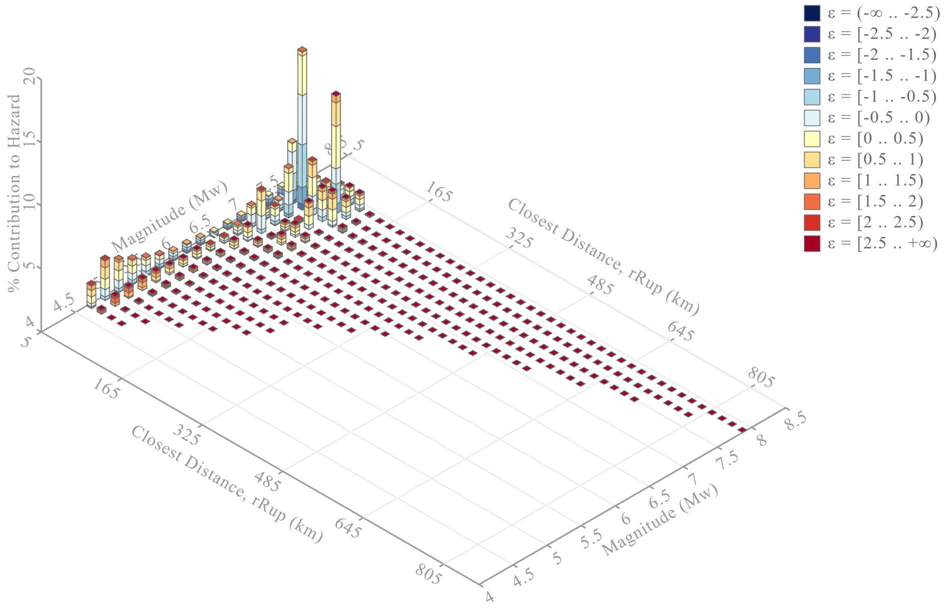

Figure B.9: Deaggregration: 475 yr, T = 0.01 s

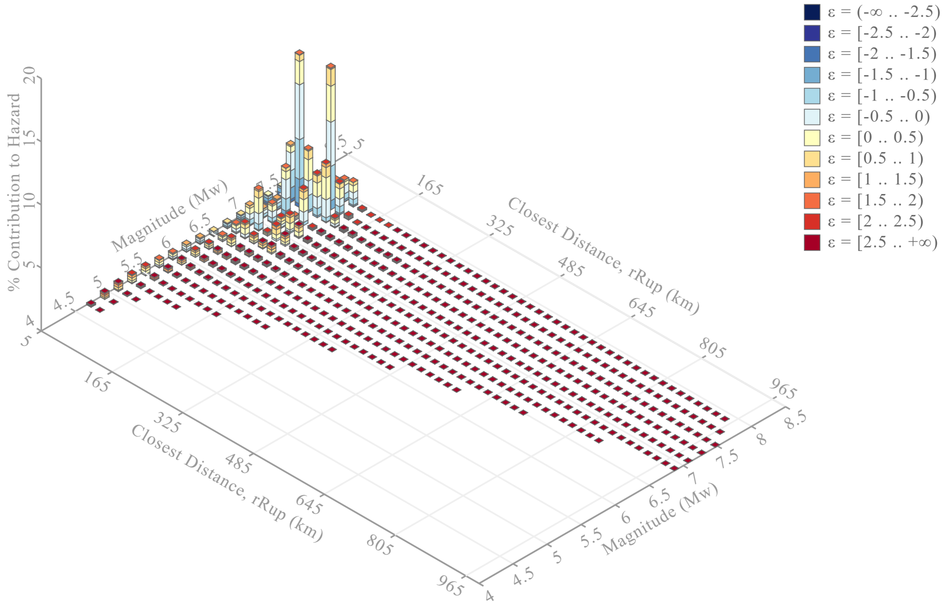

Figure B.10: Deaggregration: 475 yr, T = 0.5 s

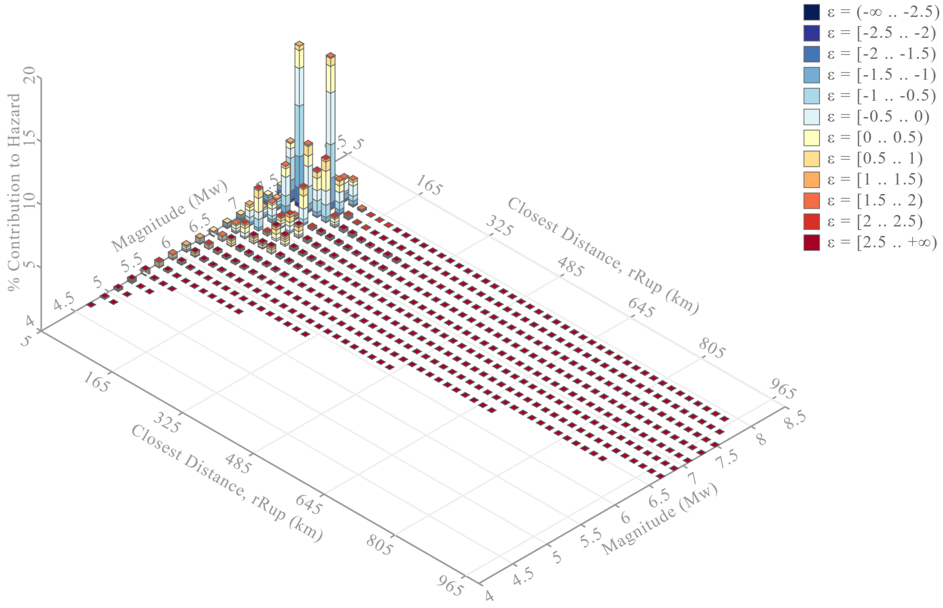

Figure B.11: Deaggregration: 475 yr, $T = 1.0\ s$

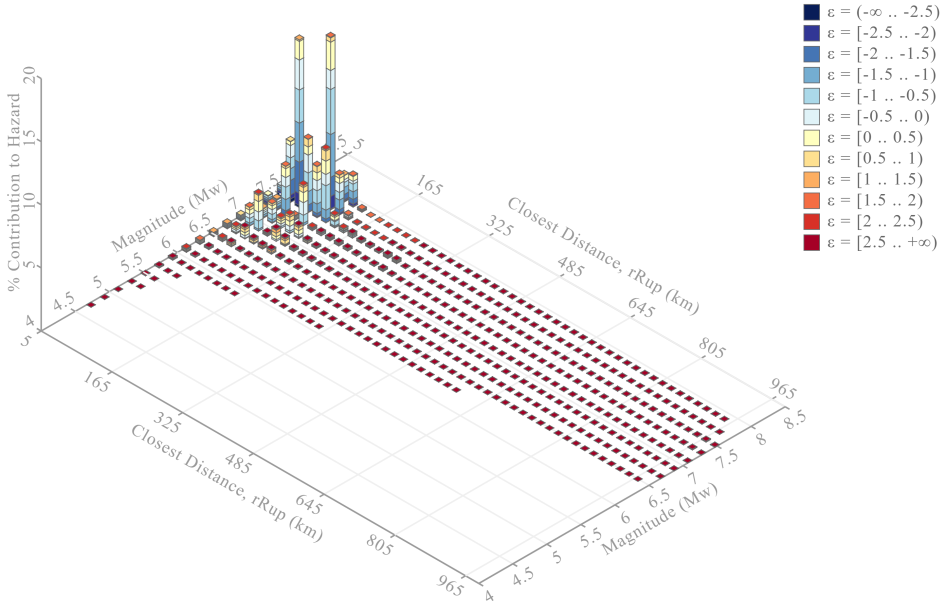

Figure B.12: Deaggregration: 475 yr, $T = 3.0\ s$

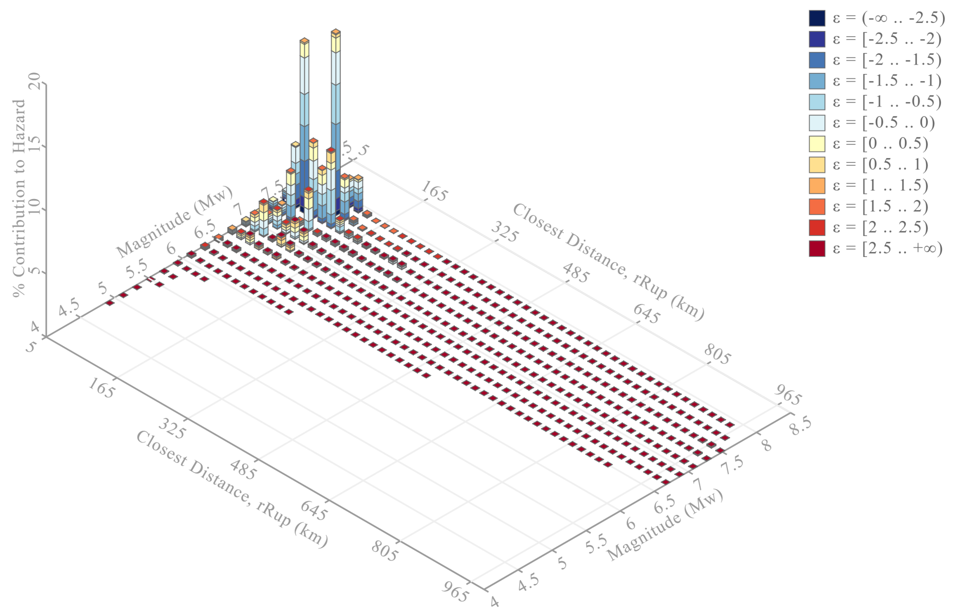

Figure B.13: Deaggregration: 475 yr, T = 5.0 s

B.3 Peer Database Ground Motion Selection

Ground motions are selected from the Peer Ground Motion Database [34]. The Bill Emerson Bridge is located near the New Madrid Seismic Zone, which is an intra-plate fault system characterized by strike-slip and some reverse faulting, so ground motions will be selected from the NGA East database.

Based on the deaggregation results shown above, the ideal search criteria/parameters used to find ground motions are:

- Fault type: strike-slip and/or reverse
- Magnitude: 7, 8
- R_{rup}: 30, 130 km
- $V_{S,30}$: 200, 400 m/s
- Spectral Ordinate: RotD100 (NGA West) or RotD50 (NGA East)
- Scaling method: Minimize MSE
- Period range/weight function period point: 0.01, 5 s
- Weight function weights: 1, 1

However, the NGA East database does not contain many large magnitude time history recordings (most recordings are less than 5.0 magnitude). Therefore, the NGA East database is used to select representative, unscaled design earthquake motions to represent realistic ground motions that would be expected to occur at the site, while, the NGA West database is used to select the extreme MCER ground motions of much higher intensity.

The selected ground motions for the representative design earthquake level hazard are:

Earthquake Name	**Station Name**	**Magnitude**	**Distance (R_{rup}, km)**	**V_{s30} (m/s)**
MtCarmel 2008-04-18a	Henderson Mound, MO	4.64	240.79	225.0
Whiting 2010-03-02	Martin, TN	3.40	65.65	300.0
Whiting 2010-03-02	Y8.S10	3.40	55.01	209.0
Mineral 2011-08-23	NP.2555	5.74	124.11	429.6
Sparks 2011-11-06	GS.OK009	5.68	60.07	321.0

Table B.1: Selected ground motions for design earthquake level hazard, from NGA-East Database

The selected ground motions for the MCER level hazard are:

Earthquake Name	**Station Name**	**Mag.**	**Dist. (R_{rup}, km)**	**V_{s30} (m/s)**	**Mechanism**	**Scale Factor**
Kocaeli, Turkey	Bursa Tofas	7.51	60.43	289.69	Strike Slip	4.9174
Chi-Chi, Taiwan	CHY004	7.62	47.32	271.30	Reverse Oblique	5.2239
Chi-Chi, Taiwan	CHY065	7.62	83.43	250.00	Reverse Oblique	5.6173
Manjil, Iran	Rudsar	7.37	64.47	242.05	Strike Slip	5.1450
Denali, Alaska	R109 (temp)	7.90	43.00	341.56	Strike Slip	7.1878

Table B.2: Selected ground motions for MCER level hazard, from NGA-West Database

C APPENDIX C: Fluid Viscous Dampers

Fluid viscous dampers are passive energy dissipation devices used to reduce structural response by converting mechanical energy into heat[1]. The device connects two structural points that experience relative motion. When relative motion occurs, the piston inside the damper forces a viscous fluid through internal orifices, producing a resisting force associated with the relative velocity between the two ends of the device.

An ideal fluid viscous damper is modeled as a velocity-dependent device. In this idealization, the resisting force depends on the relative velocity and does not depend directly on the relative displacement. Therefore, the device contributes supplemental energy dissipation with negligible elastic stiffness. This distinction is important because a purely viscous damper can reduce dynamic response without significantly changing the elastic vibration periods of the structure.

Let $u(t)$ denote the relative displacement between the two ends of the damper, defined positive along the local axis of the device. The corresponding relative velocity is:

$$\dot{u}(t) = \frac{du(t)}{dt}.$$

The damper force $P(t)$ is defined positive in the same direction as positive $u(t)$. The constitutive force law is:

$$P(t) = C_\alpha \left|\dot{u}(t)\right|^\alpha \operatorname{sgn}(\dot{u}(t)), \tag{C.1}$$

where C_α is the damper coefficient and α is the velocity exponent.

The sign function $\operatorname{sgn}(\cdot)$ is defined as:

$$\operatorname{sgn}(x) = \begin{cases} +1, & x > 0, \\ 0, & x = 0, \\ -1, & x < 0. \end{cases}$$

Thus, $\operatorname{sgn}(\dot{u})$ assigns the sign of the damper force according to the sign of the relative velocity. The magnitude of the force is controlled by $|\dot{u}|^\alpha$.

For $\alpha = 1$, **Eq. (C.1)** reduces to the linear viscous model:

$$P(t) = C_1 \dot{u}(t).$$

For $0 < \alpha < 1$, the damper is nonlinear. In this case, the force grows more slowly than the velocity at high velocities, while maintaining relatively large force levels at low velocities. This behavior is useful for supplemental damping applications because it can provide significant energy dissipation without causing damper forces to increase in direct proportion to peak velocity. For $\alpha > 1$, the force grows faster than the velocity at high velocities. This behavior is more representative of shock-transmission or lock-up devices than of conventional supplemental fluid viscous dampers.

Dimensional consistency of **Eq. (C.1)** requires:

$$[P] = [C_\alpha]\,[\dot{u}]^\alpha.$$

Therefore:

$$[C_\alpha] = F\left(LT^{-1}\right)^{-\alpha},$$

where F, L, and T denote the dimensions of force, length, and time, respectively.

C.1 Damper Coefficient from a Rated Force

Damper properties are commonly specified through a rated force P_r measured at a rated velocity v_r. These two quantities define the coefficient C_α once the velocity exponent α is selected. Taking magnitudes in **Eq. (C.1)** gives:

$$P_r = C_\alpha v_r^\alpha .$$

Hence:

$$C_\alpha = \frac{P_r}{v_r^\alpha} . \tag{C.2}$$

For a nonlinear damper with:

$$\alpha = \frac{1}{3}, \qquad P_r = 300 \text{ kips}, \qquad v_r = 27 \text{ in/s},$$

Eq. (C.2) gives:

$$C_{1/3} = \frac{300 \text{ kips}}{(27 \text{ in/s})^{1/3}} = 100 \, \frac{\text{kips}}{(\text{in/s})^{1/3}} .$$

At a relative velocity of 1 in/s, the corresponding force is:

$$P = 100\,(1)^{1/3} = 100 \text{ kips}.$$

Thus, reducing the velocity from 27 in/s to 1 in/s reduces the velocity by a factor of 27, while the force is reduced only by a factor of 3. This illustrates the effect of using a velocity exponent smaller than one.

C.2 Force–Displacement Loop under Harmonic Relative Motion

The force-displacement loop is useful because its enclosed area represents the energy dissipated by the damper during one cycle of motion. To obtain this loop in closed form, a prescribed harmonic relative displacement is used:

$$u(t) = u_0 \sin(\Omega t),$$

where u_0 is the displacement amplitude and Ω is the circular frequency of the imposed relative motion. Differentiating gives:

$$\dot{u}(t) = u_0 \Omega \cos(\Omega t).$$

Substituting this velocity into **Eq. (C.1)** gives:

$$P(t) = C_\alpha \left| u_0 \Omega \cos(\Omega t) \right|^\alpha \operatorname{sgn}(\cos(\Omega t)) .$$

The parametric curve $\big(u(t), P(t)\big)$ defines the force-displacement loop. Eliminating time gives an explicit normalized expression for its shape. Since:

$$\frac{u}{u_0} = \sin(\Omega t),$$

then:

$$|\cos(\Omega t)| = \Big(1 - \sin^2(\Omega t)\Big)^{1/2} = \left(1 - \frac{u^2}{u_0^2}\right)^{1/2} .$$

Therefore, the force magnitude satisfies:

$$|P| = C_\alpha \Omega^\alpha u_0^\alpha \left(1 - \frac{u^2}{u_0^2}\right)^{\alpha/2}.$$

Equivalently:

$$\left(\frac{|P|}{C_\alpha \Omega^\alpha u_0^\alpha}\right)^{2/\alpha} + \left(\frac{u}{u_0}\right)^2 = 1. \tag{C.3}$$

Equation **Eq. (C.3)** describes the normalized loop shape. For $\alpha = 1$, the curve is an ellipse. For $0 < \alpha < 1$, the curve becomes fuller and more rectangular because the force remains relatively large over a wider portion of the displacement cycle. This larger enclosed area corresponds to greater energy dissipation per cycle for the same displacement amplitude and frequency scale.

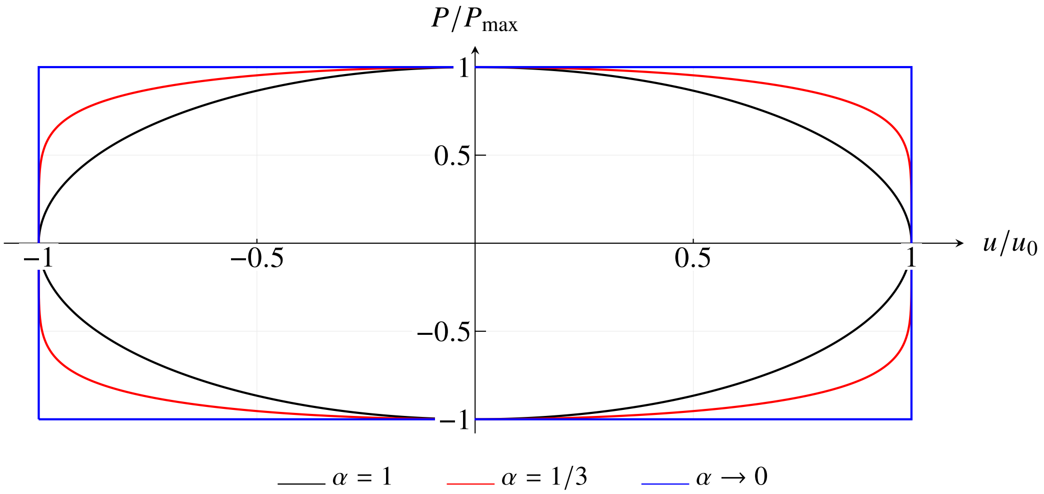

Figure C.1: Normalized force-displacement loops for fluid viscous dampers under harmonic relative motion.

C.3 Energy Dissipated per Cycle

The energy dissipated by a damper during one complete cycle equals the work done by the damper force over the closed force-displacement loop. The differential work associated with an incremental relative displacement du is $P\,du$. Therefore:

$$W_{D,\alpha} = \oint P\,du, \tag{C.4}$$

where $W_{D,\alpha}$ denotes the energy dissipated per cycle by a damper with velocity exponent α.

Since $du = \dot{u}\,dt$, **Eq. (C.4)** can be written in time form as:

$$W_{D,\alpha} = \int_0^{2\pi/\Omega} P(t)\dot{u}(t)\,dt. \tag{C.5}$$

Substitution of **Eq. (C.1)** into the integrand gives:

$$P(t)\dot{u}(t) = C_\alpha\,|\dot{u}(t)|^\alpha\,\mathrm{sgn}(\dot{u}(t))\,\dot{u}(t).$$

Since:

$$\mathrm{sgn}(\dot{u}(t))\,\dot{u}(t) = |\dot{u}(t)|,$$

the instantaneous dissipated power is:

$$P(t)\dot{u}(t) = C_\alpha \left|\dot{u}(t)\right|^{\alpha+1}.$$

For the harmonic relative motion previously introduced:

$$\dot{u}(t) = u_0\Omega\cos(\Omega t),$$

and therefore:

$$W_{D,\alpha} = \int_0^{2\pi/\Omega} C_\alpha \left|u_0\Omega\cos(\Omega t)\right|^{\alpha+1} dt.$$

The function $|\cos(\Omega t)|^{\alpha+1}$ gives equal contributions over the four quadrants of one cycle. Thus:

$$W_{D,\alpha} = 4C_\alpha\Omega^{\alpha+1}u_0^{\alpha+1}\int_0^{\pi/(2\Omega)} \cos^{\alpha+1}(\Omega t)\,dt.$$

Introducing the nondimensional angle:

$$\theta = \Omega t, \qquad d\theta = \Omega\,dt,$$

the energy becomes:

$$W_{D,\alpha} = 4C_\alpha\Omega^\alpha u_0^{\alpha+1}\int_0^{\pi/2} \cos^{\alpha+1}\theta\,d\theta. \tag{C.6}$$

The remaining integral is evaluated using the gamma function[35]. For $z > 0$, the gamma function is defined by:

$$\Gamma(z) = \int_0^\infty s^{z-1}e^{-s}\,ds.$$

The gamma function extends the factorial to non-integer arguments. For a positive integer n:

$$\Gamma(n) = (n-1)!.$$

It also satisfies:

$$\Gamma(z+1) = z\Gamma(z), \qquad \Gamma\left(\frac{1}{2}\right) = \sqrt{\pi}.$$

The standard integral needed in **Eq. (C.6)** is:

$$\int_0^{\pi/2} \cos^n\theta\,d\theta = \frac{\sqrt{\pi}}{2}\frac{\Gamma\left(\frac{n+1}{2}\right)}{\Gamma\left(\frac{n}{2}+1\right)}.$$

Taking $n = \alpha + 1$ gives:

$$\int_0^{\pi/2} \cos^{\alpha+1}\theta\,d\theta = \frac{\sqrt{\pi}}{2}\frac{\Gamma\left(\frac{\alpha+2}{2}\right)}{\Gamma\left(\frac{\alpha+3}{2}\right)}.$$

Substitution into **Eq. (C.6)** gives:

$$W_{D,\alpha} = 2\sqrt{\pi}\,C_\alpha\Omega^\alpha u_0^{\alpha+1}\frac{\Gamma\left(\frac{\alpha+2}{2}\right)}{\Gamma\left(\frac{\alpha+3}{2}\right)}. \tag{C.7}$$

For the linear case $\alpha = 1$, **Eq. (C.7)** gives:

$$W_{D,1} = 2\sqrt{\pi}\, C_1 \Omega u_0^2 \frac{\Gamma(3/2)}{\Gamma(2)}.$$

Using:

$$\Gamma\left(\frac{3}{2}\right) = \frac{1}{2}\Gamma\left(\frac{1}{2}\right) = \frac{\sqrt{\pi}}{2}, \qquad \Gamma(2) = 1,$$

it follows that:

$$W_{D,1} = \pi C_1 \Omega u_0^2.$$

This result is the area of the elliptical force-displacement loop of a linear viscous damper.

C.4 Equivalent Linear Viscous Coefficient

A nonlinear damper does not have a constant linear viscous coefficient. However, for a specified harmonic displacement amplitude u_0 and circular frequency Ω, an equivalent linear viscous coefficient can be defined by matching the energy dissipated per cycle.

Let $C_{1,\mathrm{eq}}$ denote the coefficient of a linear viscous damper that dissipates the same energy as the nonlinear damper under the same harmonic relative motion. The energy dissipated by this equivalent linear damper is:

$$W_{D,1,\mathrm{eq}} = \pi C_{1,\mathrm{eq}} \Omega u_0^2.$$

Equating this expression to **Eq. (C.7)** gives:

$$\pi C_{1,\mathrm{eq}} \Omega u_0^2 = 2\sqrt{\pi}\, C_\alpha \Omega^\alpha u_0^{\alpha+1} \frac{\Gamma\left(\frac{\alpha+2}{2}\right)}{\Gamma\left(\frac{\alpha+3}{2}\right)}.$$

Solving for $C_{1,\mathrm{eq}}$:

$$C_{1,\mathrm{eq}} = \frac{2}{\sqrt{\pi}} C_\alpha \Omega^{\alpha-1} u_0^{\alpha-1} \frac{\Gamma\left(\frac{\alpha+2}{2}\right)}{\Gamma\left(\frac{\alpha+3}{2}\right)}. \tag{C.8}$$

The equivalent coefficient in **Eq. (C.8)** depends on the assumed displacement amplitude u_0 and circular frequency Ω. Therefore, it is not a fixed property of the device. It is a response-dependent linearization valid only for the selected harmonic motion.

D APPENDIX D: Validation of the FVD Implementation in Midas Civil

The theoretical formulation of fluid viscous dampers (FVDs), including the velocity-dependent force law, the force–displacement loop under harmonic motion, and the energy dissipated per cycle, is presented in Section C. Therefore, this appendix does not repeat the complete derivation. Instead, it verifies that the FVD implementation used in Midas Civil reproduces the behavior expected from **Eq. (C.1)** and **Eq. (C.3)** before the dampers are introduced into the full Bill Emerson Bridge model, see Section A.

D.1 Test FVD Implementation

In Midas Civil, the FVD was modeled as a general link element[12, 36] with a viscous damper, or oil damper, property assigned in the active translational direction. Two damper definitions were considered. The first one corresponds to a linear fluid viscous damper with exponent $\alpha = 1.0$. The second one corresponds to a nonlinear fluid viscous damper with exponent $\alpha = 0.4$.

According to **Eq. (C.1)**, the linear case should produce a proportional relation between force and relative velocity, while the nonlinear case should produce a power-law relation. The objective of the test model is to confirm that the general link output in Midas Civil follows these two expected responses.

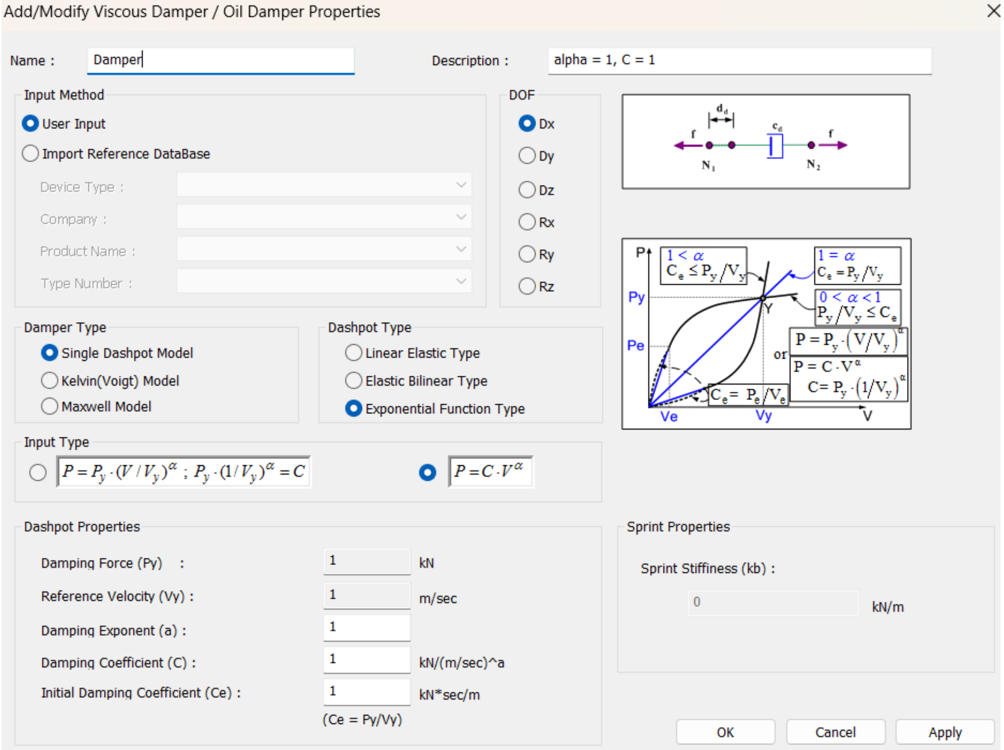
Add/Modify Viscous Damper / Oil Damper Properties

Name : Damper

Description : alpha = 1, C = 1

Input Method
● User Input
○ Import Reference DataBase
Device Type :
Company :
Product Name :
Type Number :

DOF
● Dx
○ Dy
○ Dz
○ Rx
○ Ry
○ Rz

Damper Type
● Single Dashpot Model
○ Kelvin(Voigt) Model
○ Maxwell Model

Dashpot Type
○ Linear Elastic Type
○ Elastic Bilinear Type
● Exponential Function Type

Input Type
○ $P = P_y \cdot (V/V_y)^\alpha \; ; \; P_y \cdot (1/V_y)^\alpha = C$
● $P = C \cdot V^\alpha$

Dashpot Properties
Damping Force (Py) : 1 kN
Reference Velocity (Vy) : 1 m/sec
Damping Exponent (a) : 1
Damping Coefficient (C) : 1 kN/(m/sec)^a
Initial Damping Coefficient (Ce) : 1 kN*sec/m
(Ce = Py/Vy)

Sprint Properties
Sprint Stiffiness (kb) : 0 kN/m

Figure D.1: Midas Civil viscous damper property definition for the linear FVD.

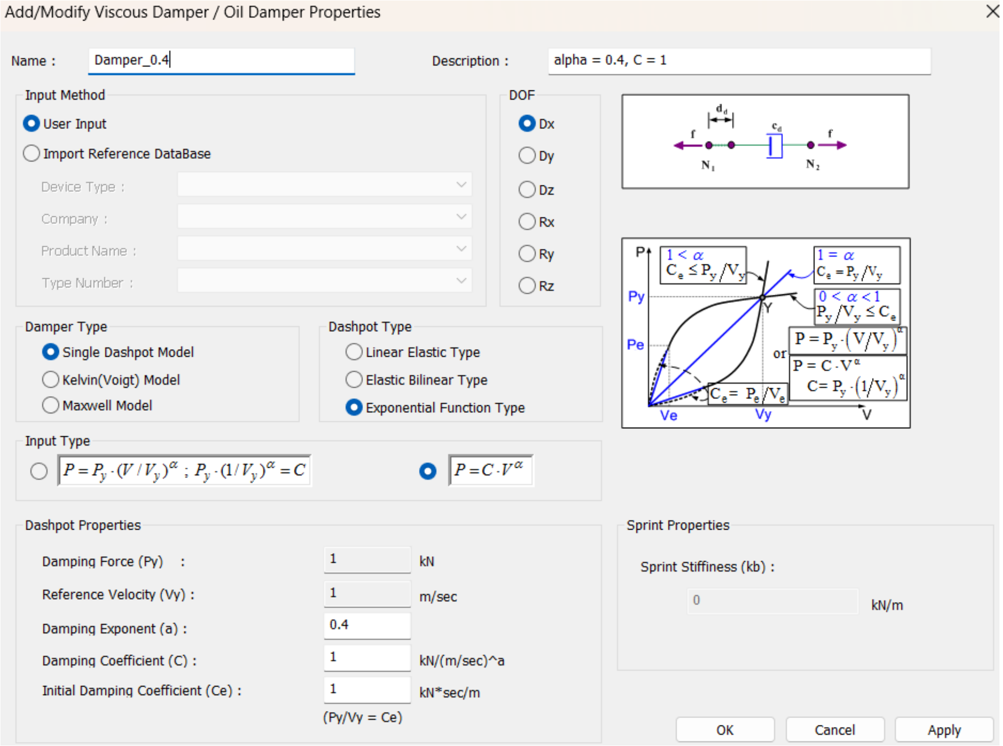
Add/Modify Viscous Damper / Oil Damper Properties

Name : Damper_0.4

Description : alpha = 0.4, C = 1

Input Method
● User Input
○ Import Reference DataBase
Device Type :
Company :
Product Name :
Type Number :

DOF
● Dx
○ Dy
○ Dz
○ Rx
○ Ry
○ Rz

Damper Type
● Single Dashpot Model
○ Kelvin(Voigt) Model
○ Maxwell Model

Dashpot Type
○ Linear Elastic Type
○ Elastic Bilinear Type
● Exponential Function Type

Input Type
○ $P = P_y \cdot (V / V_y)^{\alpha}$; $P_y \cdot (1 / V_y)^{\alpha} = C$
● $P = C \cdot V^{\alpha}$

Dashpot Properties
Damping Force (Py) : 1 kN
Reference Velocity (Vy) : 1 m/sec
Damping Exponent (a) : 0.4
Damping Coefficient (C) : 1 kN/(m/sec)^a
Initial Damping Coefficient (Ce) : 1 kN*sec/m
(Py/Vy = Ce)

Sprint Properties
Sprint Stiffness (kb) : 0 kN/m

Figure D.2: Midas Civil viscous damper property definition for the nonlinear FVD.

After defining the damper properties, a single general link element was created between Node 1 and Node 2. Node 1 was restrained against translation in the longitudinal and vertical directions, while Node 2 was left free in the direction of the applied dynamic excitation. A harmonic nodal force was then applied at Node 2 to impose cyclic motion and validate the force–velocity and force–displacement behavior of the FVD.

An auxiliary truss element was also created between the same two nodes. This element was included to provide an additional force-output quantity during the cyclic analysis and to compare the recorded response with the force developed by the general link. The truss stiffness was intentionally kept small so that the response remained governed by the FVD link.

D.1.1 Test Model Settings and Property Definitions

The material, section, loading, and link properties used in the test model are summarized below:

- Linear FVD/link: $C = 1.0$, $\alpha = 1.0$.
- Nonlinear FVD/link: $C = 1.0$, $\alpha = 0.4$.
- Distance between Node 1 and Node 2: $L = 1.0$ m.
- Truss element elastic modulus: $E = 1.0\ \text{kN/m}^2$.
- Truss element area: solid circular section with $A = 1.0\ \text{m}^2$.
- Forcing function: harmonic force with amplitude 1.0 kN and frequency 1.0 Hz.

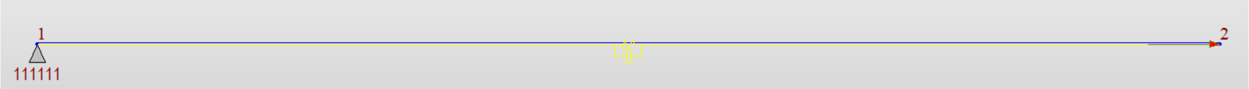

Figure D.3: Front view of the FVD test model. The general link is shown in yellow, the auxiliary truss element is shown in blue, and the dynamic nodal force is applied at Node 2.

The model was analyzed using nonlinear direct integration in Midas Civil. Separate analyses were performed for the linear and nonlinear FVD definitions so that the numerical link response could be compared against the behavior derived in Section C.

D.2 Results of the Test FVD Implementation

The results from **Fig. D.4** to **Fig. D.9** confirm that the implemented FVD response is consistent with the theoretical force law in **Eq. (C.1)**. In the nonlinear case, the force–velocity plot follows the expected power-law relation associated with $\alpha = 0.4$. In the linear case, the same plot reduces to the expected straight-line relation associated with $\alpha = 1.0$.

The force–displacement plots are also consistent with the harmonic response discussed in Section C. In particular, the linear case produces the elliptical loop expected from **Eq. (C.3)** when $\alpha = 1.0$, while the nonlinear case produces a fuller loop associated with the smaller velocity exponent. Small deviations from an ideal closed curve are attributed to the transient portion of the response and to the finite time step used in the direct integration analysis.

The comparison between the link force and the auxiliary truss force provides an additional check on the internal force output recorded during the dynamic analysis. The agreement in phase and magnitude confirms that the general link response is being consistently extracted from Midas Civil.

D.2.1 Nonlinear Case

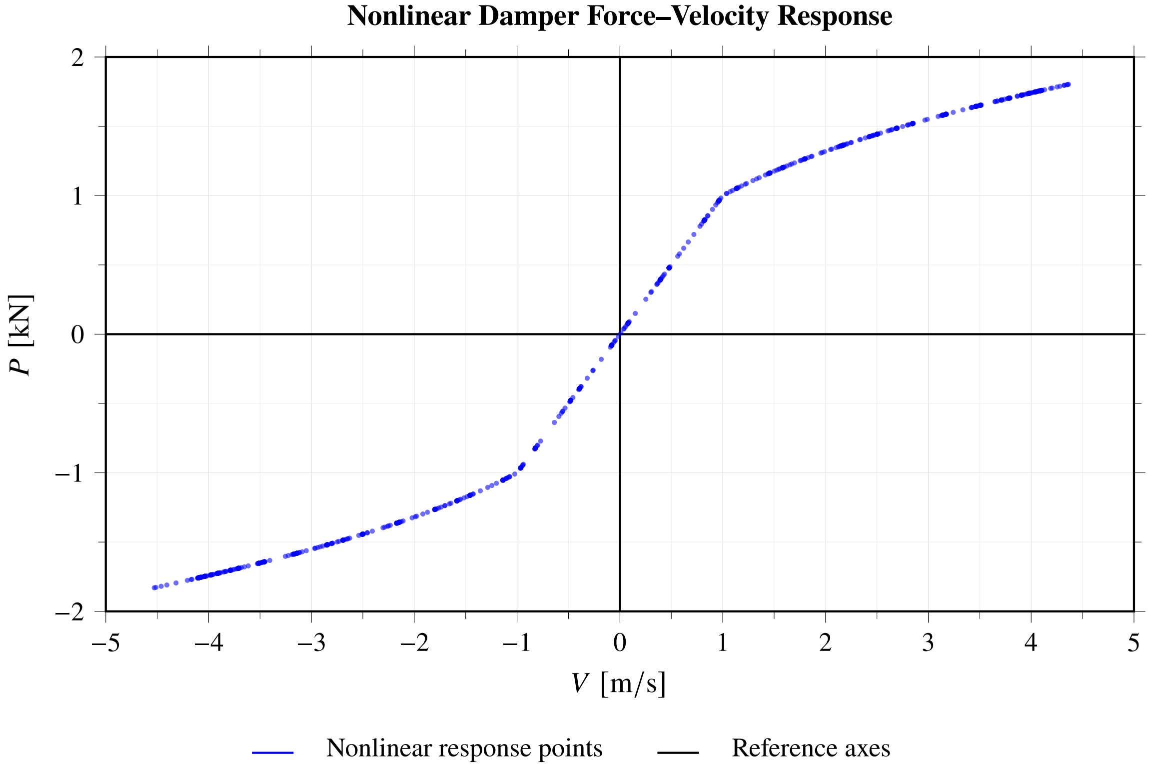

Figure D.4: Force–velocity cloud obtained from the nonlinear response-history analysis. The apparent sharp corners are attributed to the time step not being small enough to resolve the smooth curvature of the exponential force–velocity relation.

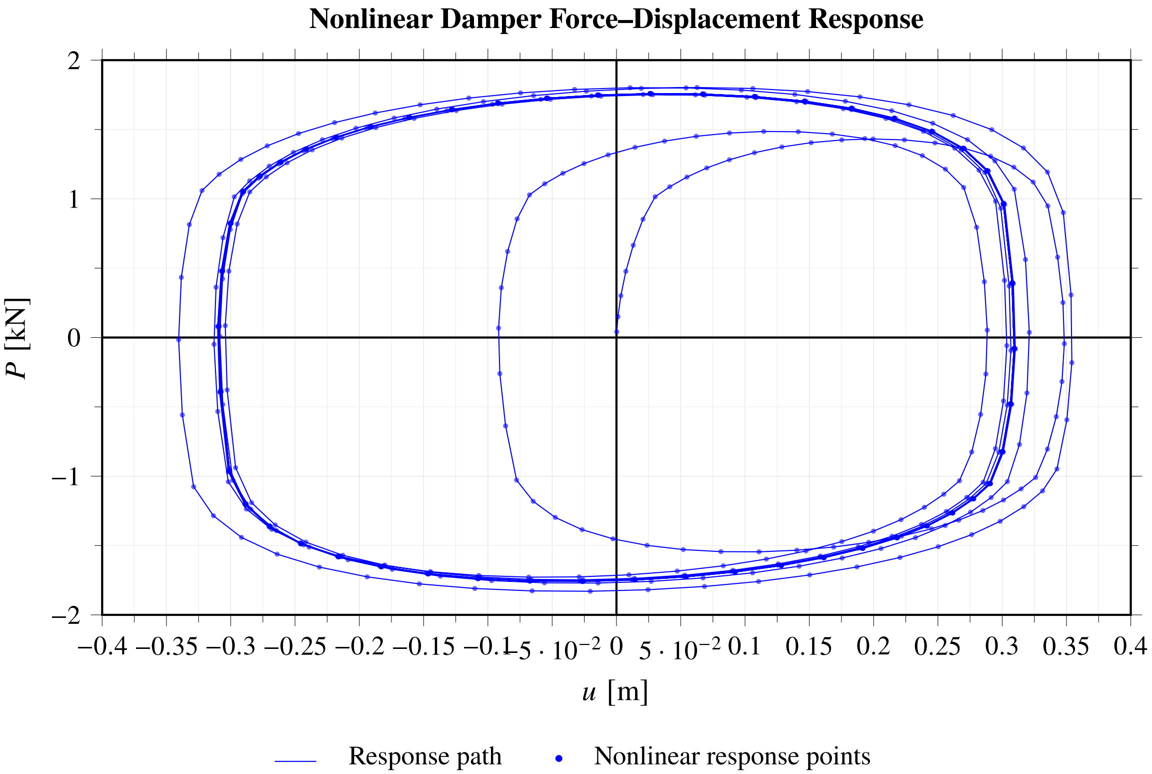

Figure D.5: Force–displacement cloud obtained from the nonlinear response-history analysis.

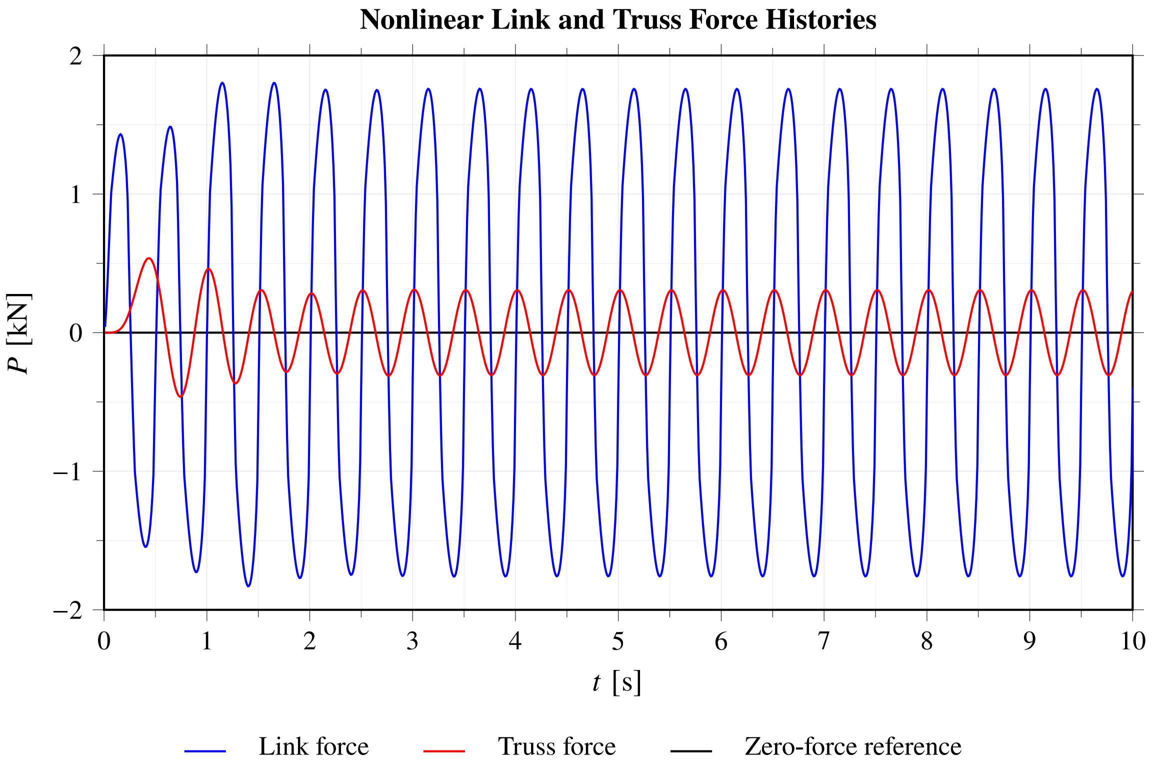

Figure D.6: Link and truss force histories obtained from the nonlinear response-history analysis.

D.2.2 Linear Case

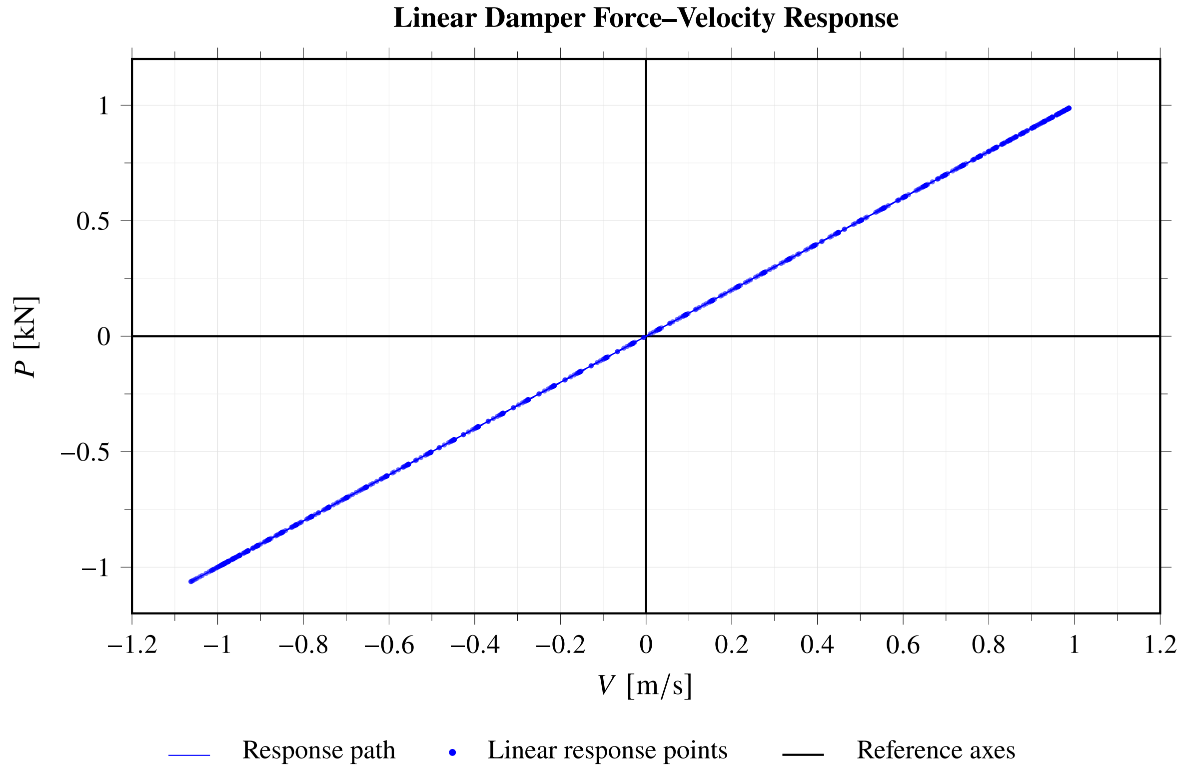

Figure D.7: Force–velocity response obtained from the linear response-history analysis.

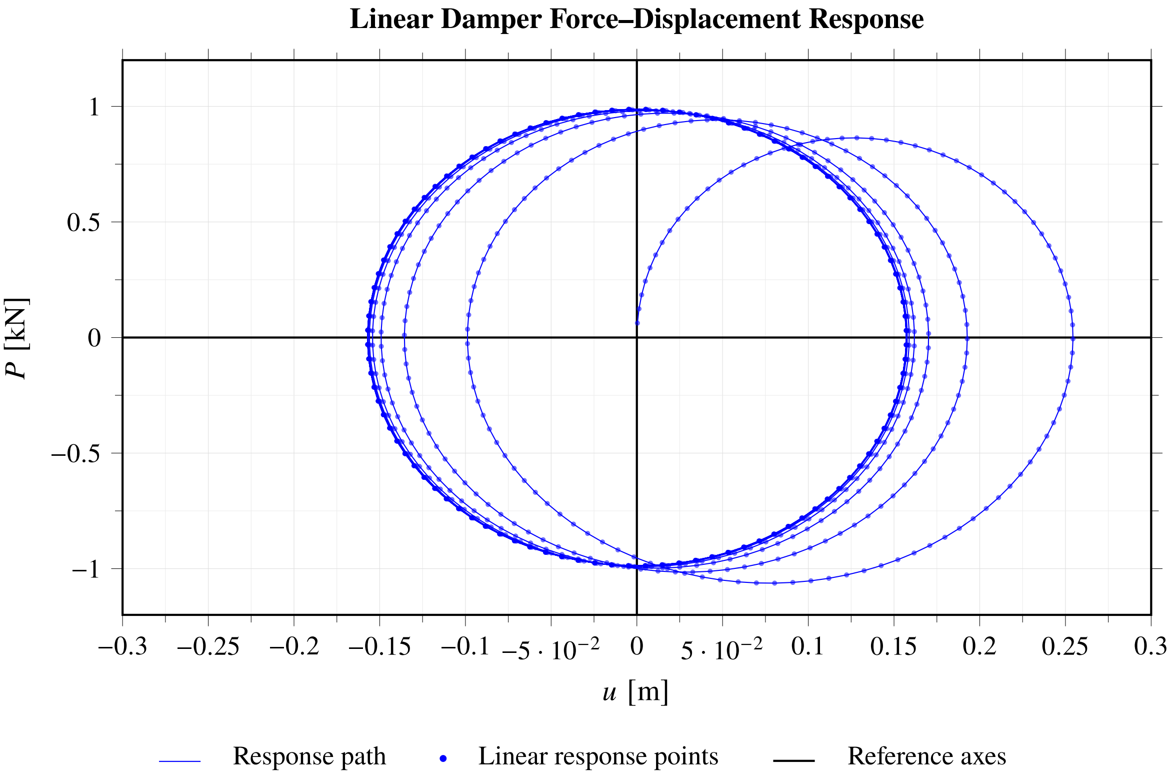

Figure D.8: Force–displacement response obtained from the linear response-history analysis.

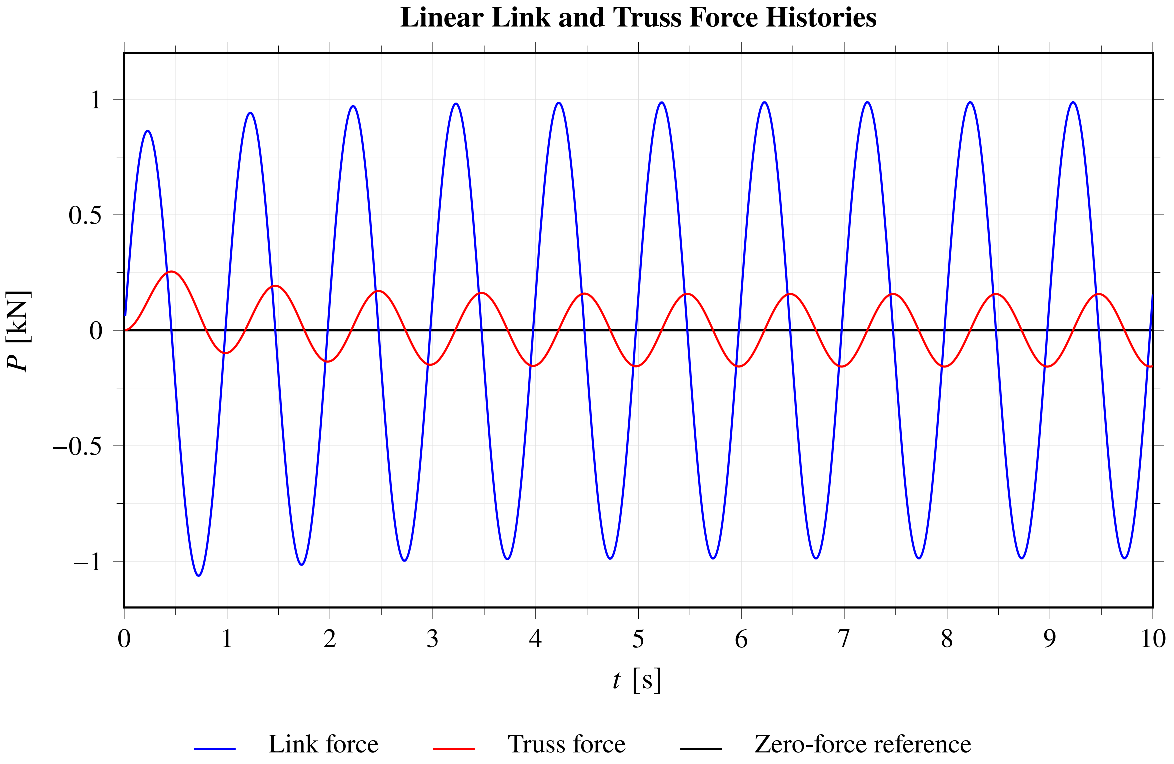

Figure D.9: Link and truss force histories obtained from the linear response-history analysis.

E Appendix E: Comment on Numerical Damping in MIDAS Civil

E.1 Motivation

During preliminary direct-integration response-history analyses, persistent high-frequency oscillations were observed in selected tower shear-force histories when the standard constant-average-acceleration Newmark scheme was used. The objective of this appendix is to document this numerical issue and to justify the modified Newmark parameters adopted in the nonlinear response-history analyses of the bridge.

The check is performed on the same bridge model using linear Newmark direct integration. The force quantity, output location, and ground-motion component were kept consistent with those used in **Fig. 5.22** only as a proxy. Therefore, the comparison isolates the effect of the time-integration parameters on the recovered tower shear-force response, without changing the structural quantity being examined.

E.2 Constant-Average-Acceleration Newmark Analysis

MIDAS Civil uses the Newmark method for direct-integration time-history analysis and allows the integration parameters γ and β to be entered directly through the user-defined option[13]. The standard constant-average-acceleration Newmark method uses

$$\gamma = \frac{1}{2}, \qquad \beta = \frac{1}{4}.$$

These values correspond to the classical average-acceleration Newmark scheme[37]. The method is widely used because it is unconditionally stable for linear systems[16, 17]. However, unconditional stability is not equivalent to numerical damping. For $\gamma = 1/2$, the constant-average-acceleration Newmark method does not introduce algorithmic damping of the high-frequency response[38].

The resulting tower shear-force history from the linear constant-average-acceleration Newmark analysis is shown in **Fig. E.1**.

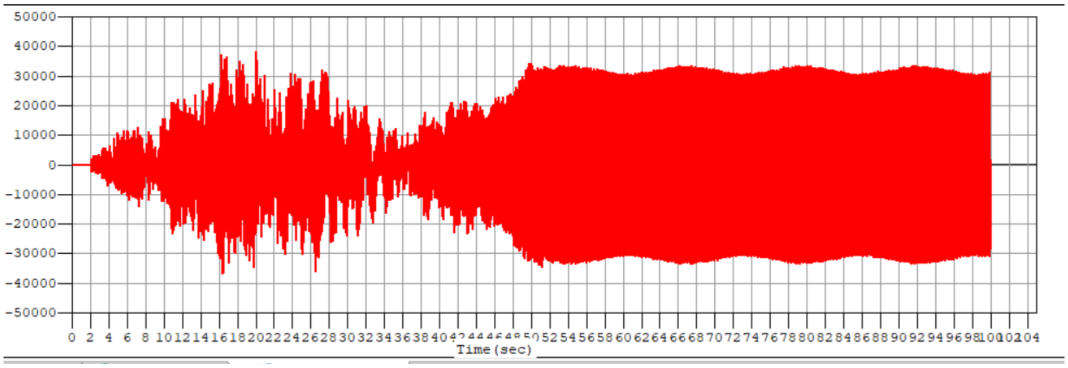

Figure E.1: Tower shear-force history obtained from linear Newmark direct integration with $\gamma = 1/2$, $\beta = 1/4$, and $\Delta t = 0.01$ s.

The linear analysis still produces a dense high-frequency force response after the main portion of the excitation. This observation indicates that the oscillation is not created only by the large-displacement geometric nonlinear formulation. It also shows that reducing the time increment from 0.05 s to 0.01 s does not, by itself, remove the high-frequency content from the recovered tower shear force. The result in **Fig. E.1** is therefore not interpreted as a complete time-step convergence study, but as a benchmark check showing that the same type of force oscillation can occur even when the analysis is linearized and the time step is refined.

E.3 Selection of Modified Newmark Parameters

To reduce the persistence of the high-frequency numerical content observed with the constant-average-acceleration scheme, modified Newmark parameters were selected for the final nonlinear response-history analyses. The purpose of this modification is not to recalibrate the physical damping of the bridge, but to introduce moderate algorithmic damping in the direct-integration procedure.

The Newmark parameter γ controls the acceleration weighting in the velocity update. The value $\gamma = 1/2$ corresponds to the constant-average-acceleration scheme and does not introduce algorithmic damping. Values larger than $1/2$ introduce numerical damping, primarily affecting the high-frequency part of the response[38]. Therefore, a moderate value was selected:

$$\gamma = 0.60. \tag{E.1}$$

This value remains close to the standard value $\gamma = 0.50$, so the selected scheme introduces limited numerical dissipation rather than a strongly damped reformulation of the response-history analysis.

For the Newmark method, unconditional stability for linear systems is obtained when the parameters satisfy[39]

$$\gamma \geq \frac{1}{2}, \qquad \beta \geq \frac{1}{4}\left(\gamma + \frac{1}{2}\right)^2. \tag{E.2}$$

After selecting the value of γ in **Eq. (E.1)**, the limiting value of β in **Eq. (E.2)** was adopted:

$$\beta = \frac{1}{4}\left(\gamma + \frac{1}{2}\right)^2. \tag{E.3}$$

This choice gives the smallest β value satisfying the unconditional-stability condition for the selected value of γ. It also recovers the standard constant-average-acceleration value $\beta = 1/4$ when $\gamma = 1/2$.

Substituting $\gamma = 0.60$ into **Eq. (E.3)** gives:

$$\beta = \frac{1}{4}\left(0.60 + \frac{1}{2}\right)^2 = \frac{1}{4}(1.10)^2 = 0.3025.$$

Thus, the Newmark parameters adopted in the nonlinear response-history analyses are

$$\gamma = 0.60, \qquad \beta = 0.3025.$$

These values introduce moderate algorithmic damping while satisfying the standard linear unconditional-stability condition for the Newmark method.

E.4 Modified Newmark Numerical-Damping Check

The resulting tower shear-force history from the modified Newmark analysis is shown in **Fig. E.2**.

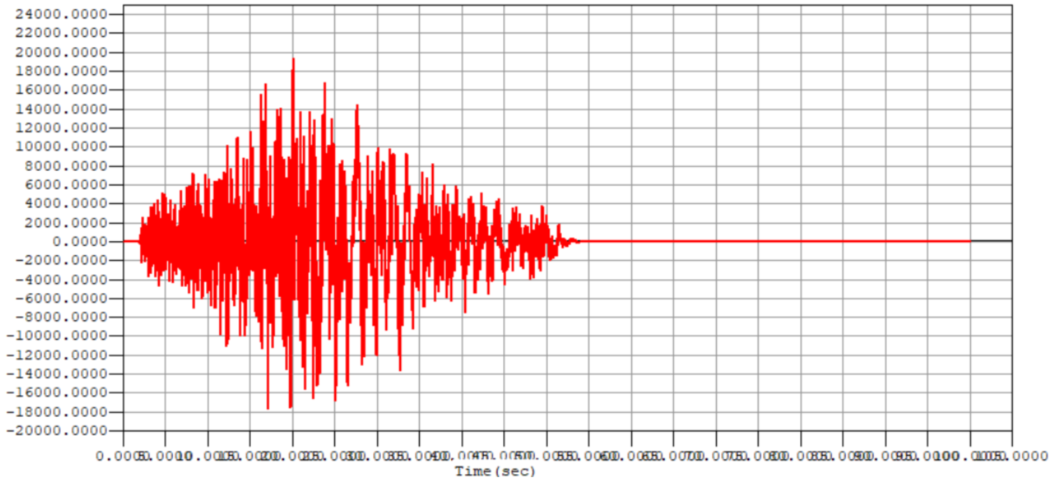

Figure E.2: Tower shear-force history obtained from linear Newmark direct integration with $\gamma = 0.60$, $\beta = 0.3025$, and $\Delta t = 0.01$ s.

The comparison between **Fig. E.1** and **Fig. E.2** shows that the modified Newmark parameters reduce the persistence of the high-frequency tower shear-force oscillation. This supports the interpretation that the oscillatory tail is associated with high-frequency numerical content retained by the constant-average-acceleration scheme. Based on this check, the modified parameters $\gamma = 0.60$ and $\beta = 0.3025$ were adopted for the nonlinear response-history analyses presented in the main body of the report.

E.5 Interpretation

The most defensible interpretation is that the tower shear histories are affected by high-frequency numerical content associated with the direct-integration and force-recovery procedures. The persistence of the oscillation in the linear $\Delta t = 0.01$ s analysis indicates that the behavior is not solely a consequence of geometric nonlinearity. The reduction of the oscillation under the modified Newmark parameters further supports the numerical-damping interpretation.

This appendix does not establish full time-step convergence, because a dedicated sequence of otherwise identical analyses with progressively smaller time increments was not performed. Additional comparisons between element shear forces, tower base reactions, and section-cut resultants would also help identify whether the oscillation is mainly a local force-recovery effect or a global dynamic response. Consequently, tower shear-force peaks associated with the high-frequency oscillatory tail should be interpreted with caution, while displacement histories remain more reliable indicators of the lower-frequency global bridge response.